

Dissertation

# Application of Waveguide Mode Diagnostics for Remote Sensing in Accelerator Beam Pipes

ausgeführt zum Zwecke der Erlangung des akademischen Grades eines Doktors der  
Technischen Wissenschaften unter der Leitung von

Arpad L. Scholtz

E389

Institut für Nachrichtentechnik und Hochfrequenztechnik

eingereicht an der Technischen Universität Wien  
Fakultät für Elektrotechnik und Informationstechnik

von

**Thomas Kroyer**

9726048

Mitterweg 632, A-7201 Neudörfel

Wien, 24. August 2005

## Zusammenfassung

In der vorliegenden Arbeit werden zwei Systeme zur Ferndiagnostik in Strahlrohren von CERN Teilchenbeschleunigern untersucht. Zu diesem Behufe werden Mikrowellen, die sich als Hohlleitermoden im Strahlrohr ausbreiten, verwendet. Das erste System ist eine Anwendung der Reflektometrie in Wellenleitern. Da das Auftreten von Störungen im Strahlrohr des Large Hadron Collider (LHC) zu erheblichen Problemen führen kann, besteht großes Interesse daran, solche Störstellen finden und lokalisieren zu können. Zeitbereichsreflektometrie auf Wellenleitern unter Verwendung synthetischer Pulse wird dafür eingesetzt. Das System baut auf einem Netzwerkanalysator auf, wobei der fundamentale TE und TM Modus im LHC Strahlrohr verwendet wird. Mittels numerischer Signalverarbeitung wird die Verschmierung der Pulse durch Hohlleiterdispersion entfernt. Zwei Verwendungsmöglichkeiten für das Reflektometer werden vorgeschlagen, die "Assembly Version" fuer Kontrollen während der Bauphase des LHC und die "In Situ Version" für Messungen am fertiggestellten LHC, auch nachdem das Strahlrohr evakuiert wurde. Für beide Versionen wurden Koppler entworfen, simuliert und an bis zu 400 m langen Rohren getestet.

Die zweite Ferndiagnostikanwendung befaßt sich mit dem Elektronenwolkeneffekt im Super Proton Synchrotron (SPS). Es wurde versucht, die über die Länge gemittelte Elektronendichte im Strahlrohr über die Transmission von Mikrowellen zu messen. Eine von der Elektronenwolke stammende Phasen- oder Amplitudenänderung wird mit der SPS-Umlauffrequenz moduliert, was hochempfindliche Seitenbandmessungen ermöglicht. Starke strahlinduzierte Signale, die zu unerwünschten Effekten führen koennen, wurden gefunden. Mögliche Erklärungen der beobachteten mit dem Strahl zusammenhängenden Modulation werden diskutiert.

## **Abstract**

In this work, two remote sensing systems using waveguide modes in beam pipes of CERN accelerators are studied. The first is an application of time domain reflectometry in waveguides. Since the emergence of unexpected obstacles in the Large Hadron Collider (LHC) beam screen may lead to major disturbances, it is highly desirable to have a tool for detection and localization of such a fault. Waveguide mode time domain reflectometry using the synthetic pulse technique has been selected for this purpose. The system is based on a vector network analyzer using the fundamental TE and TM mode on the LHC beam-screen. Numerical signal processing is used to remove waveguide dispersion. Two modes of operation for the Reflectometer are proposed, the Assembly Version for inspection during the installation of LHC and the In Situ Version for measurements with the machine under vacuum. Coupling structures for both versions were designed and simulated, and tests on lines of up to 400 m length were performed.

The second remote sensing application turns around the electron cloud effect in the Super Proton Synchrotron (SPS). It was tried to measure the line-averaged electron cloud density by transmitting microwaves along the beam pipe. Any electron cloud-related phase or amplitude shift is modulated by the SPS revolution frequency, making highly sensitive sideband measurements possible. Large beam-induced RF signals leading to parasitic effects had to be coped with. Possible explanations of the observed beam-related modulation are discussed.

# Contents

## I Introduction

<b>1 CERN</b>	<b>1</b>
1.1 Accelerators . . . . .	1
1.2 Brief introduction to synchrotrons . . . . .	3
<b>2 Large Hadron Collider</b>	<b>9</b>
2.1 Machine lay-out . . . . .	9
2.2 Beam screen . . . . .	12
2.2.1 Properties at cryogenic temperatures . . . . .	17
2.2.2 Overall attenuation . . . . .	20
2.3 Beam vacuum interconnects . . . . .	21
2.4 Installation and commissioning . . . . .	23

## II LHC reflectometer **25**

<b>3 Concept</b>	<b>26</b>
3.1 Methods for obstacle detection . . . . .	26
3.2 Synthetic pulse reflectometry . . . . .	27
3.2.1 Resolution . . . . .	28
3.2.2 Range & Sensitivity . . . . .	29
3.2.3 Obstacles . . . . .	31
3.3 Summary . . . . .	31
<b>4 Reflectometer Assembly Version</b>	<b>32</b>
4.1 TE mode coupler . . . . .	32
4.2 TM mode coupler . . . . .	35
4.3 Data processing . . . . .	38
4.3.1 Basic functionality . . . . .	39
4.3.2 Advanced features . . . . .	46
4.3.3 Backend functions . . . . .	46
4.4 Performance . . . . .	49
4.4.1 Resolution . . . . .	49
4.4.2 Range . . . . .	50
4.4.3 Sensitivity . . . . .	50
4.4.4 Test obstacles . . . . .	51
4.4.5 Multiple reflections . . . . .	55

4.5	Reflectometry on the cryogenic ring line . . . . .	56
4.5.1	RF properties of the QRL . . . . .	58
4.5.2	Measurements . . . . .	61
4.5.3	Preliminary conclusion and possible application . . . . .	64
4.6	Summary . . . . .	64
<b>5</b>	<b>Reflectometer In Situ Version</b>	<b>66</b>
5.1	Concept . . . . .	66
5.1.1	Desirable features . . . . .	67
5.1.2	Location . . . . .	67
5.1.3	Modes of operation . . . . .	68
5.2	Modified VM module . . . . .	69
5.2.1	Coupler design . . . . .	70
5.2.2	Realisation of adopted design . . . . .	81
5.3	Performance . . . . .	82
5.3.1	Range . . . . .	83
5.3.2	Sensitivity . . . . .	83
5.4	Potential fringe applications . . . . .	84
5.5	Summary . . . . .	85
<b>III</b>	<b>Microwave transmission diagnostics</b>	<b>86</b>
<b>6</b>	<b>Electron cloud effect</b>	<b>87</b>
6.1	Introduction . . . . .	87
6.2	Electron cloud in the LHC . . . . .	90
6.3	Summary . . . . .	92
<b>7</b>	<b>SPS microwave transmission experiment</b>	<b>93</b>
7.1	Concept . . . . .	93
7.2	Measurement set-up . . . . .	94
7.2.1	Machine lay-out . . . . .	94
7.2.2	RF measurement equipment . . . . .	96
7.2.3	Testing of the measurement set-up . . . . .	100
7.3	Data acquisition . . . . .	102
7.4	Results . . . . .	104
7.4.1	Beams and Machine Parameters . . . . .	104
7.4.2	Attenuation with beam . . . . .	105
7.5	Bench cross-check . . . . .	113
7.5.1	Electrons injected into a pipe carrying waveguide modes . . . . .	114
7.5.2	Resonator measurements . . . . .	117
7.5.3	Discussion . . . . .	118
7.6	Possible explanations . . . . .	119
7.6.1	Electron cyclotron absorption . . . . .	120
7.6.2	Tails . . . . .	120
7.7	Summary . . . . .	121

<i>CONTENTS</i>	iii
<b>Conclusion</b>	<b>121</b>
<b>Bibliography</b>	<b>123</b>
<b>List of Abbreviations</b>	<b>126</b>
<b>Acknowledgements</b>	<b>127</b>

**Part I**

**Introduction**

# Chapter 1

## CERN

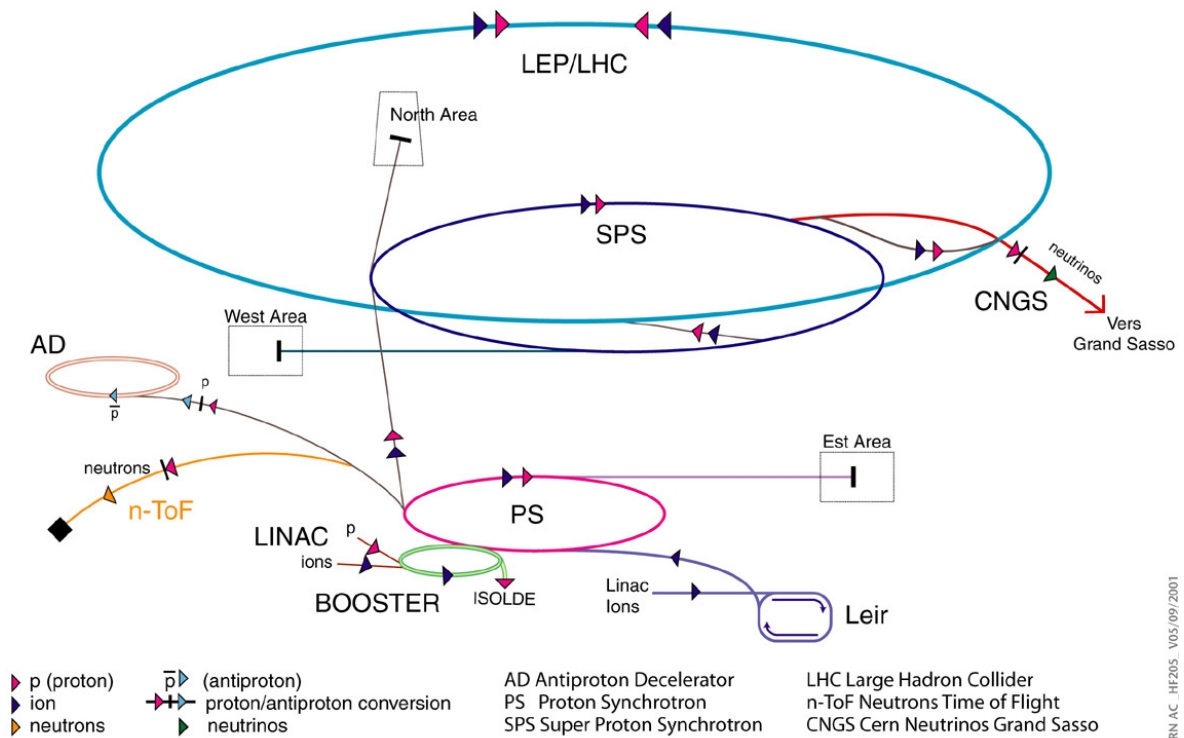
After the destructions of World War II, European nuclear physics was in a very bad state. Seizing the suggestion of the French physicist Louis de Broglie, the *Conseil Européen pour la Recherche Nucléaire* (CERN), or *European Organisation for Nuclear Research* was formally established with 11 member states in 1954. For the site of the CERN laboratory complex the quiet village Meyrin a few kilometers outside Geneva close to the French border was chosen.

Today CERN has 20 member states and works in close collaboration with many non-member states like the U.S., Russia, India or Japan. The current activities are concentrated on the construction of the Large Hadron Collider (LHC), which will become operational in 2007. In addition to particle physics there are many spin-offs in other technologies, the most famous being the World Wide Web, that was developed at CERN in 1990-91.

### 1.1 Accelerators

The wide-spread particle physics program being carried out at CERN relies on a number of accelerators. As an accelerator only accepts particles in a given energy range, particles have to go through different acceleration stages for reaching very high energies. CERN's flagship project, the LHC (Large Hadron Collider) will sit at the end of CERN's accelerator chain, as shown in Fig. 1.1. Protons being collided in the LHC experiments will already have gone a long way. Emitted by a proton source, they are first run through LINAC2 (Linear Accelerator 2), which they leave with a momentum of 50 MeV/c. Then they are further accelerated by circular machines, namely the Proton Synchrotron Booster (PSB, ejection energy 1.4 GeV), the PS (Proton Synchrotron, ejection energy 26 GeV) and the SPS (Super Proton Synchrotron, ejection energy 450 GeV) before finally being injected into the LHC. For each injection the beam has to be matched to the machine in order to minimize beam losses and other detrimental effects.

In addition to furnishing protons and ions for the LHC once it is in operation, the machines in the injector chain produce a variety of lower energy beams for fixed target physics, antimatter production and many other experiments.



CERN.AC\_HF2005\_V05/09/2001

Figure 1.1: The accelerators in use and under construction at CERN. Protons going to the Large Hadron Collider (LHC) start their journey in the Linear Accelerator (Linac, bottom of image) and are pre-accelerated in PSB, PS and SPS before being injected into LHC. The precursor of LHC was the Large Electron Positron Collider (LEP), ions are pre-accelerated in the Low Energy Ion Ring (LEIR) and ISOLDE is the name of an experimental area.

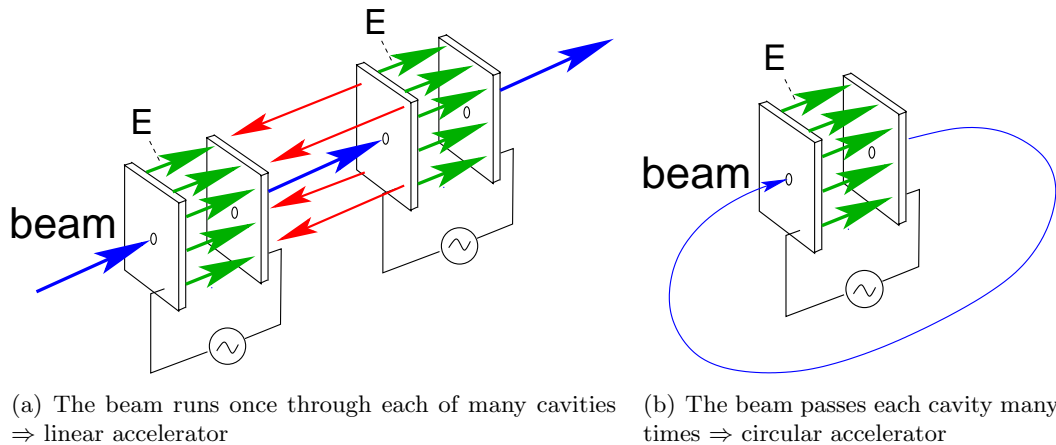


Figure 1.2: Accelerating cavities in linear and circular accelerators.

## 1.2 Brief introduction to synchrotrons

In the last section we saw that most accelerators at CERN are circular machines (Fig. 1.1), or more precisely, synchrotrons. Only in the initial phase of acceleration other types of accelerators are used. Since most of this thesis turns around synchrotrons, a short introduction on the principles of such machines will be given here. For more detail the reader is referred e.g. to [1].

### Principle of acceleration

The force  $\vec{F}$  on a particle of charge  $q$  moving with velocity  $\vec{v}$  in an electric field  $\vec{E}$  and a magnetic field  $\vec{B}$  is given by the Lorentz force

$$\vec{F} = q(\vec{E} + \vec{v} \times \vec{B}) \quad (1.1)$$

Since the force due to the magnetic field acts normal onto the velocity, energy gain is possible only if there is an electric field. First accelerators used electrostatic fields, and this type of acceleration is still widely used e.g. in electron tubes. However, since static voltages obtainable in the lab are limited (10 MV range for Van de Graaf generators), the interest turned to time varying fields to reach still higher particle energies.

Fig. 1.2 shows two of the principle options using time varying fields. The particle passes through a capacitor parallel to the RF (radio frequency) electric field, which is oscillating at a frequency  $f_{RF}$ . Each time a particle passes through one of those capacitors, it gains the energy  $qU$ , with the gap voltage  $U$  between the plates.<sup>1</sup> In order to maximize the particle energy, several of these acceleration stages can be used in a line, leading to a linear accelerator. Another possibility is to make the particle pass through each acceleration stage again and again, which leads to a circular accelerator. To prevent the RF fields in the capacitor from leaking out, the rims of the two plates have to be connected. The entire structure then becomes a cavity with distinct resonant modes, see Fig. 1.3. In many cases the  $TM_{010}$  mode is used, which has its maximum

<sup>1</sup>Here it is assumed that the time the particle takes for passing through this gap is much smaller than the RF period. If this is not the case, the voltage must be averaged over the transit time.

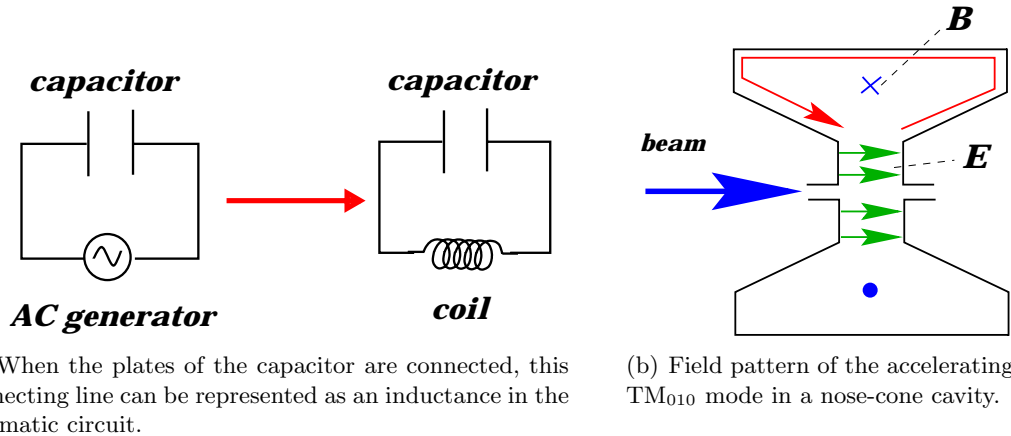


Figure 1.3: Going from a capacitor to a cavity

electric field on the beam axis. To give an example, the CERN SPS is equipped with travelling wave cavities operating at 200 MHz and delivering a peak power of about 1 MW [3]. In the following we will focus on circular accelerators. For further information on Linacs the reader is referred to [4].

### Circular machines

In circular machines, the particle trajectories need to be bent. This is most commonly done by static magnetic fields normal to the orbital plane. The bending radius  $R$  can be found by equating the Lorentz force with the centripetal force.

$$qvB = \frac{mv^2}{R} \quad (1.2)$$

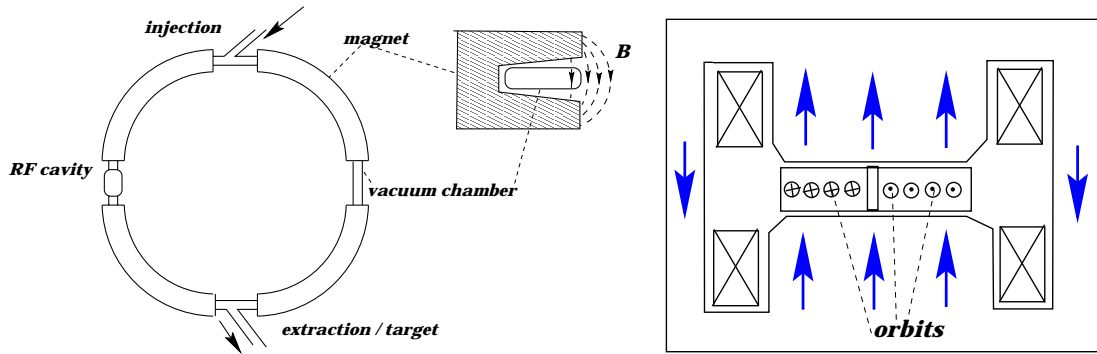
with  $q$ ,  $m$  and  $v$  designating the particle's charge, mass and velocity, respectively. Using the particle momentum  $p = mv$ , the equation above can be written

$$BR = \frac{p}{q} \quad (1.3)$$

Fig. 1.4 shows the two most prominent examples for circular machines, the synchrotron and the cyclotron. The particles are injected into the synchrotron in one of the straight sections. The extraction, RF cavities, instrumentation or physics experiments may be installed in other straight sections. In the curved sections, dipoles bend the particles to complete the orbit. When the particles are accelerated, the bending field in the magnets must be increased to keep the particles in the orbit, the magnets are "ramped".

The concept of the cyclotron is different. Here the magnetic field is kept constant, which means that the particles' bending radius increases when they are accelerated by the RF field in the accelerating gap (not shown in image). The low-energy particles are injected into the center of the machine; they spiral outwards as they gain energy. At some point, they are extracted. A very good introduction on cyclotrons can be found in [5].

There is yet another kind of accelerator, the betatron. In its lay-out it is pretty similar to the cyclotron, however, there are no acceleration cavities. Rather, the acceleration electric field is created by ramping the magnetic bending field.



(a) Synchrotron: The magnetic field is increased as the particles are accelerated which keeps the bending radius constant.

(b) Cyclotron: the magnetic field (blue arrows) is constant, which implies that the particles spiral outwards as they gain energy.

Figure 1.4: The two main types of circular accelerators.

### Longitudinal motion in synchrotrons

With the use of cavities for acceleration, a particle gains energy only if it arrives when the gap voltage is positive. This means that a beam of particles needs to be grouped in packets, or “bunched”. This can be done before injecting the beam into a synchrotron, or one can also *slowly* turn on the cavity gap voltage so that bunches gradually form out of the initial longitudinal particle distribution.

In a dipole the orbit radius gets larger for increasing particle momentum, but the particle velocity increases, as well. The relation between revolution frequency  $f_{rev}$  and particle momentum  $p$  is given by [6]

$$\frac{df_{rev}}{f_{rev}} = \left( \frac{1}{\gamma^2} - \alpha_p \right) \frac{dp}{p} \quad (1.4)$$

with the relativistic factor

$$\gamma = \frac{1}{\sqrt{1 - \frac{v^2}{c^2}}}, \quad (1.5)$$

the speed of light  $c$  and the momentum compaction factor  $\alpha_p$ , a machine parameter that is mainly determined by the quadrupoles. At low particle energy  $1/\gamma^2 \approx 1 > \alpha_p$ , that is, the revolution frequency increases with momentum. When the momentum gets high,  $\gamma \gg 1$  and  $1/\gamma^2 < \alpha_p$ . Now the revolution frequency decreases when the momentum increases. The energy when  $1/\gamma^2 = \alpha_p$  is called transition energy.

Assume now that there is a stationary beam in the machine, i.e. the acceleration voltage is on, but the phase of this voltage is such that the center of the bunch passes at a zero crossing of the cavity voltage. We are in point (a) in Fig. 1.5, and the slope of the cavity voltage is positive. Assume further that we are below transition, that is, the revolution frequency increases as the momentum increases. The particle (c) comes after the center of the bunch, so it has lower energy. Since it sees a positive acceleration voltage, it will gain energy and move towards the center of the bunch. The opposite will happen to particle (b). The particles are thus focused longitudinally. For particles not too far from the center of the bunch, the restoring force increases approximately linearly with the

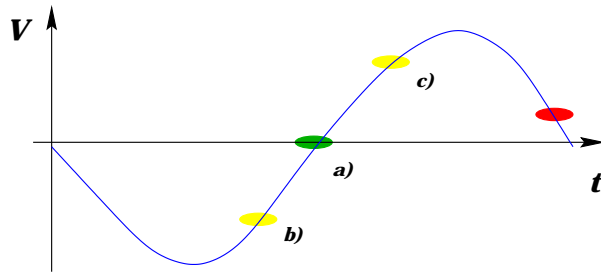


Figure 1.5: Particles with different energy arrive at different times in a cavity.

phase, so the particles will make harmonic oscillations around the center of the bunch. The frequency of this longitudinal motion is called *synchrotron frequency*; its inverse is the *synchrotron tune*.

A very important consequence of this effect is that when a particle beam crosses the transition energy, it will suddenly be on the wrong slope of the cavity voltage. To preserve longitudinal focusing, the phase of the cavity voltage must then be changed by 180 degrees. In practice, the transition energy is not slowly crossed but jumped over by changing the value of  $\alpha_p$ .

### Filling pattern and spectrum of the beam-induced currents

This far only single bunches have been considered. Normally bunches are grouped in so-called “bunch trains” or “batches”. The number of bunches per batch as well as the distance between successive bunches varies in a wide range from accelerator to accelerator. Typical values for the LHC beam are 72 bunches per batch with a bunch spacing of 25 ns. The beams in the SPS will be treated in more detail in section 7.4.

Since the beam is made up of charged particles, it induces currents in the metallic beam pipe and excites electromagnetic waves. These currents and electromagnetic waves are detected by beam diagnostics equipment. The term “beam signals” is often used for the signals induced by the beam. Similarly, its spectrum is called “beam spectrum”.

The longitudinal shape of each bunch is usually approximated by a cosine squared distribution, however, microstructures in the bunch profile can be present, as well. In the SPS, with bunch lengths are of the order of 1 ns, the spectrum of one single bunch has its first zero at about 560 MHz [27]. For passing bunch trains, this signal is repeated with a period equal to the bunch spacing. In the frequency domain, this corresponds to a multiplication with a Dirac comb type signal. For the LHC beam, the spacing of the frequency components is therefore  $1/25 \text{ ns} = 40 \text{ MHz}$ . In addition to that, the signals repeat with the revolution frequency  $f_{rev}$ , and so the spectrum is folded again with a comb with line spacing  $f_{rev}$ .

### Transverse motion in synchrotrons

When a particle beam leaves the particle source, it has a certain divergence. In order to control the transverse beam size, focusing is needed in the transverse plane. Quadrupole magnets are used for this purpose. The magnetic field quadrupole in Fig. 1.6(a) is given

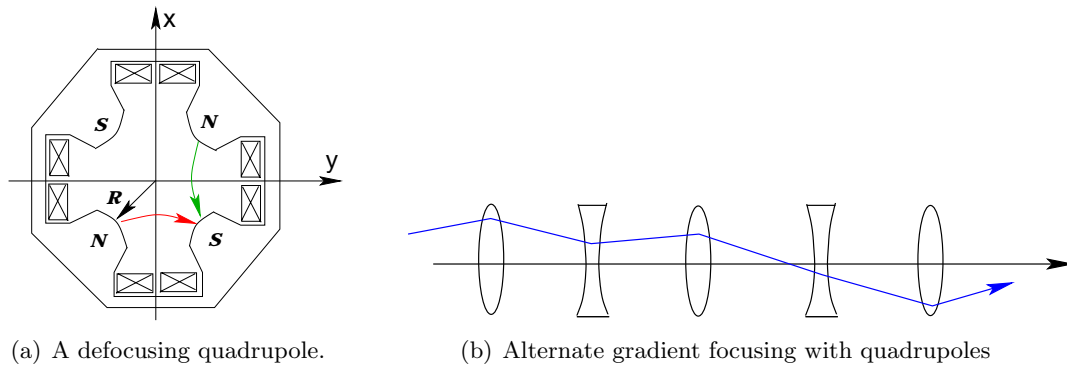


Figure 1.6: Transverse focusing with quadrupoles

by

$$\begin{aligned} B_x &= -g_1 y \\ B_y &= -g_1 x \end{aligned}$$

with a positive constant  $g_1$ . Particles having a positive charge  $q$  and velocity  $v$  flying through the quadrupole (into the plane of the paper) then feel the force

$$\begin{aligned} F_x &= g_2 y \\ F_y &= -g_2 x \end{aligned}$$

with  $g_2 = qv g_1$ . This quadrupole is defocusing in the horizontal plane and focusing in the vertical plane. For a relativistic beam ( $\gamma \gg 1$ ) the trajectory of particles in quadrupoles can be approximated by formulas known from geometric optics. Focusing (defocusing) quadrupoles then act like thin convex (concave) lenses. In general, in synchrotrons focusing and defocusing quadrupoles are used in a regular pattern in both curved and straight sections. This scheme, also known as *alternate gradient focusing*, is illustrated in Fig. 1.6(b). In such a structure, similar to the longitudinal direction, the particles can also make quasiharmonic oscillations. These oscillations in the transverse plane are known as *betatron motion*. The oscillation frequency along the horizontal axis is called horizontal betatron frequency, its inverse is the horizontal betatron tune or simply horizontal *tune*. Similar terms are used for the vertical motions.

The practical importance of the transverse tunes comes from the fact that when the tune has an integer value, the beam gets unstable. This is due to the fact that the impact of any little perturbation in the ring adds up at each turn. Such perturbations cannot be avoided, they may be pumping ports, changes of the beam pipe cross-section or the like. Therefore integer tunes must be avoided.

### Machine cycle

Depending on the purpose of an accelerator it may be operated in various ways. In the following a typical SPS physics cycle is discussed, see Fig 1.7. In such a cycle, beam for fixed target experiments is produced. At time  $T = 0$ , there is no beam in the machine, i.e. the beam intensity is zero. In this context, the term “beam intensity” is used for the total number of particles in the machine. The magnetic field is low,

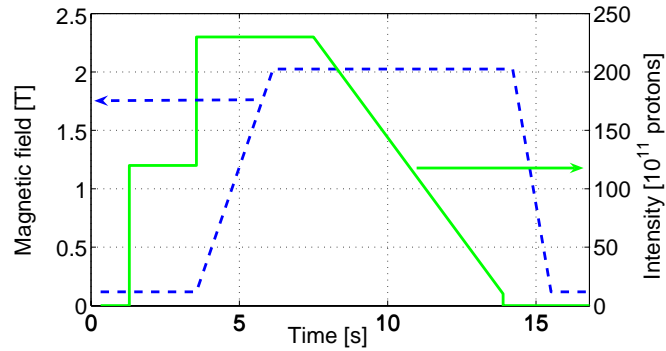


Figure 1.7: The magnetic field in the main bending magnets (solid green curve) and the beam intensity (dashed blue curve) during a typical SPS machine cycle.

since the machine is prepared for the first injection, it is at the so-called “injection flat bottom”. At about  $T = 1$  s, the first batch is injected and about 2 s later the second batch. Now there are about  $2.3 \cdot 10^{13}$  protons in the machine. Immediately after this second injection the acceleration begins and the magnetic field ramps (increases) up to around 2 T at top energy ( $T = 6$  s). Now, the beam is either sent to LHC, or it goes to another experiment, as in the present case. Since the physics experiments prefer a low beam intensity over a relatively long time, the beam is extracted slowly during about 6 s. Thereafter, the magnetic field is ramped back to the level at injection. If the beam would have to go to LHC, it would have been extracted within one single turn.

## Chapter 2

# Large Hadron Collider

In order to push the frontiers of physics further out, collisions at higher and higher energies have to be studied. Up to the end of 2000 the Large Electron-Positron Collider (LEP) was in service at CERN, opening up a new important discovery domain. With a length of nearly 27 km it was the world's largest particle accelerator, achieving beam energies of up to 100 GeV. After exploiting the LEP for 11 years, it was decided to shut it down to make place for the next generation particle accelerator, the Large Hadron Collider (Fig. 2.1). The existing LEP tunnel about 100 m underground will be reused for the installation of the Large Hadron Collider (LHC), which is scheduled to become operational in 2007.

The LHC's proton beams will be accelerated to an energy of 7 TeV, which is 70 times higher than in LEP. To keep the beam on track, powerful superconducting magnets producing fields up to 8.4 T, cooled with superfluid helium are necessary. In Figure 2.2 the cross-section of an LHC cold arc is shown. The entire assembly is under high vacuum. In the very center there are the two beam-pipes embedded in the dipole magnets.

### 2.1 Machine lay-out

In order to avoid expensive civil engineering works, the LHC was designed to follow the existing LEP tunnel [2]. It has eight arcs and eight long straight sections, which are approximately 2800 and 530 m long, respectively. The arc sections host the main bending magnets, while the straight sections are used as experimental or utility insertions (2.3). All eight arcs have basically the same layout.

The two high luminosity experiments (ATLAS and CMS) are situated in point 1 and point 5 in the center of the corresponding long straight sections (LSS). The two smaller experiments ALICE and LHCb are located in point 2 and point 8. The four remaining long straight sections are used for the RF cavities, collimation systems and the beam dump. The injection into LHC takes place close to point 2 for beam 1 and close to point 8 for beam 2.

In the current design (optics version 6.4) the arcs are made of 23 regular arc cells each. Each cell is 106.9 m long and composed of two half cells, each of which contains three dipole magnets (14.3 m magnetic length, 15.5 m beam screen length) and one 6.6 m long short straight section (SSS). This SSS houses the lattice quadrupoles and some higher order multipoles. The layout of an LHC cell is shown in Fig. 2.4. Apart from the main bending magnets (MBA and MBB) and the lattice quadrupoles (MQ) a variety



Figure 2.1: The ring of LHC. The CERN labs are located at the left close to the point where the two larger rings intersect. The dotted line is the border between Switzerland and France. Note the Geneva International Airport at the bottom of the picture for scale.

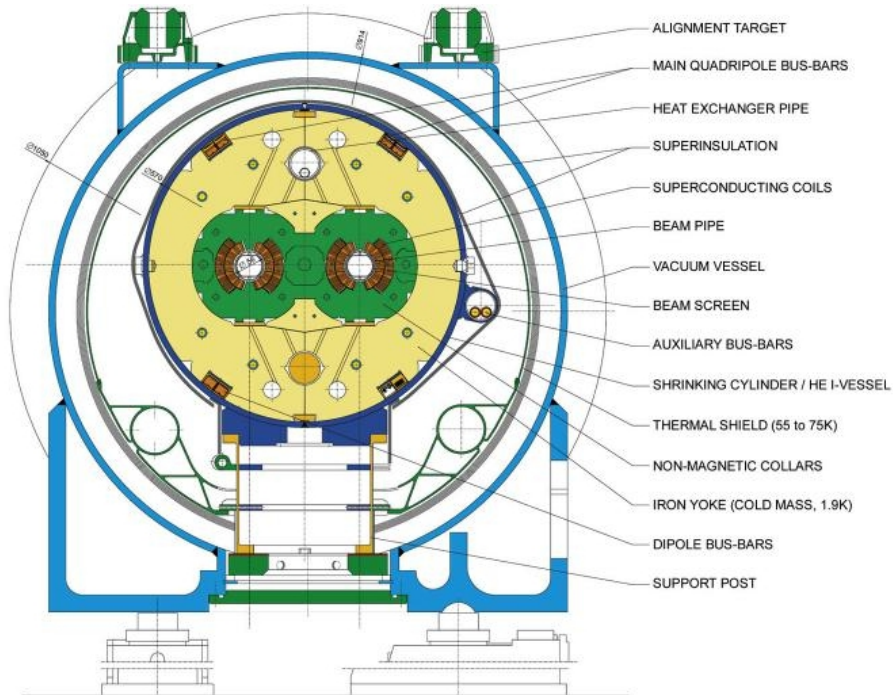


Figure 2.2: Standard cross-section of the LHC machine.

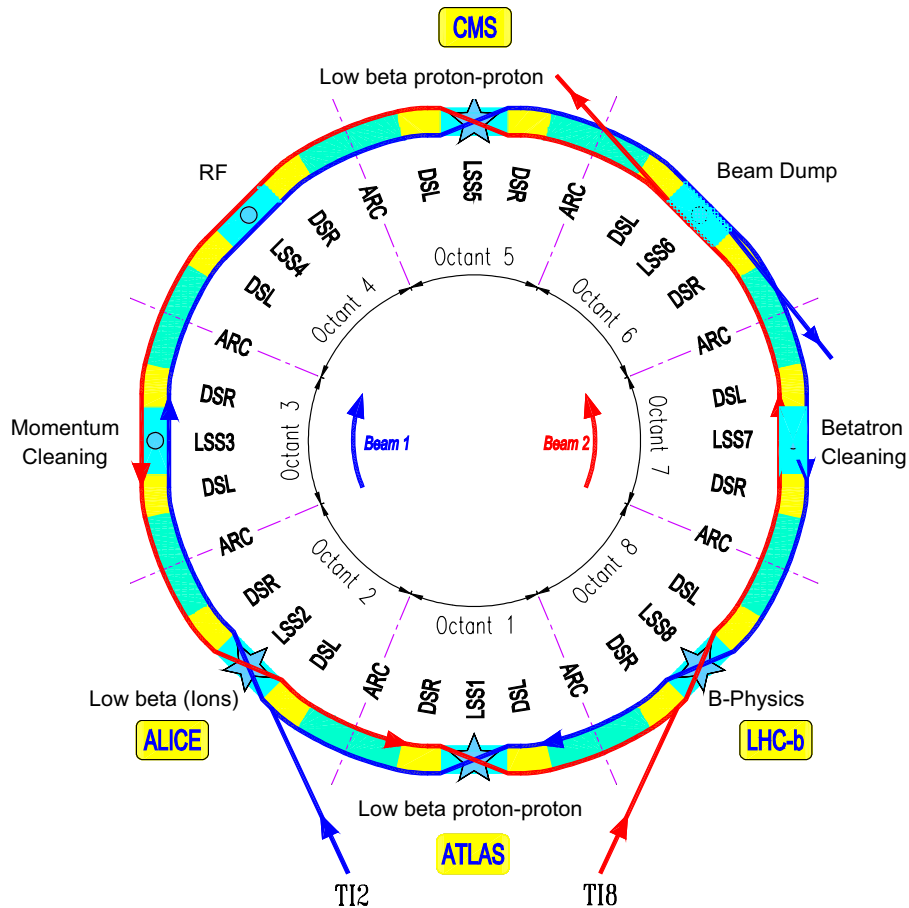


Figure 2.3: Schematic layout of LHC. In middle of the eight octants there are long straight sections which house experiments (ATLAS, ALICE, CMS and LHCb), collimation systems (Betatron and momentum cleaning), the RF cavities and the beam dump. Abbreviations: LSS long straight section, DSR and DSL dispersion suppressor right and left.

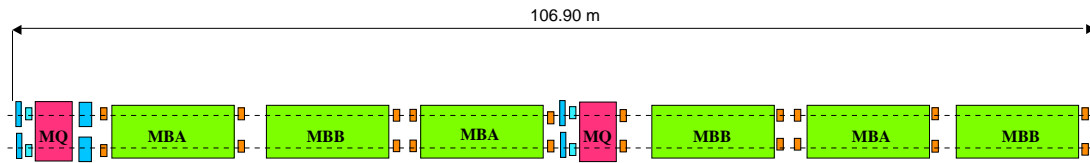


Figure 2.4: Layout of an LHC arc cell. Main bending magnets are denoted with MBA and MBB, lattice quadrupoles with MQ.

of higher order lattice magnets and corrector magnets is used.

In most of LHC, except for the experimental areas, the two beams circulate in separate beam pipes. In the arcs, the two beams are spaced horizontally by 194 mm. In the experiments the beams cross either in the horizontal or in the vertical plane.

## 2.2 Beam screen

Unlike other accelerators, where there is only one single beam pipe between the magnets and the beam aperture, LHC arc sections are going to be equipped with two coaxial pipes. This proved necessary due to the fact that LHC's superconduction bending magnets operate at a temperature of 1.9 K. Evacuating the heat load on the beam pipe induced mainly by image currents, beam losses, electron cloud and synchrotron radiation would be very expensive at such low temperatures. Therefore, there will be the so-called cold bore (1.9 K) in contact with the magnets and a thermally insulated beam screen (5 to 20 K) inside the cold bore (Fig. 2.5). Intercepting a major part the heat load at 20 K considerably reduces the cost of refrigeration.

For the propagation of microwaves above waveguide cut-off inside the beam aperture we have to focus our attention mainly on the beam screen. It is manufactured with specially developed stainless steel of 1 mm thickness. On the inner surface there is a 75  $\mu\text{m}$  copper coating to minimize the impedance seen by the beam-induced image currents [11].

The beam screen cross-section is circular with 46.4 mm inner diameter, with two flattened sides 37 mm apart. It is covered with 8 rows of axial pumping slots to allow the evacuation of residual gas. The slots are on average 8 mm long, 1 mm wide and cover about 4.4 % of the beam screen surface. To avoid resonances in the 10 GHz range the lengths of the pumping slots and the distance between them were randomized. This pseudo-random pattern repeats every 50 cm.

Since the protons in LHC are accelerated up to several TeV, synchrotron radiation cannot be neglected as in other hadron machines. At design energy (7 TeV) the critical energy of the synchrotron radiation falls in the UV range. To avoid this light being reflected around the ring, the inner surface of the beam screen is covered on one side with saw-teeth like corrugations. Due to the manufacturing process a small welding strip (less than 2 mm wide) will stay on the side opposite to the corrugations [12]. On the outside of the beam-screen two stainless steel cooling tubes are welded to ensure an operating temperature between 5 and 20 K. Recently, a metallic shielding between the flat part of the beam screen and the cold bore was added to the design to prevent electrons from the electron cloud from escaping through the pumping slots and depositing

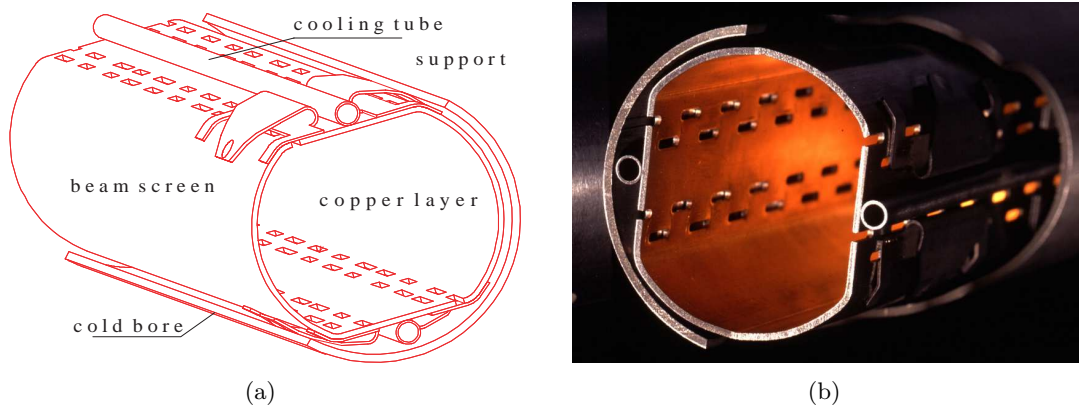


Figure 2.5: The LHC beam screen with the surrounding cold bore, the pumping slots and the cooling tubes.

their energy directly on the cold bore.

### RF properties

The properties of the beam screen as a waveguide at microwave frequencies were amply studied in [7]. Here we only give a short roundup. For propagation of microwaves there are basically two important parameters,

- the cut-off frequencies  $f_c$  of the various modes and
- the attenuation of each mode.

These two parameters were obtained in measurements on a single beam screen without cold bore, cooling tubes or pumping port shield using a resonator method.

For reflectometer measurements, in general we are not interested in propagating two modes at once. Therefore it is important to choose the correct frequency range, which is influenced by the cut-off frequencies of the different modes. The detection range is given, among others, by the waveguide attenuation. Only the first two TE and TM modes were extensively studied in the resonator measurements. For higher order modes the measurements become increasingly difficult due to the large number of modes propagating in the beam screen. However, simulations could reproduce the measured cut-off frequencies to a very high precision. Thus, when it comes to the cut-off frequencies of the higher order modes, we can rely on the simulations.

It was not attempted to simulate the attenuation of the beam screen. The higher order modes' attenuation can only be roughly estimated from the available data. Among many loss mechanisms, the wall current distribution in the region of the slots has a crucial impact on the waveguide attenuation.

### Cut-off frequencies

Before starting the discussion of the results, the notation of the waveguide modes has to be clarified. The beam screen has a cross-section similar to an elliptic waveguide.

Number	Mode	Simulated $f_c$ [GHz]	Measured $f_c$ [GHz]
1	TE <sub>c11</sub>	3.624	3.614 ± 0.0005
2	TE <sub>s11</sub>	4.350	4.325 ± 0.002
4	TE <sub>c21</sub>	6.160	
5	TE <sub>s21</sub>	6.827	
7	TE <sub>01</sub>	8.537	
8	TE <sub>c31</sub>	8.903	
10	TE <sub>s31</sub>	9.021	
11	TE <sub>02</sub>	10.83	
3	TM <sub>01</sub>	5.326	5.333 ± 0.0007
6	TM <sub>c11</sub>	7.947	7.987 ± 0.0005
9	TM <sub>s11</sub>	8.941	
12	TM <sub>c21</sub>	10.85	

Table 2.1: Cut-off frequencies of the first 12 modes on the slotted beam-pipe. The measurement uncertainly given is standard deviation of the set of individual measurements.

For this reason, an analog notation will be used. For instance, the fundamental TE mode that has its electric field lines parallel to the shorter side of the beam screen will be called TE<sub>c11</sub>. This mode corresponds to the TE<sub>11</sub> in the circular waveguide. The subscript *c* designates *cosine* polarisation, that is, an E field parallel to the shorter side of the beam screen. The second TE mode is then denoted TE<sub>s11</sub> for *sine* polarisation. The first TM mode on the beam screen corresponds to the first TM mode on both circular and elliptic waveguides and will be named TM<sub>01</sub> as usual. The mode patterns of the first modes on the beam screen are shown in Fig. 2.6.

The cut-off frequencies of the first modes are given in Table 2.1. The simulated values were obtained with the 3D simulation code Microwave Studio. To keep the geometry simple, only the cross-section was modelled. We used a geometrical model approximating the typical beam screen dimensions: a diameter 46.4 mm round tube with flattened sides 37.0 mm apart. The sharp edges are rounded off with 4 mm blending radius but this has only little impact on the simulated  $f_c$ . The welding strip and 3-dimensional structures such as the pumping slots and the saw-tooth shaped corrugations were neglected. The discrepancies between simulation and measurement results are fractions of a percent and thus acceptable. They could be due to mechanical measurement precision, systematic measurement errors and inaccuracies of the model or simulation.

### Attenuation

Since the beam screen is not an ideal waveguide, it can be expected that its properties are different from waveguides, as well. Mainly the pumping slots are responsible for the high attenuation of some modes. It was shown elsewhere [41] that the waveguide modes do not change their mode pattern much in presence of slots. So if a mode has azimuthal wall currents at the position of the slots, they will be interrupted. Displacement currents than take over: the slots radiate. Looking at the mode pattern of the different waveguide modes, some observations can be made.

- TE mode wall currents always have azimuthal components.

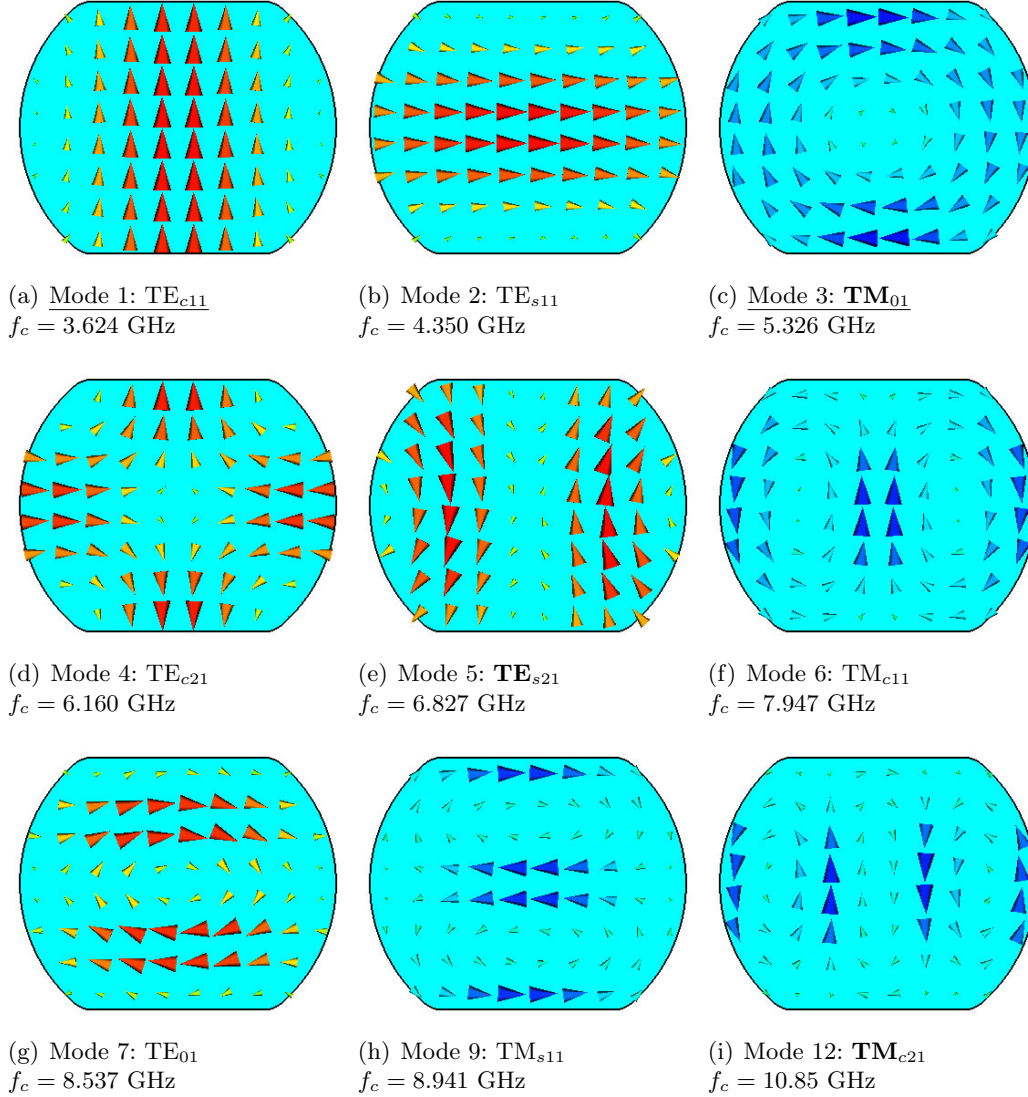


Figure 2.6: Waveguide modes on the LHC beam screen. For TE modes the E field (reddish) and for TM modes the H field (blueish) is plotted. The quoted cut-off frequencies are the simulated values. Modes with  $\text{TM}_{01}$  symmetry (horizontal and vertical H symmetry plane) were printed in bold face, the first higher order mode with  $\text{TE}_{c11}$  symmetry (horizontal E and vertical H symmetry plane) is the  $\text{TE}_{c31}$  mode with cut-off at 8.87 GHz.

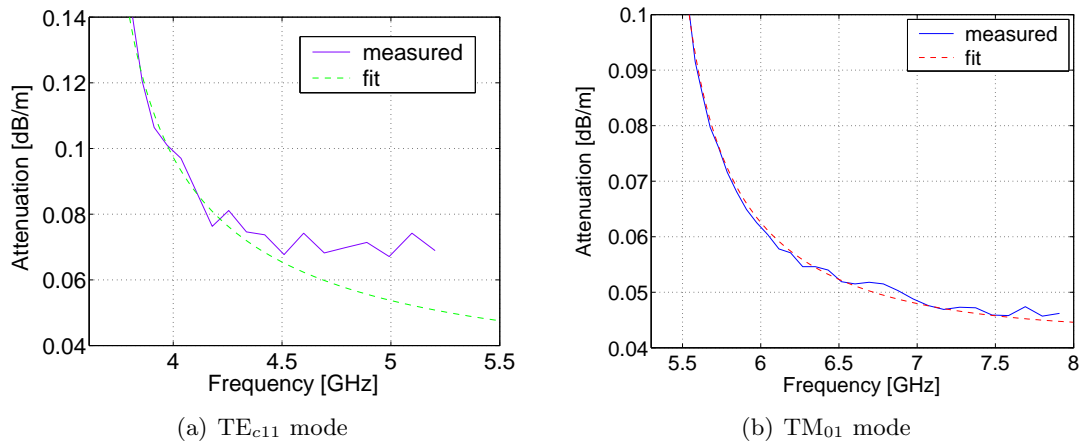


Figure 2.7: Attenuation of the first TE and TM mode

- TM modes have exclusively axial wall currents.
- The  $TE_{c11}$  mode has rather small azimuthal wall currents compared to the  $TE_{s11}$  mode.

From the above qualitative reasoning we can conclude that TE modes will be attenuated much by radiation losses, whereas TM modes should only suffer low attenuation. However, it has to be heard in mind that the resonator measurement in [7] was conducted with a “naked” beam screen sitting on a table. Installed in the cold bore with the pumping slot shields in place 2 mm away from the beam screen [42], the radiation losses through the slots can be expected to be considerably smaller.

Fig. 2.7 shows the attenuation of the first TE and TM mode. The measurement results are compared to curves predicted by theory for copper waveguides of similar geometry. The cut-off frequency represents a fixed point for a waveguide. For this reason the waveguides used for the comparison were chosen to have the same cut-off frequency as the beam screen. For the  $TE_{c11}$  mode a rectangular waveguide with approximately the same side ratio was used, since the E field is rather similar to the  $TE_{10}$  mode in a rectangular waveguide. When it comes to the  $TM_{01}$  mode, the H lines are parallel to the conductive surface, looking more like the  $TM_{01}$  mode in a circular profile, so a circular waveguide was chosen for comparison.

This leads to theoretical curves that should ideally have the same shape as the measured data. However, due to parasitic effects such as surface roughness and impurities in the conducting layer the measured curve is normally offset by a constant factor. By fitting this single parameter in the frequency band close to cut-off, these parasitic effects can be accounted for. Since resistive losses are high in the region, radiation losses will be comparably small, having a small impact on the quality of the fit. Higher attenuation can also be expected to come from the different waveguide profile as compared to the models.

An important difference can be noted between the two plots. For the  $TM_{01}$  mode the measured curve has the same shape as the theoretical prediction. For the fitting parameter we got about 1.35, which means that the attenuation was about 35 % higher than the theoretical curve over then entire frequency range. This offset is perfectly

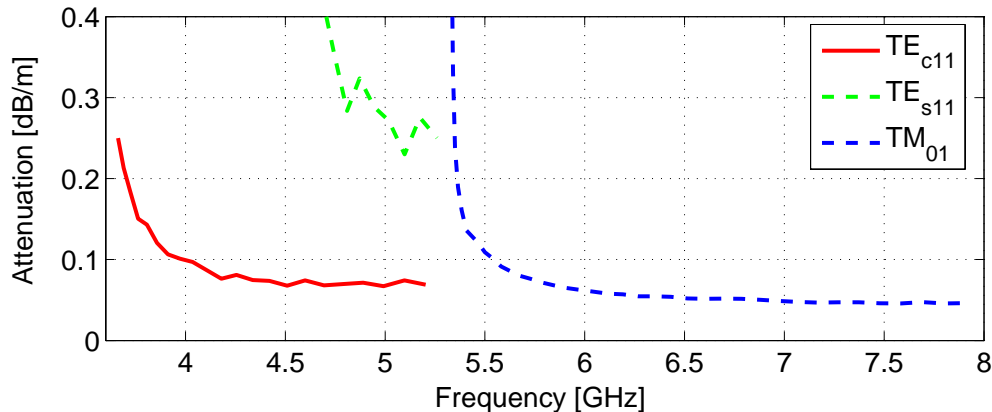


Figure 2.8: Comparison of the measured attenuation of the first three modes. Please note the massive attenuation of the  $TE_{s11}$  mode.

normal even for standard waveguides. For commercial copper C-band waveguide, the attenuation was found to be about 10 % higher than predicted. Only above 7.5 GHz the curve appears to flatten somewhat. On the other hand, the  $TE_{c11}$  mode curve flattens already at about 4.5 GHz. This effect is without doubt caused by the radiation losses taking over. Contrary to the usual resistive losses that decrease with frequency<sup>1</sup>, radiation losses increase with frequency. Therefore, a considerable part of the observed losses is due to radiation.

In Fig. 2.8 the losses of the first three modes are compared. Obviously, the  $TE_{s11}$  mode with its high azimuthal wall currents around the slots radiates a lot. Measurements for the TE modes were only conducted below the cut-off of the  $TM_{01}$  mode to avoid its strong interference. It can be assumed that the attenuation of the  $TE_{c11}$  mode rises slowly in the frequency range between 5 and 7 GHz. Assuming that the radiated power goes with the square of frequency, an attenuation of about 0.09 dB/m can be expected at 7 GHz. The  $TM_{01}$  attenuation measurement was limited by the second TM mode entering the game at 8 GHz. At 8.7 GHz three additional data points (not in the plot) could be taken, showing an attenuation of about 0.0457 dB/m. The curve is expected to continue falling towards 0.045 dB/m at 9 GHz and then rise slightly. The minimum of the fitted theoretical curve is at about 9.3 GHz.

## 2.2.1 Properties at cryogenic temperatures

### Cut-off

When cooled down to its nominal operation temperature (between 5 and 20 K), some properties of the beam screen change dramatically. This is certainly not the case for the cut-off frequency. The coefficient of thermal expansion for stainless steel is about  $17\mu\text{m}/(\text{m}\cdot\text{K})$  at room temperature. Coming close to absolute zero, it decreases. When cooled down from 293 K to 20 K, type 304 stainless steel contracts by 0.304 % [19]. This makes the cut-off frequencies increase by the same amount to about 3.625 GHz for the  $TE_{c11}$  and 5.349 GHz for the  $TM_{01}$  mode. This effect has to be kept in mind,

<sup>1</sup>Of course the resistive losses have a local minimum at some frequency but it is way above our frequency range.

since it will entail a perceivable change of waveguide dispersion.

### Attenuation

Operation at cryogenic temperatures has one considerable advantage. The impedance seen by the image currents will be low. The beam screen specification requires the RRR<sup>2</sup> of the copper layer to be below 80 at DC [45]. High purity copper is used for the 75  $\mu\text{m}$  thick coating. However, during the production process impurities diffuse from the steel pipe into the copper layer. The concentration of these impurities decreases with the distance from the copper-steel surface, but on the outer copper surface diffusion stops and the foreign atoms pile up. For the small penetration depths of the order of 0.1  $\mu\text{m}$  at microwave frequencies an RRR of about 20 appears realistic [47]. The Ohmic losses would thus drop by about a factor 4.5, assuming we are in the classic skin effect regime. It will be pointed out later that this is not the case. With the resistive dissipation in the copper decreasing, other loss mechanisms get more important, especially

- ohmic resistance in the welding strip
- radiation losses
- microscopic surface roughness.

The first two of these loss factors are estimated to account for about 10 % of the room temperature attenuation. Since they do not decrease with temperature, they will get more important at cryogenic temperatures compared to the resistive losses.

At cryogenic temperatures, for high frequencies, the mean free path length of the electrons is of the order of the skin depth. In this regime the surface resistance cannot be calculated any more using the classic formula [15]

$$R_S(f) = \sqrt{\pi f \mu_0 \rho} \quad (2.1)$$

with the resistivity  $\rho$ . Under these conditions the so-called anomalous skin effect appears. An empirical formula exists that describes the surface resistance in the cryogenic regime,

$$R_S(f) = R_\infty (1 + 1.157 \alpha^{-0.276}) \quad (2.2)$$

for  $\alpha \geq 3$ .  $R_\infty$  and  $\alpha$  are given by

$$R_\infty = \sqrt[3]{\frac{\sqrt{3}\pi}{4} \rho \mu_0^2 d^2} \quad (2.3)$$

and

$$\alpha = \frac{3}{2} \left( \frac{d}{\delta} \right)^2 \quad (2.4)$$

where  $d$  designates the mean free path length and  $\delta$  the classic skin depth

$$\delta = \sqrt{\frac{1}{\pi f \mu_0 \sigma}}, \quad (2.5)$$

---

<sup>2</sup>The residual resistivity ratio (RRR) is the ratio of a sample's resistivity measured at room temperature to the resistivity measured at temperature of liquid helium (4.2 K). The RRR depends heavily on the material's purity.

with  $\sigma = 1/\rho$  designating the conductivity. The conductivity of copper at room temperature is  $\sigma = 5.9 \cdot 10^7$  S/m. The mean free path length of an electron can be calculated from [18]

$$d = \frac{\sigma m \nu_F}{n e^2} \quad (2.6)$$

with the electron mass  $m$ , the Fermi speed  $\nu_F$  and electron volume density  $n$ . Evaluating the above formulas for copper at 20°C we find with  $\nu_F = 1.57 \cdot 10^6$  m/s and  $n = 8.46 \cdot 10^{28}$  m<sup>-3</sup> for the mean free path length  $d = 3.9 \cdot 10^{-8}$  m. Since  $d$  is proportional to the conductivity, it increases by the value of the RRR at cryogenic temperatures. In the following we assume an RRR of 20 in the outermost copper layer of the beam screen.

When the LHC dipole magnets are powered, the magneto-resistive effect will further increase the waveguide attenuation. It can be neglected at room temperature, but in the cryogenic regime the mean free path length of the electrons becomes comparable to the Larmor radius. When a magnetic field is applied, it increases the effective path length of the conduction electrons. For high magnetic fields and high frequencies, the resistivity can be described by the Kohler law [16]

$$\rho(B, T) = \rho_0(T) \cdot \left(1 + 10^{1.055 \log_{10}(B \cdot RRR) - 2.69}\right). \quad (2.7)$$

where  $B$  is the magnetic field,  $T$  the temperature and  $\rho_0$  the resistivity at temperature  $T$  without magnetic field. The resistivity thus obtained has to be plugged in the formulas for the anomalous skin effect given above.

In [15] and [44] the surface resistance of a tube with a co-laminated copper layer was measured at cryogenic temperatures. This technique was used for the beam screen, as well. The available data covers the frequency between 100 MHz and 2 GHz. It was tried to extrapolate the behaviour in the frequency range of interest (4 to 10 GHz). For measurements without magnetic field, the surface resistance found at 1.2 GHz was about 20 % higher than the values predicted by the anomalous regime theory.

At higher frequencies, a discrepancy between 0 % and 50 % appears possible. Assuming a 25 % increase compared to theory, the resistive part of the attenuation is found to decrease by a factor 3.0 over the entire frequency range, 4 to 10 GHz. For the TM<sub>01</sub> mode this means a substantial drop in attenuation. At room temperature, the TM<sub>01</sub> mode attenuation was found to be 0.0485 dB/m at 7 GHz. With an estimated 90 % of that coming from resistive losses, an attenuation of 0.0195 dB/m is expected in the cryogenic regime.

On the other hand, only roughly 40 % of the TE<sub>c11</sub> mode attenuation appear to stem from resistive losses. With a measured attenuation of 0.07 dB/m at 5 GHz, a rather small drop to about 0.051 dB/m can be hoped for.

When a magnetic field is applied, in general the magneto-resistive effect will increase the resistivity. Only for “small” magnetic fields the resistivity may decrease slightly. The measurements in [15] show pretty good agreement with theory. When ramping from  $B = 0$  to 8.4 T, the conductivity peaks at about  $B = 2$  T ( $\approx 5\%$  above normal), then decreases to about 5% below its value without magnetic field. This compares well to the 6% drop at  $B = 8.4$  T predicted by theory.

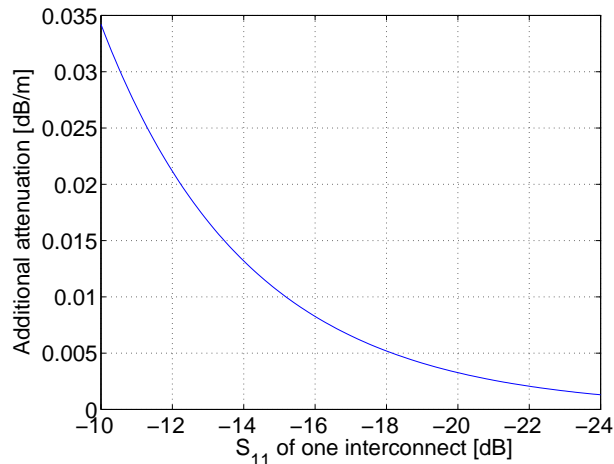


Figure 2.9: Additional attenuation due to power scattering by the interconnects

$TE_{c11}$	$TM_{01}$	T [K]	B [T]	Interconnects	Method
0.07	0.0485	300	0	No	Resonator measurement
0.105	0.06	300	0	Yes	Measurement on 50 m test track
0.085	0.028	20	0	Yes	Estimation
0.086	0.029	20	8.4	Yes	Estimation

Table 2.2: Overall attenuation in [dB/m] of the  $TE_{c11}$  mode at 5 GHz and of the  $TM_{01}$  mode at 7 GHz in the beam screen.

## 2.2.2 Overall attenuation

At this point, the attenuation being one of the most important design parameters, it appears appropriate to summarize all the present information about it. First, the properties of the beam screen were considered separately. However, the interconnects play an important role, as well, as will be discussed in the next section. By reflecting power, they effectively increase the attenuation seen by a wave propagating down the beam screen. The LHC arcs and dispersion compressor sections are composed of cells. The smallest unit is a half cell of length  $\approx 53.5$  m, consisting of three dipoles and one quadrupole. Therefore, there is on average one interconnect every  $53.5/4 = 13.375$  m. The additional attenuation  $\alpha_{add}$  can then be calculated as

$$\alpha_{add} = \frac{-10 \cdot \log_{10} \left( 1 - 10^{\frac{S_{11i}}{10}} \right)}{13.375} \quad (2.8)$$

with the interconnect reflection coefficient  $S_{11i}$ . This formula was evaluated in Fig. 2.9.

With an estimated  $S_{11}$  of  $-15$  dB for the  $TM_{01}$  mode and  $-10$  dB for the  $TE_{c11}$  mode, the interconnects are expected to contribute by 0.01 dB/m and 0.035 dB/m, respectively, to the overall attenuation.

Table 2.2 lists the current estimations of the overall line attenuation. The data taken on the 50 m test track confirmed estimations that took as a basis the attenuation of the “naked” beam screen and the interconnect reflections. The values given were obtained by measuring the peak reflection of a short circuit at the end of the 50 m line. However,

since no cold bore was installed on the 50 m test track, the  $TE_{c11}$  mode attenuation might be somewhat overestimated.

Coming to cryogenic conditions, here we have to rely on estimations presented in the previous section. For the  $TM_{01}$  mode a substantial drop in attenuation by a factor two is expected. The  $TE_{c11}$  mode attenuation should stay almost constant since already at room temperature the radiation through the slots accounts for most of the losses. Small temperature changes, in particular within the operational range of 5 to 20 K, should not result in large changes in attenuation. This is because the above loss mechanisms, including resistive losses, do not depend too strongly on temperature in cryogenic conditions. When the LHC bending magnets are ramped to their design field of 8.4 T, the resistivity should increase by about 6 %, leading to a noticeable increase in attenuation.

However, the uncertainties of the above estimations are hard to quantify. One weak point is the extrapolation of the surface resistance. It appears to be a safe assumption that the surface resistance will have the same properties at 2 GHz as at 8 GHz, but we simply do not know for sure. An RRR different from the one assumed should not make too big a difference in the anomalous skin effect regime. Another critical point are the reflections from the interconnects. There is reason to believe that their reflection coefficients in the machine may be smaller than what we found in our preparatory experiments. Especially after cool-down, when all the contact fingers are making contact, the  $TM_{01}$  mode reflections should decrease considerably.

### 2.3 Beam vacuum interconnects

In the LHC cold arcs, the bending magnets and the short straight sections housing quadrupoles and other correction magnets will have to be interconnected. The continuity of all the vital installations of LHC must be guaranteed, comprising cryogenic lines, vacuum enclosures, electrical power supply, thermal insulation and the beam screen. We will focus especially on the latter. In order to keep the machine impedance low, customary sliding RF contacts had to be developed, designed to have a DC resistance below 0.1 m $\Omega$  [13].

After installation, at ambient temperature, the contact fingers are in an undefined state, meaning that they are not necessarily closed [14], Fig. 2.10. During cool-down to 1.9 K, the cryomagnets contract by about 40 mm and the contact fingers slide into position.

The contact fingers are integrated in a so-called *plug-in module* that is inserted *after* the magnet installation. The gap between two dipole magnets is only  $160 \pm 6$  mm long, between a dipole and SSS it can be a bit longer (up to  $167.5 \pm 6$  mm). At their extremities, all the LHC arc elements have one standardised 98 mm diameter flange. This flange exists in two versions: *upstream* and *downstream* designate the sides where the beam enters and leaves the plug-in module. Fig. 2.11 shows as an example the interconnect between a main bending magnet and a short straight section. Main bending magnets always have standard flat beam screen interface (upstream flange, cut G). SSS have the same interface on the upstream side and a circular 48 mm diameter interface on the downstream side (downstream flange, cut B) for the beam position monitors.

For installation, the plug-in module is compressed and fitted between two LHC ring components, for instance two dipoles. The beam screen then enters the plug-in module about 5 mm deep in its groove. A good RF contact is provided on the front side of

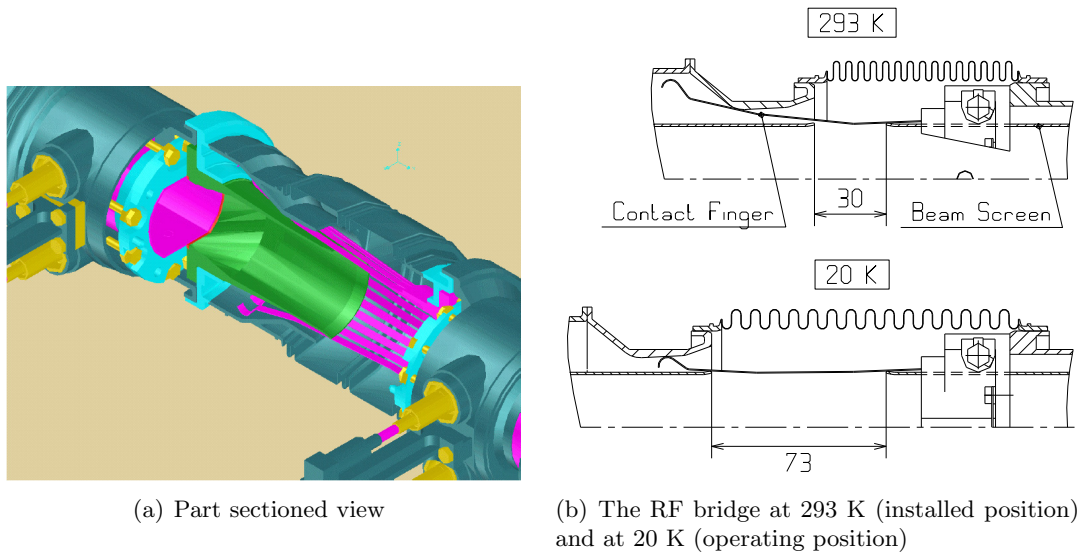


Figure 2.10: The plug-in module of the beam vacuum interconnect

the beam screen and sideways to the small spring contacts. To avoid corrosion and to reduce the contact resistance, the extremities of the beam screen are gold-plated.

### RF properties

The RF contact fingers were optimized to keep the machine impedance as low as possible. The azimuthal image currents will see the contact fingers only as a tiny perturbation. The same is true for TM waveguide modes, since their wall current distribution is very similar to the image currents. Thus the TM wave will be well guided and the field component close to the stainless steel bellows will be very low. With exclusively very good conductors (copper and brass) seen by the wave, it can be supposed that the losses in the interconnect are negligible. Therefore the RF properties of the interconnect can be characterised by measuring the reflection only. However, it did not prove easy to measure these reflections. For the  $TM_{01}$  mode, in the range between 6 and 8 GHz a reflection coefficient between  $-25$  and  $-10$  dB was found. The properties were strongly frequency-dependent due to the fact that for the electromagnetic wave, the interconnect looks like two independent reflections; one at each transition between the beam screen and the contact fingers. Also the a priori unknown gap length plays a very important role. However, the interconnects used in the measurements were not of the final design and modified for practical reasons [7]. In another measurement series, on an almost 50 m long test track including two interconnects, an averaged reflection coefficient of about  $-15$  dB was found. For this evaluation, the interconnect's reflection coefficient was extracted from a long trace by time domain gating.

No dedicated measurements were performed for the  $TE_{c11}$  mode, but it could be assumed that the impact of the interconnect is still more important. This was confirmed in the measurement series on the 50 m test track. A reflection of roughly  $-10$  dB was found for the interconnects. With high reflections and their exact properties so diffi-

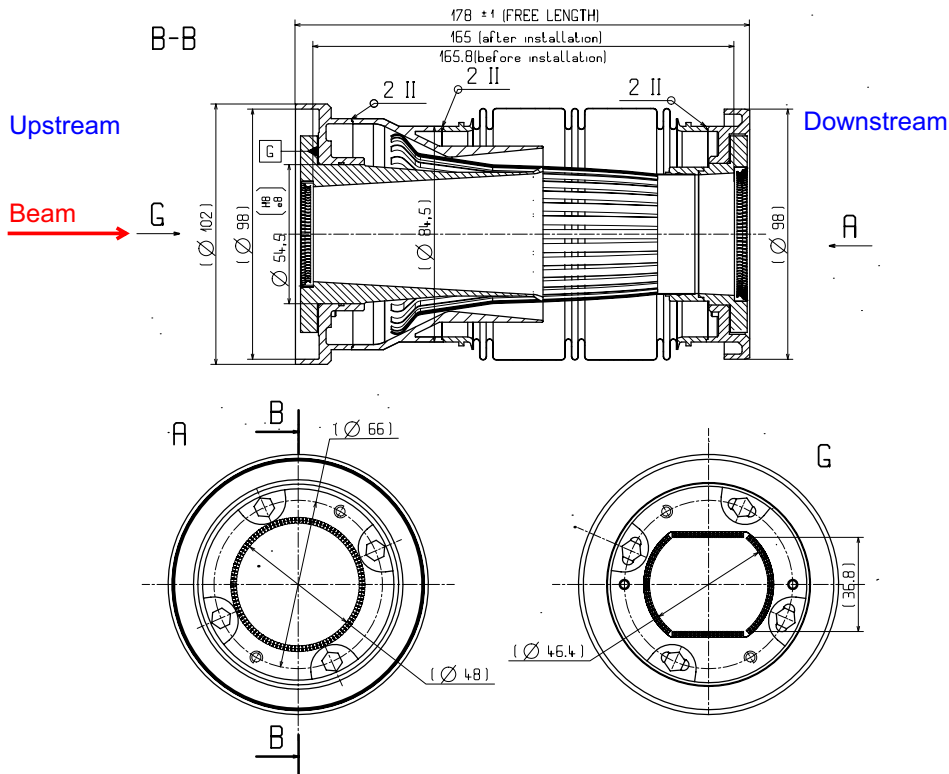


Figure 2.11: Design drawing of the beam vacuum interconnect between an arc dipole (cut G) and a short straight section (cut A).

cult to determine, the interconnects could become a major limiting factor for both the reflectometer's range and sensitivity.

## 2.4 Installation and commissioning

In the cold arcs the general infrastructure is installed first. Among the most important components are the cryogenic distribution lines, which transport the liquid helium from the cryoplant on the surface to the magnets in the tunnel. Thereafter the installation of the LHC machine cold mass begins. In general the magnets are tested on the surface, then moved into the tunnel, aligned and interconnected. Space in the tunnel is scarce, as can be seen in the image in Fig. 2.12.

In the present plan (January 2005) the installation and commissioning will start with sector 7-8 (arc between point 7 and point 8). Before full machine commissioning, a test with beam is foreseen in this sector. This will allow to verify the correct design and installation of many vital components and systems. Only beam 2 will be used, coming from the SPS via the TI8 transfer line, it will go through IR 8 (interaction region 8) and run along sector 7-8. In IR 7, the beam will be stopped by a temporary beam dump. This test is currently scheduled for May 2006. It should last for about two weeks. Only very low intensity beams (pilot bunch with  $5 \cdot 10^9$  protons) will be used in order to keep the irradiation of the equipment low. This first test with beam is an interesting opportunity for checking the reflectometer and microwave beam diagnostics

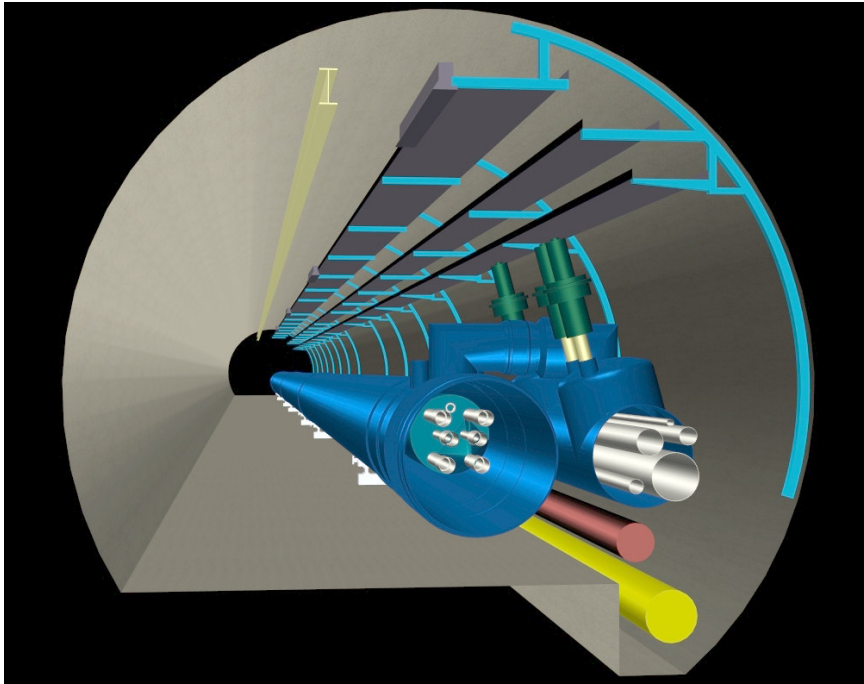


Figure 2.12: A typical view of the LHC tunnel. The left part is reserved for material transport with a monorail train that runs suspended on the yellow rail on the ceiling.

presented in this work.

**Part II**

**LHC reflectometer**

## Chapter 3

# Concept

In the past, during the commissioning of most major accelerators, strange objects have been found in the beam pipe. This may be contact fingers of badly installed interconnects, metal rulers, cleaning towels or even beer bottles. There is a non-vanishing probability that this may happen again in CERN's latest project, LHC. Due to the huge cold mass of the arc sections, any intervention in such a region would be very time-consuming and costly. But with the means at hand, even finding an obstacle once LHC is finished would be extraordinarily difficult. Special care will be taken during the assembly of the elements of LHC to prevent having obstacles, but from experience things do not always go the way they are supposed to. Therefore, there is a strong interest to have a means to detect and localize such obstacles. Having a check during installation and another one after finishing the LHC without breaking the vacuum, would both be interesting. The next chapters present the work done on the *Assembly Version* for inspection during the installation and the *In Situ Version* for diagnostics with the LHC under vacuum. The development work was focused on the long arcs, since they are the most inaccessible regions of the LHC.

Various methods can be thought of for detecting and localizing obstacles in an accelerator beam pipe. After outlining the possible options, we will concentrate on microwave time domain reflectometry, which was found to be the most straightforward approach.

### 3.1 Methods for obstacle detection

The stringent cleanliness requirements in LHC immediately rule out robot-mounted cameras or similar means. Additionally, such devices could eventually get stuck, causing even greater trouble. Therefore, any approach for obstacle detection has to proceed without "direct" contact to the beam pipe.

A number of techniques are currently used in remote sensing, such as

- Ultrasonic pulse-echo
- Laser reflectometry
- Microwave reflectometry

The use of ultrasonic waves would require gas in the beam pipe, while laser reflectometry is not satisfying due to its limitation in range. Additionally, it cannot cope with the

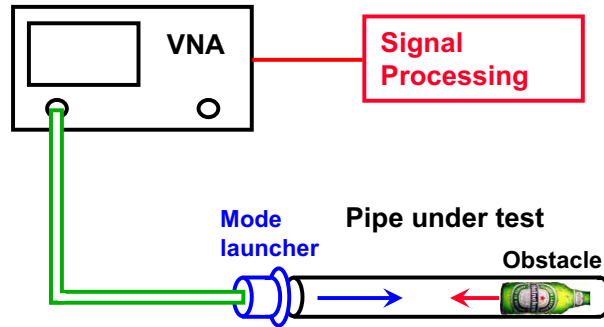


Figure 3.1: Set-up of a synthetic pulse waveguide reflectometry measurement

rugged surface at the outer side of the beam pipe that is meant for trapping synchrotron light. However, in the right frequency range microwaves will be guided in the beam pipe, thus providing low attenuation and long range. Three kinds of microwave reflectometry were considered:

- FMCW<sup>1</sup> “radar”
- Real time pulse reflectometry
- Synthetic pulse reflectometry

The latter approach was chosen for various reasons. One important point is that synthetic pulse reflectometry can be implemented using a commercial network analyser. This way offers a high dynamic range and one does not have to invest lots of manpower in developing front-end measurement equipment. Another advantage comes from the fact that since network analyser measurements are done in the frequency domain, the waveguide dispersion can be compensated in a very straightforward way. This is not the case for FMCW and real time pulse reflectometry, which are otherwise heavily used in non-dispersive media such as air and space.

## 3.2 Synthetic pulse reflectometry

Synthetic pulse reflectometry is one of the methods readily used for example in telecommunications network inspection, geophysics and printed circuit testing. An inspection of an accelerator vacuum chamber of several meters length is reported in [8]. The typical measurement set-up is sketched in Fig. 3.1. A vector network analyser is connected via a cable and mode launcher to the pipe under test. The measurement data is then processed externally. In this approach the device to inspect is considered as a black box and the reflection response from one or two ports is measured in the frequency domain. Calculating the Fourier transform reveals the profile of the reflections in time and, for homogeneous non-dispersive lines, in space. However, in the LHC beam screen unlike in air or on coaxial lines, dispersion has to be taken in consideration. This effect can be corrected numerically on the measurement data, if the cut-off frequency of the waveguide is known over its entire length. Obviously, this correction method can be applied in a very straightforward manner for homogeneous structures, such as the LHC

<sup>1</sup>Frequency Modulated Continuous Wave

beam screen.

On a homogeneous line with several discrete discontinuities, multiple reflections will turn up. For instance, two inhomogeneities at  $x = 2$  and  $x = 3$  meters from the end of the line will produce a rat-tail of multiple reflections seemed to be located  $x = 4$ ,  $x = 5$ , etc meters. If the individual inhomogeneities are small enough, then the magnitude of the multiple reflections will be small and can be neglected. However, if there is only one larger reflection, the signal will be corrupted and ways of recovering the correct reflection profile have to be considered.

### 3.2.1 Resolution

The resolution is one of the major parameters of a time domain reflectometry system. In our case, however, it is not of utmost importance to be able to distinguish between two similar closely spaced peaks. Rather we are interested in seeing obstacles in the smooth beam screen. Still, there is some interest in detecting small peaks, that is, potential obstacles close to larger inhomogeneities, such as the interconnects.

The resolution in time domain is inversely proportional to the frequency bandwidth used. For this reason it is always tried to maximize the bandwidth  $\Delta f$ , even at the cost of higher overall insertion loss or reflections from the coupling element. In the following, we stick to the 6 dB notation, that is, a given peak width designates the 6 dB impulse bandwidth. In dependence of the window function used in the Fourier transform, the impulse width ranges within  $1.2/\Delta f$  and  $2.8/\Delta f$ , corresponding to a Kaiser window with  $\beta$  between 4 and 13. Small values of  $\beta$  seem beneficial on first regard, since they allow to keep the main lobe width small. However, this comes at a price. The side lobes will increase, and even worse for long range measurements, the far-away side-lobes will drown the signal from the end of the line. For measurements over short ranges (up to 100 m), Kaiser windows with  $\beta$  down to 6 can be used. When longer ranges are needed,  $\beta$  must be increased at least to 9 or 11. With this information the 6 dB impulse length can be calculated as

$$\Delta t = \frac{k}{\Delta f} \quad (3.1)$$

with a constant  $k \approx 1.9$  for  $\beta = 6$  and  $k \approx 2.5$  for  $\beta = 11$ . In order to get the spatial resolution from that,  $\Delta t$  has to be multiplied with the wave's group velocity over two. In a waveguide, the group velocity is not constant, so an appropriate mean over the frequency range has to be used. The group velocity  $v_g$  in dependence of the cut-off frequency  $f_c$  is given by [10]

$$v_g = c_0 \sqrt{1 - \left(\frac{f_c}{f}\right)^2} \quad (3.2)$$

with the speed of light in free space  $c_0$ . It was empirically found that the quadratic mean of  $v_g$  fits best for dispersion compensation, so it can also be applied to calculate the delay.

$$\bar{v}_g = c_0 \sqrt{1 - \left(\frac{f_c}{f}\right)^2} \quad (3.3)$$

Mode	Freq. range [GHz]	$\overline{v}_g/c_0$ [%]	$\beta = 6$	$\beta = 11$
TE <sub>c11</sub>	4 to 6	67.5	9.6 cm	12.6 cm
TE <sub>c11</sub>	4 to 6.6	71.0	7.8 cm	10.2 cm
TE <sub>c11</sub>	4 to 7.0	73.0	6.9 cm	9.1 cm
TM <sub>01</sub>	6 to 8.0	63.9	9.1 cm	12.0 cm
TM <sub>01</sub>	6 to 9.0	68.9	6.5 cm	8.6 cm
TM <sub>01</sub>	6 to 10.5	74.1	4.7 cm	6.7 cm

Table 3.1: 6 dB Impulse width in reflection mode for two typical values of the Kaiser parameter  $\beta$ .

Bandwidth setting	$\beta = 6$	$\beta = 11$
3 dB	0.73	0.72
6 dB	1	1
20 dB	1.68	1.74
40 dB	2.07	2.30

Table 3.2: Comparison of the impulse width for different definitions, normalized to the corresponding 6 dB bandwidth.

The 6 dB impulse width  $\Delta x$  is then given by

$$\Delta x = \frac{k\overline{v}_g}{2B} \quad (3.4)$$

with the frequency bandwidth  $B$ . It was evaluated for several cases of interest in Table 3.1.

For the reflectometer it is interesting, as well, how close a small obstacle can be to e.g. the coupling element or an interconnect without being drowned in the big neighbouring peak. With interconnects having reflections of the order of  $-15$  dB, the 20 dB bandwidth is the decisive parameter. Otherwise, especially in assembly measurements, the case of the far beam screen extremity sealed with a protective cap might arise. This cap is made of metal and acts quite like a short circuit. For detecting a close-by obstacle, the peak's 40 dB bandwidth is important. In Table 3.2 these bandwidth values are listed.

### 3.2.2 Range & Sensitivity

In this part two other performance parameters of a reflectometer are treated, the spatial range and the sensitivity, given by the minimum detectable signal. Generally speaking, the spatial range depends on two parameters, (1) the network analyser's dynamic range and (2) the attenuation on the line. For the available instrument, an Agilent E8358A, the dynamic range in the frequency range of interest (about 6 to 9 GHz for the TM<sub>01</sub> mode) is about 115 dB. This value was found using an IF bandwidth of 100 Hz. However, this information has to be considered carefully. In fact, the network analyser has an in-built range switching that allows its ADC (Analog to Digital Converter) to use its full range. In principle, the maximum signal amplitude in frequency domain is set to maximum gain before digitization in the ADC. For reflectometer operation, we are mainly interested in the time domain data. Thus, the dynamic range cited above has to

be interpreted as the difference between noise floor in time domain and the maximum incident signal. This means that by minimizing the total signal, the level of the noise floor can be decreased. When measuring on the LHC beam screen, we will encounter the reflections of the interconnects. Since they cannot be avoided, this will pose a limit to the reflectometer performance. However, the farther away from the network analyser, the more line attenuation these reflections will see. Conversely, discontinuities close to the network analyser port will have a direct impact onto the dynamic range. Thus, in order to prevent further losses in dynamic range, a very low-reflection transition between the network analyser and the beam screen is needed. In practice, these coupling elements should be at least as good as the interconnects in terms of broad-band reflection coefficient. Thus, for the measurements, the available dynamic range is given by the difference between the instruments's dynamic range and the amplitude of the highest reflection.

With an obstacle having a reflection coefficient of  $S_{11o}$ , the range  $R$  can be expressed as

$$R = \frac{\text{Dynamic range of network analyser [dB]} - \text{Maximum reflection [dB]} + S_{11o}}{2\alpha} \quad (3.5)$$

with  $\alpha$  designating the one-way line attenuation in dB/m. For example, an obstacle with  $S_{11o} = -20$  dB can be detected on the E8358A network analyser (dynamic range @ 100 Hz IF bandwidth 115 dB) using the  $TM_{01}$  mode (room temperature attenuation 0.06 dB/m) and a reasonably well-matched coupler (maximum reflection = -10 dB) at

$$R = \frac{115 \text{ dB} - (-10 \text{ dB}) + (-20 \text{ dB})}{2 \cdot 0.06 \text{ dB/m}} = 875 \text{ m}. \quad (3.6)$$

Slightly longer ranges are possible by choosing smaller IF bandwidths, but at the price of a longer measurement. The assumed amplitude of the minimum reflection  $S_{11o}$  could be considered as a kind of sensitivity. However, the above considerations do not tell whether a small reflection can be seen above the noise floor. Apart from the thermal noise, two kinds of background signal have to be distinguished:

- Numerical noise from calibrations. Calibrations are a very useful tool for removing numerically the effect of transmission lines and discontinuities. It is possible for example to move the reference plane of the measurement to the end of the coaxial cable that is connected to the coupling element. A more sophisticated technique is waveguide calibration, which makes it possible even to set the reference plane to the extremity of the beam screen. However, since approximations are unavoidable and mechanical contacts are not perfectly reproducible, calibrations introduce errors. These deviations tend to increase with time and with the number of mechanical manipulations. In the time domain, they manifest themselves by an increasing noise level.
- Multiple reflections. All the discontinuities “naturally” existing on the beam screen, such as interconnects, produce reflections. Waves scattered an odd number of times still end up running back to the network analyser, where they show up as phantom reflections. Another reason or incentive for developing well-matched coupling structures is to keep these phantom reflections low.

### 3.2.3 Obstacles

At this point it is necessary to define what we understand by an obstacle. It is an object disrupting the continuity of the beam screen in some way. Physically, this may correspond to a change in beam screen geometry, conductivity, dielectric permittivity or even susceptibility as seen by the electromagnetic wave in the beam screen. Slow variations of these parameters over distances much longer than the wavelength (roughly 10 cm) cannot in general be detected in reflectometer operation. Examples of obstacles that give significant reflections are

- local deformations of the beam screen
- pieces of copper coating coming off the wall
- interconnect contact fingers sticking into the aperture
- metallic objects, such as screws or nuts
- other objects, such as cleaning towels or cigarette butts

A couple of test obstacles were studied in more detail, as is described in the chapter about the Assembly Version.

## 3.3 Summary

Among the different methods discussed for obstacle detection in accelerator beam pipes, microwave synthetic pulse reflectometry turned out to be the most promising candidate. Measurements are performed on a vector network analyser, which allows accurate control of most parameters and good reproducibility. Thereafter, the obtained data can be easily treated numerically. In the following parts of the chapter, the main performance parameters resolution, range and sensitivity are introduced and estimated for a typical synthetic pulse reflectometry system. Resolutions of the order of 10 cm and ranges approaching 1 km were found for operation on the LHC beam screen. The chapter closes with a clarification of what we understand by the term “obstacle” in the present context.

## Chapter 4

# Reflectometer Assembly Version

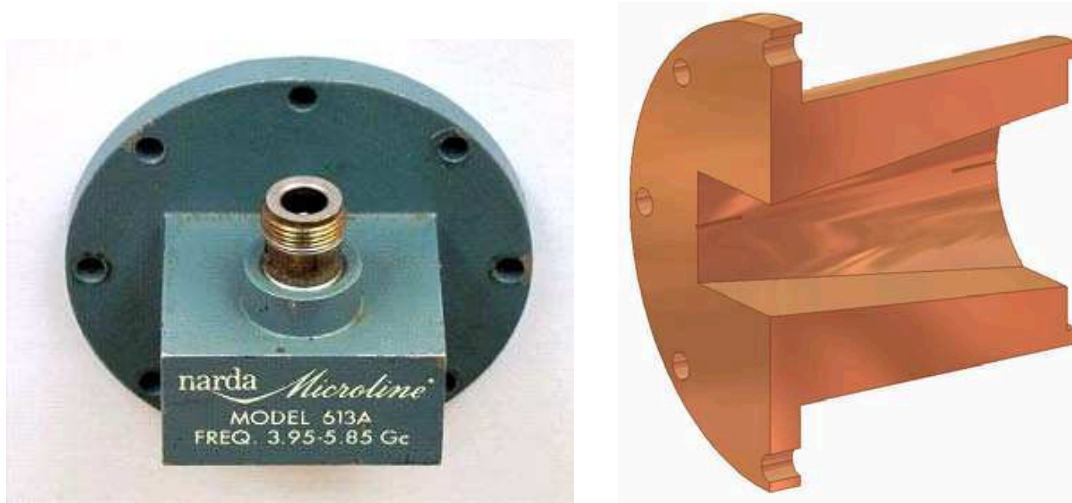
There is a special risk of the emergence of obstacles in the LHC beam screen during the first installation. It would therefore be advantageous to check that all beam screen sections are clean immediately before the magnets are interconnected. In cooperation with CERN's AT-VAC group that is responsible for quality insurance of the beam vacuum interconnections, a strategy was worked out. Tests of single dipoles are planned to make use of an optical method with polarized light, developed at the Krakow University of Technology. The Assembly Version of the microwave reflectometer is planned to be used for entire LHC cells as depicted in Fig. 2.4 for a final check and verification of the correct installation of the interconnects.

Both the  $TM_{01}$  and the  $TE_{c11}$  mode can be applied, since the targeted ranges are relatively small, so the higher  $TE_{c11}$  mode attenuation is not a limiting factor. Two independent measurements become possible this way, which adds to the reliability of the results.

In the following we will take a closer look to the design of the coupling modules. They provide the link between the network analyser and our device under test: the beam screen. The goal is to design couplers with minimal reflection coefficient  $S_{11}$  under the given mechanical and budgetary constraints. The reflection coefficient will be averaged over a frequency range of interest, that is, the range where the reflectometer is operated for the respective mode. As pointed out in the introduction (Fig. 2.11), the available space at the position of the plug-in modules for inserting our couplers is very limited. Including mechanical tolerances, no more than 154 mm in length is available between two adjacent dipoles. This space could be further reduced by protective caps temporarily installed on the extremities of the beam screen. The present design is based on a maximum coupler length of 120 mm. This allows easy mounting after removal of all protective caps. An ultra-short design allowing the use of the coupler even with the protective caps in place on the next dipole, would have seriously compromised the couplers' RF performance.

### 4.1 TE mode coupler

The  $TE_{c11}$  mode being the fundamental mode on the beam screen can be easily used in mono-mode operation. However, the wider the operational frequency band, the higher the obtainable resolution. For this reason it has been tried to maximize the frequency bandwidth by choosing overmoded operation [17].



(a) Commercial C-band waveguide adapter for the  $TE_{10}$  mode

(b) Customary transition from flat rectangular waveguide to beam screen.

Figure 4.1: The two components of the  $TE_{c11}$  mode launcher

As a rule of thumb, on a waveguide the lower frequency limit should be chosen between  $1.1f_c$  and  $1.2f_c$ , which corresponds to about 4 to 4.3 GHz for the  $TE_{c11}$  mode ( $f_c = 3.614$  GHz). The minimum frequency was chosen as close to cut-off as possible for two reasons. First, obviously, a higher resolution can be obtained this way. The second point is that aperture constrictions will be much more visible at frequencies close to cut-off.

For the maximum frequency there is no sharp limit. Rather it will get more and more difficult to get a spurious-mode free excitation for increasing frequencies. Operation up to 7 GHz with acceptably low spurious modes was achieved with the present design. In the following, when speaking about the  $TE_{c11}$  mode operational frequency range, we mean the range between 4 to 7 GHz.

The adopted design consists of two components. For the actual excitation a commercial C-band coax to waveguide transition was used (Fig. 4.1(a)). Then a smooth transition that opens up to the wider beam screen profile is necessary (Fig. 4.1(b)).

This approach has several advantages. In the first place, only the transition to the beam screen has to be manufactured, the C-band adapter can be purchased from industry. That saves times and resources. Having said that, it is also easier to excite the fundamental  $TE_{c11}$  mode in a waveguide with flat profile. Let's consider again the modes propagating on the beam screen, Fig. 4.2.

In the beam screen, due to its pretty round shape, the mono-mode region is very small, having a width of only a bit more than 600 MHz. It is hard to avoid the  $TM_{01}$  mode when trying to excite the  $TE_{c11}$  mode. On the C-band waveguide on the other hand the  $TE_{10}$  is the only propagating mode in a bandwidth of more than 3 GHz. It can thus be fed in a very pure way. Even though specified only for the band between 3.95 and 5.85 GHz, it can be used with a not too high degradation in performance up to 7 GHz. The  $TE_{20}$  and the  $TE_{01}$  mode are not excited as a consequence of symmetry reasons. A sharp limit is 7.5 GHz, where the  $TM_{11}$  starts propagating in the rectangular waveguide.

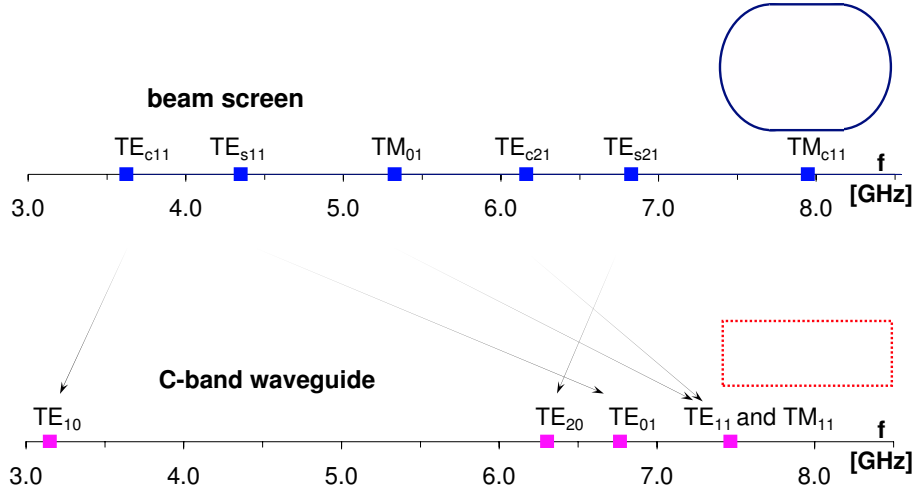
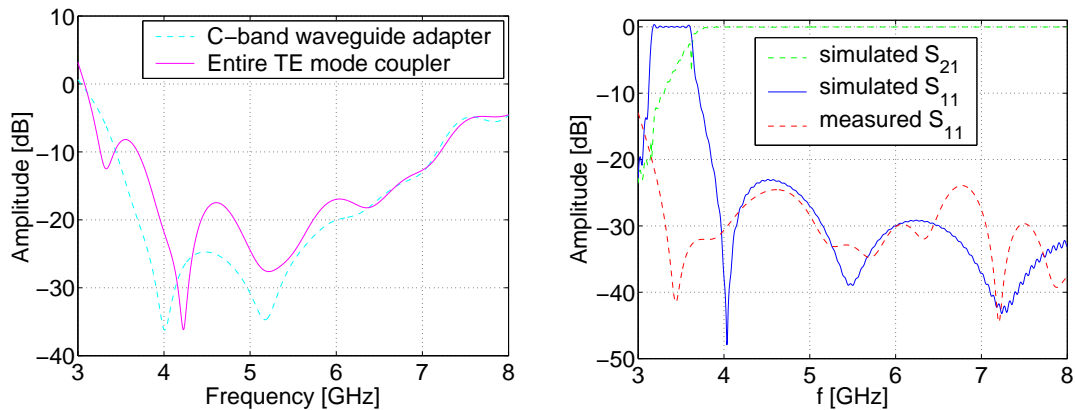


Figure 4.2: The corresponding modes on the beam screen and in a C-band waveguide.

After its excitation, the  $TE_{10}$  mode propagates through the smooth matching piece that widens up to the beam screen. Like in a horn antenna, higher order modes will be excited at the beginning of this transition region. The matching piece has two symmetry planes, the horizontal and the vertical centre plane. Combined with the fact that the incoming  $TE_{10}$  mode's electric field is perpendicular onto the horizontal centre plane and its magnetic field is perpendicular onto the vertical centre plane, we can conclude that only modes having the same symmetry will be excited much. However, the first mode that fulfills this condition is the  $TE_{c31}$  with cut-off at 8.87 GHz, far above our frequency region of interest. These theoretical considerations were confirmed in simulations, provided the transition piece is smooth and not too short.

The simulated and measured performance of the TE mode coupler are plotted in Fig. 4.3. The reflection coefficient of the complete coupler was not simulated, because the exact properties (geometry, dielectric constant) of the C-band adapter at hand were hard to pin down. Fig. 4.3(a) shows that the overall performance is determined mainly by the C-band adapter. A slight increase in  $S_{11}$  due to the transition piece cannot be avoided, either. The two bumps at  $\approx 4.7$  and  $\approx 6$  GHz are obviously coming from the transition to the beam screen cross-section. In this measurement, the fully assembled TE coupler was connected to the network analyser via a 1 m long coaxial cable. By one-port calibration, the reference plane was set to the cable's end connector. At the other side of the cable, a long piece of beam screen was inserted to simulate operation conditions. Since reflections from the end of the beam screen and even from the slots cannot be avoided, time domain gating was used to extract the frequency response of the coupler's reflection.

The simulation results agree very well with measured data, as can be seen in Fig. 4.3(b). To separate the reflection of the C-band adapter from the transition piece's in time domain, a 43 cm long piece of C-band waveguide was inserted between the two. Thereafter, gating was applied to get the transition piece's frequency response. The low-frequency components below 4 GHz are smeared out by dispersion on the C-band waveguide, otherwise there is a pretty satisfactory agreement between the measured and the simulated  $S_{11}$ . Concluding, we found a weighted average of  $S_{11}$  of about  $-20$



(a) Measured reflection coefficient of the C-band coax to waveguide adapter and of the complete TE coupler.

(b) Simulated  $S_{11}$  of the transition piece in Fig. 4.1(b) compared to measurements.

Figure 4.3: Simulated and measured performance of the TE mode coupler. The measurements were performed with one-port calibration at the coax connector using time domain gating onto the element's reflection.

dB for a 3 GHz bandwidth between 4 and 7 GHz.

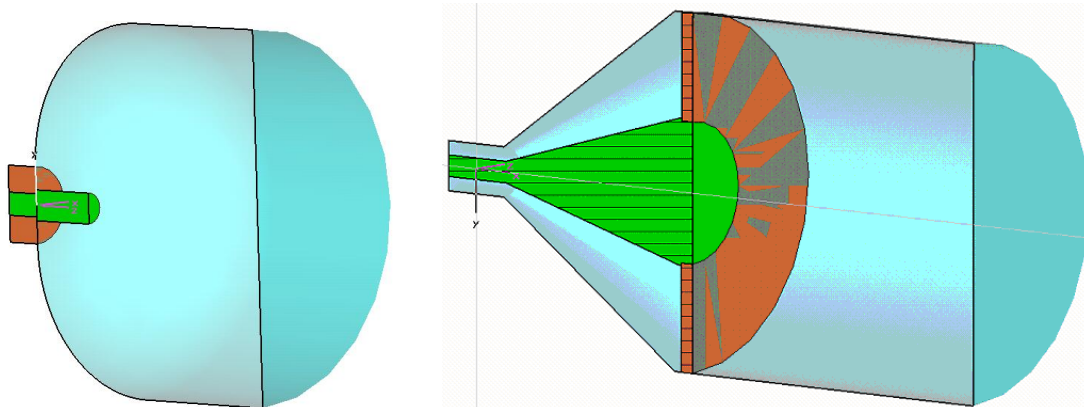
## 4.2 TM mode coupler

To work with the  $TM_{01}$  mode on the beam screen implies working on an overmoded waveguide. However, due to its special mode pattern, the  $TM_{01}$  mode can be excited in a very pure way. On the beam screen, the next TM mode having the same symmetry is the  $TM_{c21}$  mode with cut-off at 10.85 GHz (mode pattern in Fig. 2.6). With  $TM_{01}$  cut-off at 5.326 GHz, there is potentially a very large band-width of about 5 GHz available. However, a very good spurious-mode free mode launcher is necessary to exploit it. The lower frequency limit will be at about 6 GHz to avoid the high waveguide attenuation and dispersion close to cut-off. Coming to the upper frequency we are currently limited by the network analyser at hand, which works up to 9 GHz but most considerations are valid for higher frequencies, as well. For the TM mode coupler, our operational frequency range extends therefore over 3 GHz, from 6 to 9 GHz.

Various designs for the TM mode coupler were checked in the first simulations. All approaches relied on exciting the  $TM_{01}$  mode in a circular waveguide and then adding a transition piece to the beam screen. The option of building a mode launcher having the shape of the beam screen was abandoned for its overwhelming mechanic complexity.

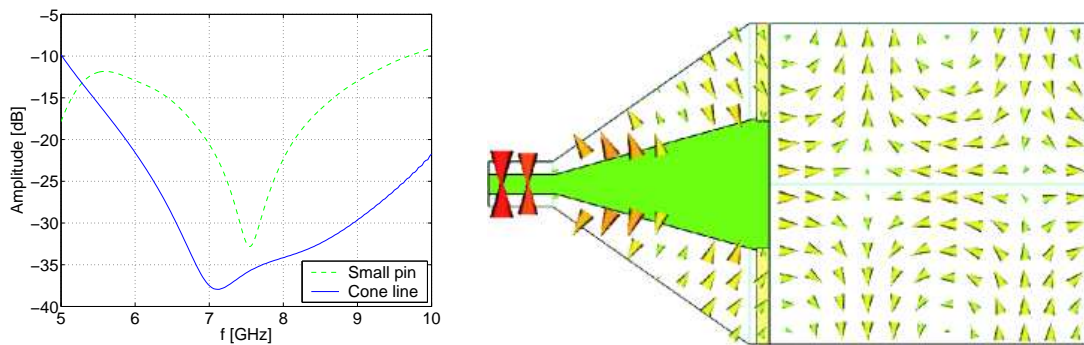
In a circular cross-section the  $TM_{01}$  mode is characterized by a perfect rotational symmetry. Every good mode launcher has to respect this symmetry. Inspired by the similarity between the TEM field pattern of the coaxial line and the  $TM_{01}$  mode, we tried a very straightforward approach: some rotationally symmetric transition from a coaxial line to a circular waveguide. Sketches of the two basic designs are shown in Fig. 4.4.

The first geometry considered consists of a relatively small pin reaching into a circular waveguide. A similar coupler has been widely used for the preparatory measurements. A theoretical treatment describing this approach was found in [46]. However,



(a) Structure using a small axial pin as coupling element. (b) More complicated design with coaxial cone transition. The pattern in the dielectric disk comes from the display under Microwave Studio and has no special meaning.

Figure 4.4: Coupling structures examined for the TM mode coupler. Dielectric is colored orange, conductor green and air blue, background material is a perfect conductor, too.



(a) Simulation of the  $S_{11}$  of the two couplers in Fig. 4.4. (b) Electric field pattern of the cone-type coupler at 7 GHz.

Figure 4.5: TM mode coupler

simulations on a model of the type sketched in Fig. 4.4(a) did not yield very satisfactory results in terms of bandwidth and matching. The second approach was inspired by the well known cone transition that is used for low reflection diameter changes on coaxial lines (4.4(b)). This way the wave is smoothly guided from the small coaxial line to the waveguide. It was found that the lowest reflections can be obtained not with some fancy excitation pin but by simply letting the inner conductor stop short at the right place. For both designs the parameters were optimized in the operational frequency range. It turned out that the cone-type coupler offers significantly better performance, see Fig. 4.5(a). This led to the decision to build a prototype on the basis of the cone-type coupler. The smooth transition to the circular waveguide is illustrated in the screen-shot from the simulations in Fig. 4.5(b).

A mechanical design drawing of the TM mode coupler is given in Fig. 4.6(a). On the left, the network analyser can be connected with a coaxial cable. Then the TEM wave runs through the cone line and couples to the TM mode. On the right side, a 6 cm long

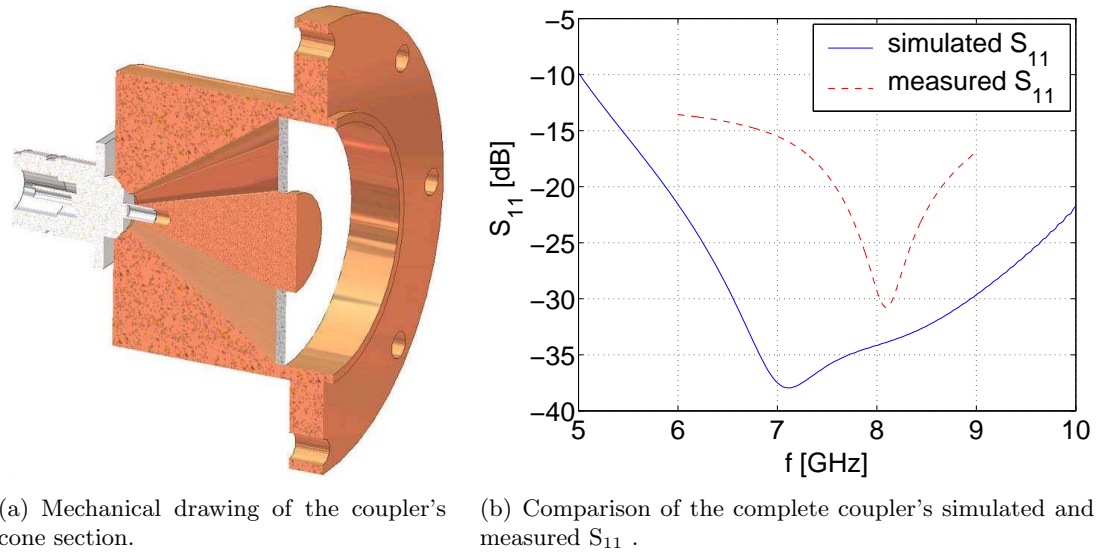


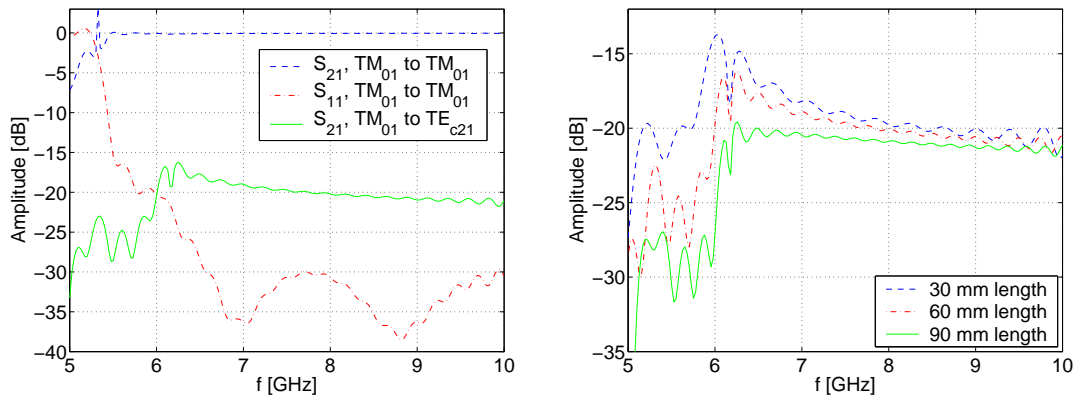
Figure 4.6: Implementation of TM mode coupler.

smoothly contracting transition piece ending in the beam screen profile is connected. A prototype of this coupler was built and tested. The results compared to the outcome of the simulations are depicted in Fig. 4.6(b). Obviously the measured  $S_{11}$  did not fully meet the expectations. The main reason for this is probably that in the region close to the tip of the cone, small mechanic uncertainties and contact resistances have a strong impact. For the present design, the weighted average over the operational range is about  $-21$  dB.

Unlike the TE mode coupler, for the  $TM_{01}$  mode we expect rather strong higher order mode excitation in the transition to the beam screen. To understand this, the symmetry planes of the  $TM_{01}$  mode in a circular and in the beam screen profile have to be examined. Like the  $TM_{01}$  mode, there exist two symmetry planes, the horizontal and the vertical plane. Both are of the magnetic type, that means, the magnetic field is normal on these planes. Unfortunately, the  $TE_{c21}$  mode has the same properties, and is can propagate on the beam screen above 6.160 GHz. The mode conversion between these two modes was studied in a series of numerical simulations.

For all simulations, the wanted  $TM_{01}$  mode was excited on the round side of the transition piece. Above 5.3 GHz most of the input power is transmitted by the wanted  $TM_{01}$  mode in the beam screen (Fig. 4.7(a), blue dashed trace). The reflection (to the same mode, the  $TM_{01}$  in the circular profile) is way below  $-20$  dB in most of the working frequency range (red dash-dotted trace). However, a part of the transmitted power goes to the  $TE_{c21}$  mode (solid green trace). Fig. 4.7(b) shows the impact of this effect as a function of the transition piece's length. Interestingly enough, making the transition piece longer does not diminish the mode conversion much, especially for higher frequencies (above 7 GHz or so).

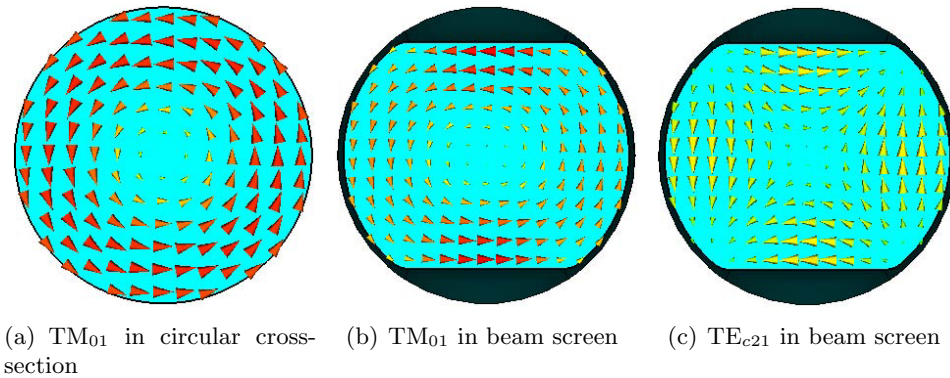
This can be understood by having a look at the mode pattern of the modes in question, Fig. 4.8. When the TM wave runs from the circular profile to the beam screen, its H field lines close to the flat parts of the beam screen are constricted. In free space or air, Maxwell's equations forbid discontinuities in the magnetic field, and so opposing



(a) The fundamental TM mode and the strongest higher order mode ( $TE_{c21}$ ) on a 60 mm long transition piece.

(b) Comparison of the excitation of the spurious  $TE_{c21}$  as a function of the transition piece length.

Figure 4.7: Simulation of the transition between the 50 mm circular waveguide and the beam screen.



(a)  $TM_{01}$  in circular cross-section

(b)  $TM_{01}$  in beam screen

(c)  $TE_{c21}$  in beam screen

Figure 4.8: Magnetic field of the modes involved in the observed mode conversion in the transition piece between circular and beam screen profile.

field components are excited for compensation. A part of them constitutes the  $TE_{c21}$  mode that propagates in both directions. Of course this result can be obtained in a more rigorous way by mode matching methods, but for our purpose a basic understanding combined with numerical simulation is sufficient.

### 4.3 Data processing

Most of the preparatory reflectometer measurements were performed on the Agilent E8358A network analyser. This network analyser runs Windows 2000 and can be connected to the LAN. Since it turned out to fulfil the various requirements, especially dynamic range, measurement speed and network connectivity, it was decided to build the data processing software around this machine. The built-in time domain option allows to calculate the reflection profile in time immediately. However, for large band-

widths and long lines, waveguide dispersion has to be corrected numerically. Other tasks, such as providing an graphical user interface, appropriate plotting, archiving, etc. needed a customary implementation, too. For these tasks, Matlab was found most appropriate. The Matlab application has a modular structure and can also be run on platforms other than Microsoft Windows. This guarantees that data from other network analysers can be treated with a minimum extra effort.

The interface to the network analyser is done in a few compact Visual Basic applications, which basically set the measurement parameters and store the results. All additional signal processing is performed in Matlab. After successful testing, Matlab functions can be compiled and run on the network analyser itself in stand-alone mode, provided the CPU load does not get too high. For instance, dispersion correction on measurement data from single dipoles could be processed without troubles. For longer sections or more complex signal processing task, the network analyser soon reaches its limits. Of course offline data processing is an option, but it would be highly desirable to have an ambulant instrument that can do fast diagnostics. The solution of choice is to have a portable PC for controlling the network analyser and doing the number crunching. This option was chosen for inspections during LHC assembly.

### 4.3.1 Basic functionality

On the network analyser the signal processing software can be run in parallel with the preinstalled network analyser application. This allows to keep maximum flexibility for the measurements. The network analyser control was implemented in Visual Basic. After start-up of the reflectometer application (reflec.exe), the empty project window appears, Fig. 4.9. There are basically three ways of performing measurements.

1. The ordinary Agilent network analyser program can be used. The data has to be saved (.s1p format) and subsequently imported into the reflectometer application.
2. By hitting the button labelled “Measurement”, one set of data is taken from the Agilent network analyser using its current settings. The data is displayed automatically in the reflectometer application.
3. Special measurement routines. When clicking on the button “Dipole”, a customized procedure for measuring the beam screen of a single dipole is initiated. The network analyser’s parameters will be set accordingly, in particular the frequency span.

### Dipole inspection

The functionality of the reflectometer application will be shown with an example: The inspection of the beam screen of a single LHC dipole magnet with the network analyser only. No external PC is used in this case.

- **Starting up.** Start up the network analyser first. Then make sure that the network analyser application (835x.exe on Agilent E8358A) is running and start the reflectometer application (reflec.exe). You will see the reflectometer startup window (Fig. 4.9).

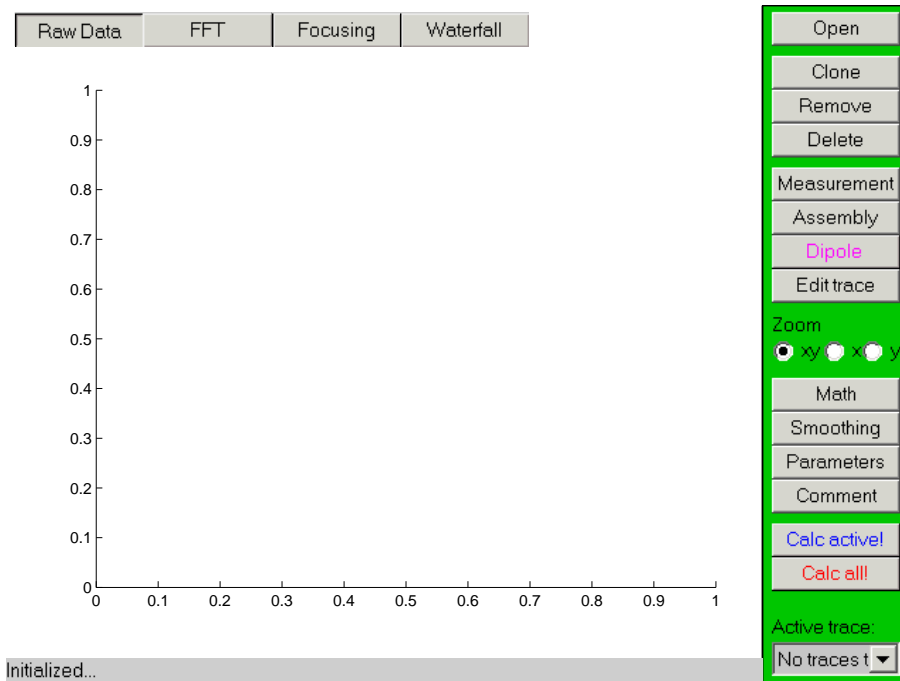


Figure 4.9: The reflectometer application after startup.

- **Initiating the measurement.** In the reflectometer window, push the “Dipole” button. Control will be handed over to a Visual Basic script that guides you through the measurement procedure.
- **TM mode measurement.** A dialogue window prompting you to connect the TM mode coupler will appear, Fig. 4.10(a). Connect the TM coupler to the extremity of the beam screen and then make sure that the coupler is connected by coaxial cable to Port 1 of the network analyser. When done, push “OK”.
- **Measuring.** The window in Fig. 4.10(b) appears. Depending on the settings of the network analyser, the measurement can take a few seconds to a few minutes.
- **TE mode measurement.** After the TM mode measurement terminates, you are prompted to connect the TE mode coupler, Fig. 4.10(c). Please do so and push “OK” when done.
- **Measurement finished.** The “Measuring...” window appears again while the measurement is performed. Finally, when the measurement procedure is finished (Fig. 4.10(d)), you can switch back to the reflectometer by hitting “OK”. If one of the measurements needs to be redone, you can go back to the previous step at any time by clicking “Back”.
- **Data analysis.** When the measurement is completed, the data is corrected for waveguide dispersion for each mode and plotted. A typical result is depicted in Fig. 4.13.

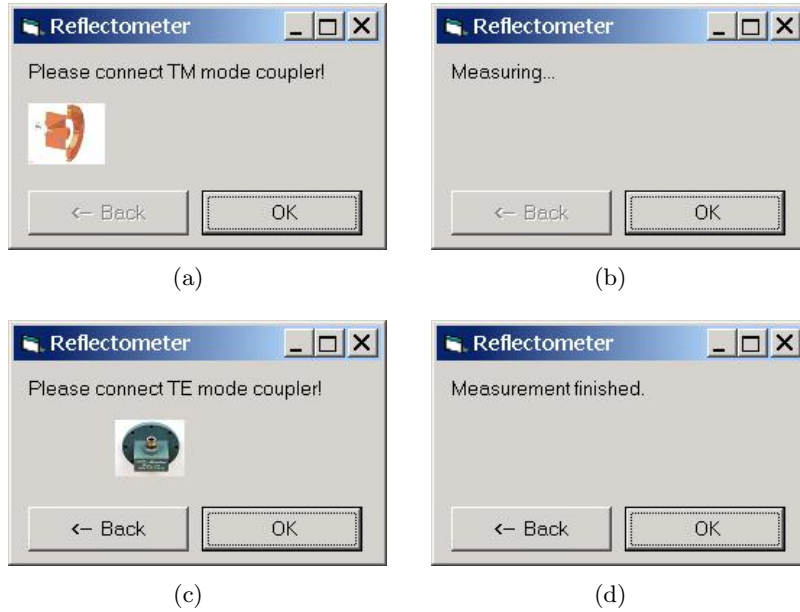


Figure 4.10: User dialog windows in an LHC dipole inspection.

### Data representations

The actual measurement being completed, we can now have a closer look at the data. Four different data representations are currently implemented, corresponding to the four tabs in the top of the reflectometer window.

- **Raw Data.** The data as measured on the network analyser. Several traces can be displayed simultaneously using difference display styles. Fig. 4.11 shows the data obtained with a TE and TM mode coupler on a single dipole. Please note the different but overlapping frequency ranges of the two couplers.
- **FFT.** The Fourier transform of the raw data. This corresponds to the time domain trace on the network analyser. Optionally, waveguide dispersion can be corrected for one distinct point in time. The first peak in Fig. 4.12 at  $t = 0$  s comes from the not perfectly matched mode launchers. At  $t \approx 1.5 \cdot 10^{-7}$  s we see the reflection from the far end of the dipole. Due to waveguide dispersion these peaks are pretty smeared out. On metallic waveguides, unlike e.g. in fibers, the group velocity always increases with frequency. In the present case, the TE mode appears to be both faster and more smeared out. This can be explained by comparing the TE and TM frequency ranges. Normalised to the respective cut-off, the TE frequency range was  $f/f_c = 1.11$  to  $1.83$  and the TM range  $f/f_c = 1.13$  to  $1.69$ . The TE wave arrives first because it contains higher and therefore faster frequency components. At the same time the normalized TE frequency span is larger, leading to wider peaks. The FFT tab is most interesting for development and maintenance of the reflectometer application and cross-checks with the network analyser.
- **Focusing.** Here the data corrected point by point for waveguide dispersion using Equation 3.3 is plotted. The correct waveguide cut-off frequency is needed for

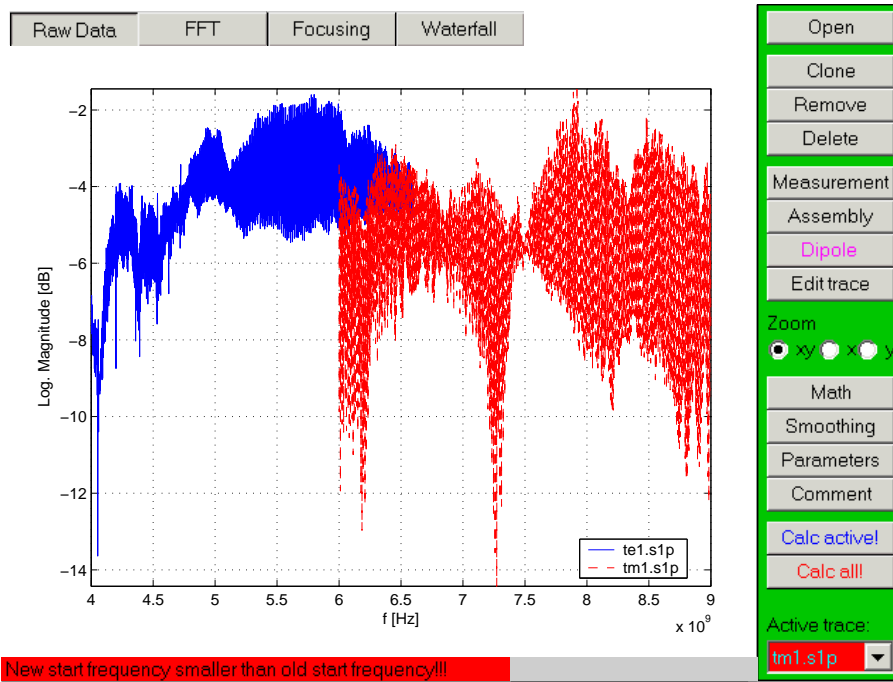


Figure 4.11: The raw data of the LHC dipole measurement in frequency domain.

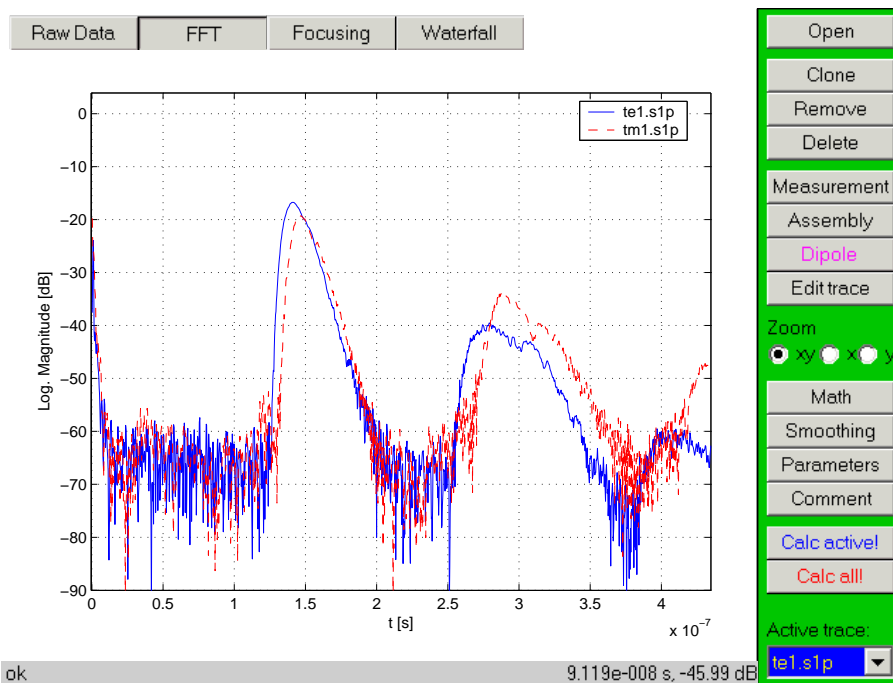


Figure 4.12: Data in time domain after Fourier transform. This plot corresponds to the time domain option on a network analyser.

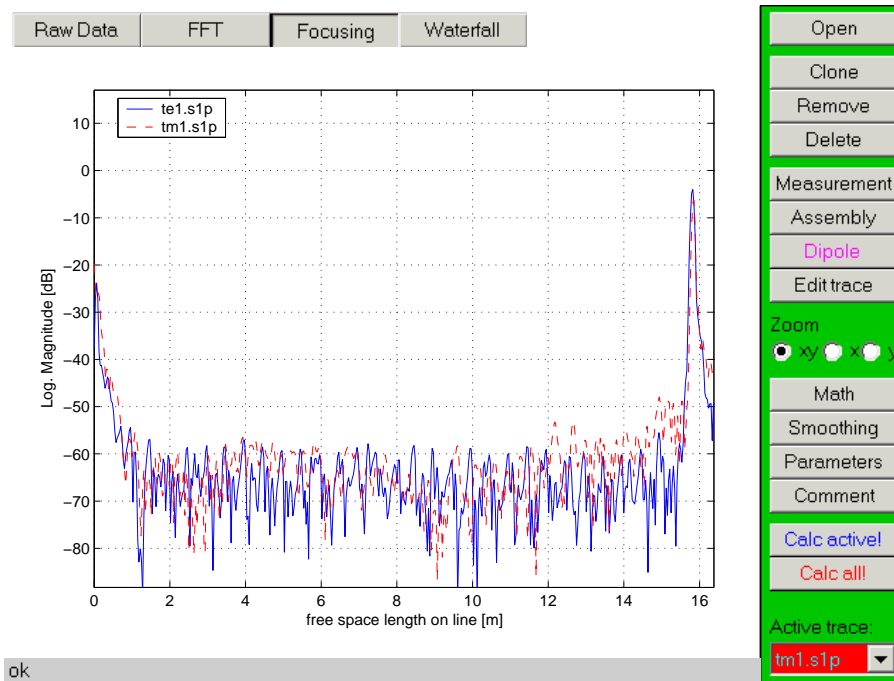


Figure 4.13: Dispersion corrected data for a single dipole in spatial domain. An exact knowledge of the modes' cut-off frequency is necessary for this focusing. The small coupler reflection can be seen at the beginning of the trace, while the end of the dipole shows up as a distinct peak. In between, the dipole is clean.

this calculation. It can be set under “Edit trace”. In predefined measurement procedures (e.g. “Dipole”) the cut-off frequency is set automatically. Fig. 4.13 shows the correctly focused data. It is interesting to note that

- the reflection from the end of the beam screen comes out as a sharp peak
  - both traces are almost on top of each other
  - the noise floor lies more than 40 dB below the reflection at the end, pointing towards very good sensitivity
  - there is a pattern in the TE mode noise floor with a period of about 50 cm, matching the slot pattern's length.
- **Waterfall.** Another nice way to visualise the dispersion correction is the waterfall plot. Like in the other plots the horizontal axis represents the distance on the line. Now the step-by-step focusing process is performed by moving the focus from zero to the maximum distance. The traces obtained are stacked in a matrix and displayed in a color plot. The points in focus are designated by a blue diagonal. This tool can be used to verify the correct setting of the cut-off frequencies and to check for mode conversion. In this plot, any mode other than the used  $TE_{c11}$  would not be in focus on the diagonal. Small features, like the 50 cm pattern come out only in the focused region. The waterfall feature has to be used with care, since huge matrices can be generated easily, entailing long calculation times.

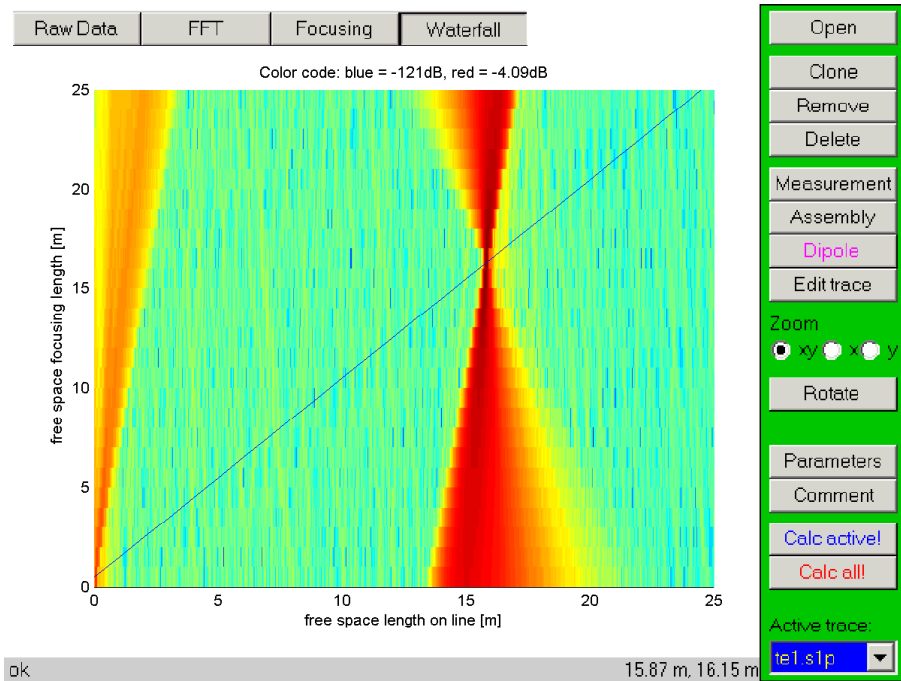


Figure 4.14: Waterfall plot illustrating the focusing operation. Points in focus should lie on the blue diagonal, if no mode conversion occurs.

## Utilities

At this point we should clarify the concepts used. The entire content of the reflectometer application constitutes a project. Projects can be opened, saved, deleted etc. under the menu item “Project”.

The expression “trace” is used not only for some curve in a plot but in a much more general way. A trace is the ensemble of all the attributes of one measurement, comprising name, data, cut-off frequency and many others. Most of the trace properties can be viewed and changed under “Edit trace”. All the operations concerning traces (clone, remove, delete and edit trace) apply to the currently active trace, which can be chosen in the popup field in the right button corner.

The traces are in contrast to the general parameters, such as the plot format and environment parameters like file paths. The latter can be modified using “Parameters”. A variety of practical manipulations can be done by the user. Most of them can be accessed via buttons in the button panel on the right.

### • Trace operations

- **Open.** Loads a data file from the disk and adds it to the traces already present. Per default, the trace attributes are initialized with those of the active trace.
- **Clone.** Makes a clone of the active trace.
- **Remove.** Removes the trace from the project.
- **Delete.** Removes the trace from the project and deletes the corresponding data file.

- **Edit trace.** Views and modifies trace attributes. The frequency limits of a trace can be changed within the original span. Data points outside the chosen range will be discarded. It is possible to select predefined values for the cut-off frequency by choosing the corresponding waveguide mode. The dielectric coefficient is taken into account only for TEM lines, otherwise it is assumed unity. Different window functions are available and the FFT resolution can be improved by zero padding of the raw data. An electrical delay can be specified to compensate the effect of a low-loss TEM line. Furthermore, it is possible to set the FFT focus. This is the point in time at which the trace should be focused. For the waterfall plot, the maximum range of calculation and the step width designating the distance between the focus points in two subsequent traces can be specified. Another interesting option is the clipping amplitude, which allows to set a lower limit for the magnitude in the waterfall plot. This helps to interpret the data by getting rid of irrelevant information.

Trace settings can be copied between traces for easier processing.

- **Predefined measurement routines**, like a single dipole measurement. Most of the important network analyser and trace parameters are set automatically.
- **Zoom.** It is possible to zoom into the plot in various ways with both the mouse and the keyboard. Please refer to the help for further information.
- **Math.** Simple but useful operations involving sets of traces are possible, provided the traces' frequency vectors are identical.
- **Smoothing.** Traces can be low-pass filtered along the abscissa. This feature corresponds in principle to the video bandwidth setting found on spectrum analysers.
- **Parameters.** Edits plot and environment parameters.
- **Comment.** Adds a comment to the project.
- **Calc active!** Recalculates and plots the active trace. This may help if some error occurs. In case it doesn't, try "Calc all!".
- **Calc all!** Recalculates and plots all traces except the hidden ones. If there is still some error persisting, go to the tap "Raw Data" and hit "Calc all!" again. Check if something is messed up in the trace properties. If it still doesn't work out, sorry, you'll have to restart the application.
- **Status line.** On the bottom of the application window a status line was added where important messages are displayed. Uncritical messages are displayed on the standard grey background or on green background, warnings appear on yellow background and errors on red background. For instance, it was tried to set frequency limits incompatible with the current data in the "Edit trace" utility. The error message issued is displayed in Fig. 4.11. When navigating in the plot with the mouse, the coordinates of the last mouse click are displayed in the right side of the status line, see Fig. 4.12.

## Help and shortcuts

For better usability most of the buttons and properties fields have little tool tips that appear when you point at it. To get help with the numerous zooming commands, please check out the “Help” menu. There are also shortcuts for most of the common operations, like “O” for opening data files or “Backspace” for removing a trace. They can be found in the “Help” menu under “Keyboard shortcuts”. For questions about other features have a look into the “Advanced features” section.

### 4.3.2 Advanced features

In addition to the basic features described in the previous section, several pretty useful special features were implemented. Among them are

- **Gating.** This function, accessible in the menu “Tools”, is an implementation of the gating function available on the network analyser. It makes it possible to analyze the frequency content of one single reflection. Even if this reflection is small, it can be studied separately, provided that it is not too close to another peak. On the network analyser, for data from waveguides, this technique is very limited by waveguide dispersion, which reduces the spatial resolution. However, in the present implementation, it can also be applied on the dispersion corrected data, thus allowing to analyse small peaks that would otherwise be drowned by dispersion-broadened neighboring peaks. The limits of the gate can be entered in seconds in the time domain trace and in meters in the focused trace.
- **Cut-off frequency calculator.** When doing the first steps using the Matlab graphic user interface, we tried to implement some small but useful tasks. During the coupler design, one of the most important parameters is the cut-off frequency. A little program for making the ever-recurring cut-off frequency calculations faster was thus very practical.

This application can be used for rectangular and circular waveguides. In addition to that, the cut-off frequencies of the first TE and TM mode on a coaxial line and the measured and simulated cut-off of the beam screen were included. The cut-off frequency calculator can be found in the menu “Tools”.

### 4.3.3 Backend functions

Like in many Matlab applications, for the reflectometer a modular design is used. The main function is *reflec.m*. When started (function call without input arguments) it first initializes the graphical user interface. Upon every user interaction, for instance, when a button is pushed, it calls itself recursively with a specific argument. A switch then chooses the right action to be taken. Small tasks, like saving the project or calling the help are treated in *reflec.m* itself. For more complicated things, like reading or plotting data, small functions are called. The handing over of variables to the functions is done either by input and output arguments or by global variables. The entire reflectometer project information is stored in two global structure arrays; all the traces are contained in the trace array *t* and the environment parameters are stored in the array *e*. An obvious draw-back of this implementation is, that when working with the not compiled

functions, only one instance of the reflectometer can run at a time. It is being considered to fix this by attaching the data to the Matlab project window in the UserData property. However, for development and maintenance the global variable approach is rather practical, since all data can be directly accessed from the Matlab command line. Below follows a detailed description of the various functions.

- **Importing data.** The standard way to get measurement data from the network analyser is to read it from an .s1p file from the disk. Other file types such as the old HP 8753 citifiles (e.g. \*.D1) are supported, too. This task is performed by *import2.m*. The data and attributes from the file header are read and stored in a Matlab structure array. In general, the data is returned as an N by 2 array with the frequency axis in the first column and the complex data in the second. Data attributes comprise start and stop frequency, step width, number of points, (redundant with data) and header info provided by the measurement device. These informations can be accessed in the reflectometer application under “Edit trace”. If data from other devices needs to be treated, a simple modification of *import2.m* is sufficient.
- **Triggering measurements.** The control of the E8358A network analyser was implemented in Visual Basic (VB). In order to make a measurement from Matlab, a small VB application is called in *reflec.m*. A measurement is triggered and the data is stored in an .s1p file. This data file is then imported into Matlab using the standard function *import2.m*.
- **Zooming, mouse and keyboard shortcuts.** All the user interactions via shortcuts are treated by *drag\_plot.m*. This function is called during the initialization of the reflectometer application. Most of the reflectometer application functionality can be accessed via keyboard shortcuts. For an actual (but not necessarily all-embracing) documentation please check the help menu. A sophisticated zooming utility has been implemented, too. It includes dragging the plot and zooming with the mouse, as well as keyboard panning and zooming. The keyboard zooming can also be used directly on the number pad of the PNA E8385A. For further details the reader is referred to the help menu.
- **Smoothing.** Traces can be low-pass filtered with the function *smoothing.m*.
- **Set active traces.** After most trace manipulations the “Active trace” field in the reflectometer application is actualized. This is done by calling *set\_active\_traces.m*.
- **FFT calculation.** When new data is to be displayed in the “FFT” tab or after pressing one of the “Calc!” buttons, the FFT of the raw data has to be calculated. This is done in the function *fourier2.m*. Several processing options are possible, especially
  - Zero padding to increase the displayed resolution of the resulting trace
  - Subtraction of an electrical delay to correct the phase shift from a coaxial line between the measurement device and the device under test
  - A number of different window functions

- Dispersion correction for one fixed distance (focusing onto one instant in time  $\tau$ )
- **Dispersion compensation.** Correction of the effect of waveguide dispersion for only one point is performed in `fourier2.m`. An improved version performing dispersion correction over an arbitrary section was implemented in `foggy2.m`. After an optional zero padding of the raw data, two ways of processing are open.
  - **Calculation of the full dispersion correction matrix.** This option basically performs the focusing to one point as in `fourier2.m`. This process is repeated with the focus running from the start of the trace (zero distance) to a specified maximum distance. The resulting traces are stacked in a matrix that can be displayed in the reflectometer application under the “Waterfall” tab. However, for each trace only a very small section close to the focus is actually “in focus”. Most of the data in the matrix is therefore not really interesting, apart from allowing to check for mode mixing. In order to get the focused data, from each trace the small focused section is cut out and pieced together. This data can be plotted under the tab “Focusing”.
  - **Fast focusing algorithm.** Even though the approach above is pretty straightforward and easy to implement, for good resolution and long distances the matrices soon get impractically large. A new algorithm optimized for dispersion correction was implemented. It calculates only the focused data, and it does it fast.

The measured data in frequency domain comes in a vector  $X$ . We can calculate the discrete  $N$ -point Fourier transform (DFT) using the standard formula

$$x(n) = \sum_{k=0}^{N-1} X(k)e^{j2\pi kn/N} \quad 0 \leq n \leq N-1 \quad (4.1)$$

Introducing the Fourier transform base  $W = e^{j2\pi/N}$  we can express the DFT in shorter terms

$$x(n) = \sum_{k=0}^{N-1} X(k)W^{nk} \quad 0 \leq n \leq N-1 \quad (4.2)$$

Waveguide dispersion is proportional to the propagation distance  $z$  and to  $\sqrt{f^2 - f_c^2}$ , with the frequency  $f$  and the cut-off frequency  $f_c$ . For a given distance  $z$ , conveniently chosen to be the distance between two points of  $x(n)$  in the time domain, we can calculate the phase compensation vector  $c$ . The element  $c(k)$  contains the negative phase distortion for the frequency  $k$  at a distance  $z$  [7]. The DFT including the phase compensation term is then

$$x(n) = \sum_{k=0}^{N-1} X(k)c(k)^n W^{nk} = \sum_{k=0}^{N-1} X(k) \left( c(k)W^k \right)^n \quad (4.3)$$

$$x(n) = \sum_{k=0}^{N-1} X(k)u(k)^n \quad 0 \leq n \leq N-1 \quad (4.4)$$

with  $u(k) = W^k c(k)$ . As can be seen in equation 4.3, each element of the data vector  $X(k)$  has to be multiplied with the corresponding element of the dispersion compensation vector  $c(k)$  for each point. Therefore the standard FFT algorithm could not be modified in order to include dispersion correction. The fast focusing algorithm can be formulated as

```
* Initialize  $u$ :  $u(k) = 1$ ;       $0 \leq k \leq N - 1$ 
* for  $l = 1$  to  $N$ 
*    $x(l) = \sum_{k=1}^{N-1} X(k)u(k)$      $0 \leq k \leq N - 1$ 
*    $u(k) = u(k)c(k)W^k$            $0 \leq k \leq N - 1$ 
* end
```

This algorithm has the same complexity as a conventional DFT, that is  $N^2$ . It is considerably faster compared to the approach where the entire focusing matrix is calculated by FFT. The latter algorithm has a complexity  $N^2 \log_2(N)$  for power of 2 trace lengths. Moreover, the fast focusing algorithm avoids huge and difficult to handle matrices.

For both options in `foggy.m` various window functions are possible and an electrical delay can be accounted for.

- **Plotting.** Two functions are responsible for plotting tasks. Ordinary 2D plots for the “Raw data”, “FFT” and “Focusing” tabs are plotted by `plotdata.m`. Various plot formats are available, including logarithmic and linear magnitude, real part and Smith Chart plot. Each trace is plotted in a different color and style, for a maximum of 6 traces, then the styles cycle. Optionally Trace symbols and a grid can be displayed (under “Parameters” button) in the reflectometer application. The waterfall plot is done by `plotmat.m`.

## 4.4 Performance

The main performance parameters of the Assembly Version were calculated and determined experimentally.

### 4.4.1 Resolution

The resolution of the Assembly Version reflectometer will be in the range of a few centimeters. Depending on the bandwidth and the window function used, the 6 dB pulse width varies in the range between 6 and 10 cm as listed in Table 3.1. For the ultimate version with the  $TM_{01}$  mode between 6 and 10.5 GHz a resolution below 5 cm could be possible, provided that spurious mode free excitation can be achieved.

Another important point is how close to a given large inhomogeneity the detection range goes. The mode launchers have a reflection coefficient of about  $-20$  dB, the interconnects are expected to give larger reflections of about  $-15$  dB. The 20 dB bandwidth for Kaiser windows can be found in Table 3.2. For a 3 GHz bandwidth  $TM_{01}$  mode measurement using  $\beta = 6$  we get  $x = 6.5 \text{ cm} \cdot 1.68/2 = 5.5 \text{ cm}$ . That means that already 5.5 cm away from the mode launcher we will be able to see a small obstacle’s peak rising out of the shoulder of the mode launcher’s reflection.

As the last particular case we will consider here the dipole’s protective end caps. They

can be considered as massive short circuits. Under the same conditions as above we get for half of the 40 dB impulse width  $x = 6.5 \text{ cm} \cdot 2.07/2 = 6.7 \text{ cm}$ . Including some safety margin we can be sure that full sensitivity is achieved no farther than 10 cm from the beam screen extremity.

#### 4.4.2 Range

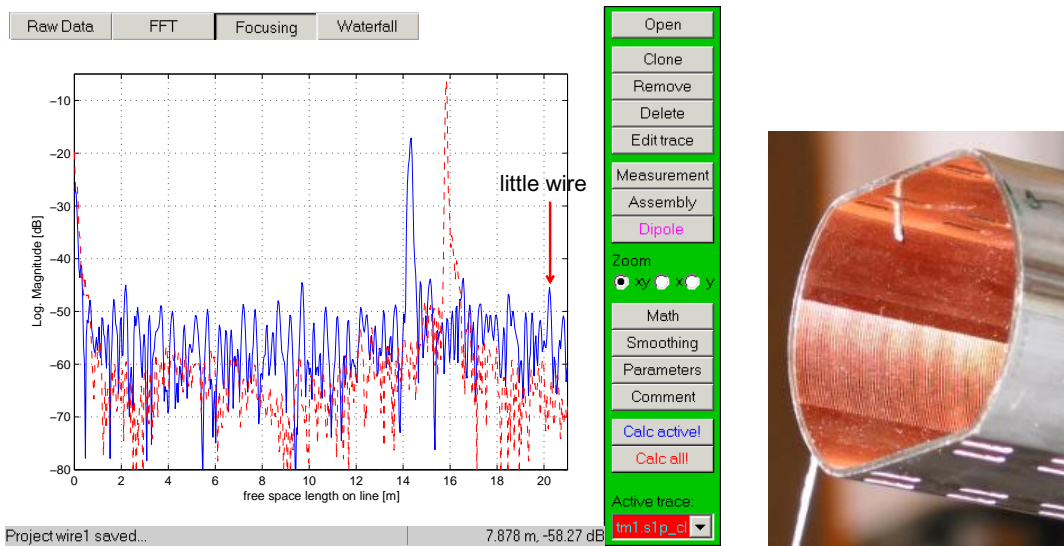
Preparatory measurements on the 50 m test track have shown that a very small obstacle can be seen over at least 40 m. The object inserted was a 1 mm diameter metallic wire, reaching 5 mm into the beam screen through one of the pumping holes (Fig. 4.15(a), solid blue trace). Accounting for waveguide attenuation, a net reflection peak of about  $-43 \text{ dB}$  was found for the  $\text{TM}_{01}$  mode. The noise level was at about  $-50 \text{ dB}$ , the peak at 14.5 m is an interconnect. On this test track only a simple beam screen tube was used, without cold bore or pumping slot shields. A waveguide calibration was performed but similar high levels of noise were found for cross-checks by uncalibrated measurement.

The noise level in the second measurement in Fig. 4.15(a) (dashed red trace) is about 10 dB lower. This measurement was performed on a completely assembled dipole. Obviously, the cold bore and the pumping slot shields act in a very favorable way. They reduce the background signal level by providing a kind of RF shielding of the pumping slots. For practical reasons no small objects were introduced in the fully assembled dipoles, but the lower noise level should make a detection of such obstacles easier than on the test track. The remaining noise in the dipole measurement is due to a non-perfect coaxial calibration to the connector of the mode launcher. An uncalibrated measurement yielded a noise floor still 8 dB lower.

As minimum detectable obstacle we define an object giving a reflection of more than  $-40 \text{ dB}$ . A metallic M4 nut for instance should already fall into this category. Now we can calculate the theoretical range of the Assembly Version reflectometer. The line attenuation of the  $\text{TE}_{c11}$  and  $\text{TM}_{01}$  mode at room temperature is given in Table 2.2. Using the available E8358A network analyser with 100 Hz IF bandwidth, we can obtain an instrument dynamic range of about 115 dB. The measured reflection coefficient of the mode launchers was close to  $-20 \text{ dB}$ . Plugging in the numbers in formula 3.5, we get a range of 800 m for the  $\text{TM}_{01}$  mode and 450 m for the  $\text{TE}_{c11}$  mode, respectively.

#### 4.4.3 Sensitivity

It has been demonstrated that the reflectometer can be used to detect small obstacles ( $-40 \text{ dB}$  reflection) at distances of up to 45 m. It can be expected that the background signal level increases with distance. Interpolating from tests using a coaxial line, it is assumed that the noise level does not increase above  $-40 \text{ dB}$  for the first 10 interconnects or so, corresponding to a distance of about 140 m. However, this assumption has to be substantiated by tests on a long section of the beam screen, e.g. one LHC cell. In the following, we assume that the minimum relevant obstacle gives a reflection of  $-40 \text{ dB}$ . The signature of typical obstacles will be further discussed in the next section.



(a) The solid blue trace was taken on the 50 m test track with an interconnect at position 14.5 m and a tiny obstacle at position  $\approx 20$  m. Since the beam screen was not installed in the cold bore, the background signal from the slots has the same level as the little obstacle. The red dashed trace represents a single dipole with the end reflection at position 16 m.

(b) The little wire that was inserted through the pumping slots into the beam screen.

Figure 4.15: Preparatory assembly measurements with the  $TM_{01}$  mode.

#### 4.4.4 Test obstacles

In preparatory tests, obstacles of various kinds have been inserted in a waveguide to check the scope of the detectable objects. As could be expected, metallic and plastic screws and nuts, handkerchiefs, cigarettes and similar objects can be seen as reflections well above  $-40$  dB. On the 50 m test track, a steel wire with 1 mm diameter was inserted at different locations into the beam screen. In order to get a better feeling of the properties of different kinds of obstacles, a more comprehensive study was done, including objects of different conductivity, electric permittivity and magnetic permeability. It turned out that the detecting sensibility depends much on the waveguide mode, the type of obstacle and the location in the beam screen. The following obstacles were studied in measurements and/or simulations:

- M3 hexagonal steel nut, 2.3 mm height, width (between parallel sides) 5.45 mm, inner diameter 2.3 mm
- M4 hexagonal steel nut, 4.7 mm height, width 6.35 mm, inner diameter 3.2 mm
- M3 hexagonal dielectric nut made from polyamide, relative permittivity estimated as  $\epsilon_r = 2.5$ , 2.6 mm height, width 5.55 mm, inner diameter 2.5 mm
- M5 hexagonal dielectric nut made from polyamide, relative permittivity estimated as  $\epsilon_r = 2.5$ , 4.25 mm height, width 8.0 mm, inner diameter 4.1 mm
- dry cigarette stub, about 30 mm long
- piece of folded cleaning cloth, slightly dirty, 35x35x5 mm<sup>3</sup>

- A6 size paper sheet, about  $14.8 \times 10.4 \text{ mm}^2$ , folded 6 times
- copper tape, 0.1 mm thickness,  $40 \times 12.5 \text{ mm}^2$
- hollow ferrite cylinder, permeability unknown, 24 mm long, outer radius 8 mm, inner radius 4.5 mm
- local deformation using a clamp with jaws  $15 \times 15 \text{ mm}^2$ . The clamp was installed on the flat sides of the beam screen and contracted by up to 2.8 mm. The resulting cross-section deformation is similar to the one created by the quench-induced currents. However, the maximum deformation of 1.4 mm for one side is about 65 % higher than the one expected during a dipole quench [22]. It should be noted that after taking the measurements and removing the clamp, a slight deformation of about 0.2 and 0.3 mm depth and 30 mm width remained on the flat sides of the beam screen.

In regions of LHC where the beam screen is installed horizontally, obstacles are likely to lie on the flat side of the beam screen. However, also obstacles sticking to the wall should not be excluded beforehand. In order to investigate the influence of the obstacles' location, they were placed in different positions in the beam screen cross-section, for most objects

- in the center of the flat beam screen side
- 10 mm aside the center of the flat beam screen side (between the two rows of pumping slots)
- in the center of the curved side, on top of the welding strip

A CST Microwave Studio simulation was run for the nuts, since their geometry and material properties are relatively easy to model. It was judged not worth the effort to simulate for example the slightly dirty cleaning cloth. The results are summarized in Table 4.1. The geometries used in the simulation are shown in Fig. 4.16. After encountering some substantial discrepancies between measurement and simulation, the model had to be somewhat adapted. Changing the material to steel instead of a perfect conductor did not yield a significant effect. The same is true for modelling the hole in the center of the nuts, at least for the metallic ones. For the dielectric objects, omitting the hole translates into an increase in effective permittivity. But still, the simulated reflections for the metallic obstacles were way too high. It was found that the resistance that had been neglected so far was responsible for that. Since it is hard to get a good quantitative grip on the surface resistance, the metallic objects were just separated from the beam screen by a 0.2 mm isolating layer. Keeping in mind that the obstacles didn't have a clean surface and that there was no contact force applied, the assumption of very low conductivity between the obstacle and the beam screen appears reasonable. Simulations using this model showed much better agreement with measured data.

For the  $\text{TE}_{c11}$  mode, the frequency range used was from 4 to 7 GHz and for the  $\text{TM}_{01}$  mode from 6 to 9 GHz for both simulation and measurements. The values quoted below are the maximum magnitudes of the reflection peaks in time domain. Pulse widening due to dispersion was neglected in the simulation, since the total length of

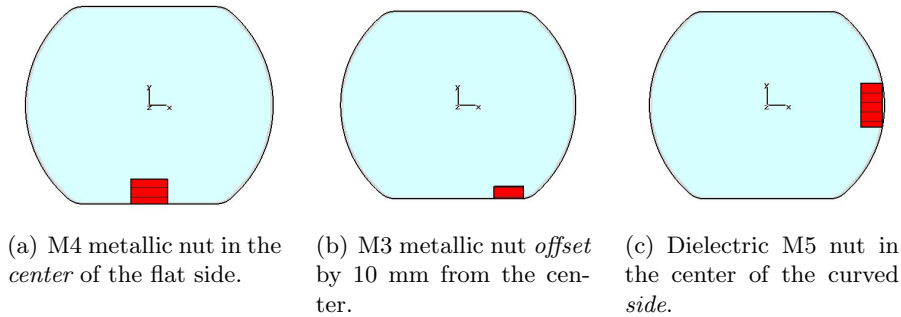


Figure 4.16: Position of obstacles in beam screen as used in simulations.

Obstacle	Location	Measured $S_{11}$ [dB]		Simulated $S_{11}$ [dB]	
		$TE_{c11}$	$TM_{01}$	$TE_{c11}$	$TM_{01}$
Steel M4 nut	center	-20	-21	-21	-20
	offset	-26	-26	-28	-24
	side	-41	-25	-42	-26
Steel M3 nut	center	-34	-34	-33	-31
	offset	-44	-37	-41	-36
	side	-45	-39	-50	-38
Dielectric M3 nut	center	-47	-49	-45	-47
	offset	-53	-51	-49	-51
	side	$\approx$ -60	-51	-64	-52
Dielectric M5 nut	center	-35	-39	-39	-38
	offset	-40	-43	-40	-43
	side	$\approx$ -60	-44	-59	-43

Table 4.1: Measured and simulated time domain  $S_{11}$  of metallic and dielectric nuts. The three possible locations are “center” for the center of the flat beam screen side, “offset” 10 mm aside and “side” for the center of the curved beam screen side. See Figure 4.16 for a sketch of these objects. In the measurements, the objects were introduced in an about 1 m long beam screen sample.

the model geometry is small (50 mm). In order to decrease the number of mesh cells while maintaining high accuracy, sub-gridding was used for the metallic objects and volume refinement for the dielectric objects. When subgrids were used, the simulation converged already at the first or second mesh refinement but each run was relatively slow. For volume refinement, in general up to 5 mesh refinements were needed to have the results converge, but the single runs terminated much faster.

In the measurements a coaxial calibration to the end of the coaxial line was used, however the coupler insertion losses and line attenuation were not taken into account. The systematic error introduced this way should not exceed 0.3 dB, and is mainly due to the coupler.

Comparing the measurement results to the numerical simulation for the nuts, generally an excellent agreement was found. For the  $TE_{c11}$  mode, the simulated values differ from the measured values by  $-0.5 \pm 2.9$  dB, for the  $TM_{01}$  mode the discrepancy is  $0.8 \pm 1.2$  dB. The measurement results for the remaining objects are presented in Table 4.2.

Obstacle	Location	$S_{11}$ [dB]	
		TE <sub>c11</sub>	TM <sub>01</sub>
cigarette stub	flat side, normal to beam screen axis	-37	-45
	10 mm aside center of flat side, parallel to beam screen axis	-49	-51
cleaning cloth	lying on flat side	-40	-51
folded paper	lying on flat side	-31	-45
copper tape	one end sticking to flat side, other end 2 mm off surface	-22	-22
	sticking to flat side over half its length, other end 1 mm off	-42	-38
	sticking to flat side over entire length	-60	$\approx$ -54
ferrite cylinder	lying in center of flat side, parallel to beam	-34	-22
	lying in center of curved side, parallel to beam	-30	-22
deformation	total vertical contraction 1.4 mm	-48	-52
	total vertical contraction 2.8 mm	-41	-45
	remaining vertical contraction $\approx$ 0.5 mm	-51	$\approx$ -60

Table 4.2: Measured time domain  $S_{11}$  of various potential obstacles. The objects were introduced in an about 1 m long beam screen sample.

The data of tables 4.1 and 4.2 can be explained in a very straightforward way considering the properties of the waveguide modes. The mode patterns of the TE<sub>c11</sub> and TM<sub>01</sub> modes (Fig. 2.6) offer some hints. In the following, the interaction of the waveguide modes with different kinds of materials will be examined.

- $\epsilon_r \neq 1$ . Dielectric objects mainly interact via the electric field. Thus, in regions of high electric field, a relatively strong response can be expected. For the TE<sub>c11</sub> mode, this is the case in particular for the region around the center of the flat beam screen side. Conversely, close to the curved side the E field is small and dielectric obstacles are virtually invisible for the TE<sub>c11</sub> mode. The TM<sub>01</sub> mode on the other hand has a strong E field on the axis of the beam screen with relatively low components close to the walls. Around the circumference of the beam screen, the E field is somewhat concentrated along the flat side, but the variation is not too big. Therefore, the TM<sub>01</sub> mode is sensitive to dielectric objects all over the beam screen.
- $\mu_r \neq 1$ . Ferrites and similar objects mainly influence the magnetic field. Using the same arguments as above with the electric field replaced by the magnetic field, we find that the TE<sub>c11</sub> mode should show a rather strong response all over the beam screen, especially in the region of the curved side. For the TM<sub>01</sub> mode the magnetic field is slightly stronger along the flat sides, therefore its obstacles in this region should give higher reflections.
- $\sigma > 0$ . Conducting objects interact with both the E and H field. However, measurement and simulation results showed that the E field plays a more important role. A behaviour similar to dielectric objects was found, even though the reflections for a given object size were far bigger.
- Surface defects. Changes in local surface resistance as well parts of the copper coating coming off directly affect the wall currents, which are coupled to both the magnetic and the electric field. Due to the lack of data we can only state that

Obstacle type		$\epsilon_r \neq 1$	$\mu_r \neq 1$	$\sigma > 0$	surface defect
Typical object		diel. M5 nut	ferrite cylinder	steel M4 nut	20 mm tape 1 mm off
TE <sub>c11</sub>	center	medium	medium	very high	
	offset	medium		high	medium
	side	very low	medium	medium	
TM <sub>01</sub>	center	medium	high	very high	
	offset	medium		high	medium
	side	medium	high	high	

Table 4.3: Summary of the sensitivity of the TE<sub>c11</sub> and TM<sub>01</sub> modes to different kinds of obstacles. The three possible locations are “center” for the center of the flat beam screen side, “offset” 10 mm aside and “side” for the center of the curved beam screen side. The rating “very high” means  $S_{11} \geq -25$  dB, “high”  $-25 > S_{11} \geq -35$  dB, “medium”  $-35 > S_{11} \geq -45$  dB, “low”  $-45 > S_{11} \geq -55$  dB, “very low”  $-55 \text{ dB} > S_{11}$ . The rating for the ferrite cylinder was decreased by one level because it is significantly bigger than the other obstacles.

both TE<sub>c11</sub> and TM<sub>01</sub> mode seem to be almost equally sensitive to this kind of perturbation.

- Deformations. For the TE<sub>c11</sub> mode, small geometry changes act like capacitive and/or inductive impedances. The typical quench deformation (flat beam screen sides bent inwards, curved sides pulled outwards) constricts the E field where it is maximum. In addition to that, in the deformed cross-section the TE<sub>c11</sub> cut-off frequency decreases owing to the enlarged width of the beam screen. A relatively big reflection can therefore be expected. The TM<sub>01</sub> mode on the other hand does not respond too much to deformations, provided that the circumference of the beam screen stays constant. This is due to the fact that the magnetic field lines still run in parallel to the deformed racetrack shape and the change in cut-off frequency is small.

The sensitivity of the TE<sub>c11</sub> and TM<sub>01</sub> modes are put together in Table 4.3 for typical obstacles of each material. It is meant to be a concise summary, not an accurate comparison, which would be difficult with objects of so different sizes and shapes. The sensitivity to conducting obstacles is high, while dielectric objects, ferrites, surface defects and deformations give medium reflections.

#### 4.4.5 Multiple reflections

When looking over longer distances, a periodic reflection pattern stemming from the interconnects will appear. The 53.5 m long LHC half-cell (Fig. 2.3), composed of three main bending magnets and a lattice quadrupole, houses four interconnects. In section 2.3 the reflection coefficient of the interconnects was estimated. For the TM<sub>01</sub> mode,  $S_{11} \approx -15$  dB and for the TE<sub>c11</sub> mode  $S_{11} \approx -10$  dB was found, averaged over the frequency range of operation. An important question is now, what will happen with the microwave power that gets reflected back on the line. In a zeroth-order approximation multiple reflections are completely neglected. Depending on the application, this is possible if the reflections are small. However, since in our case the interconnects reflections

are not very small and we are interested in finding little inhomogeneities, the multiple reflections have to be taken into account.

For the  $TM_{01}$  mode, a signal being reflected once by an interconnect has a relative magnitude of about  $-15$  dB. The first multiple reflection component is the signal that was reflected three times with a magnitude of about  $-45$  dB. This gets close to the target value for an obstacle of  $-40$  dB. The  $TE_{c11}$  mode interconnect reflection being still higher, multiple reflections in the range of  $-30$  dB can be expected. However, all is not lost, since the positions of the interconnects are known. Therefore, the locations of multiple reflection peaks can be anticipated.

Fig. 4.17 shows the simulated multiple reflection peaks for the  $TM_{01}$  mode. In the left plot the simplified case of equidistant interconnects is shown. However, because the LHC short straight sections are shorter than the dipoles, the interconnects are not equidistantly spaced. The latter case is shown in the right plot. In these simulations only the signals reflected once and three times are included, representing a first-order approximation. Higher order multiple reflections are negligible, for they would be another 30 dB smaller. When several signals superimpose, the signal power was added as a pessimistic estimation.

Comparing the two plots in Fig. 4.17, several points can be noted.

- The first interconnect's response is unperturbed.
- For subsequent multiple reflections the signal level grows.
- For equidistant reflectors, all multiple reflections fall on the locations of direct reflections. No additional noise is created between the reflectors, but the response of each single reflector is perturbed. This can be a problem when the signal of a single interconnect needs to be analyzed in detail.
- For the real LHC lattice, the multiple reflections are “scrambled” spatially. The level of the multiple reflection signal grows slower but the noise floor between the interconnects rises. At a distance of about 150 m, the multiple reflections reach the  $-40$  dB obstacle threshold. On the other hand, the perturbations of the interconnects' reflections are rather limited.

At this point the fact has to be stressed that these simulations depend a lot on one parameter, the interconnects'  $S_{11}$ . There is still some uncertainty on this parameter. A supposedly small increase by 5 dB can significantly increase the level of the reflections, as can be seen in the  $TE_{c11}$  case in Fig. 4.18. Already at 100 m distance multiple reflections as high as  $-27$  dB can be expected. Especially for the  $TE_{c11}$  mode, a “dynamic deconvolution” procedure would be interesting for numerical removal of multiple reflections.

## 4.5 Reflectometry on the cryogenic ring line

The superconducting LHC magnets will be cooled with superfluid helium to their operating temperature of 1.9 K. An intricate cryogenic system was devised for refrigeration, distribution and evacuation of the helium [2]. Produced in eight refrigeration plants situated at five points (Fig. 4.19(a)), the liquid helium is pumped into the tunnel for transport on the cryogenic ring line (QRL). The QRL runs alongside the machine on

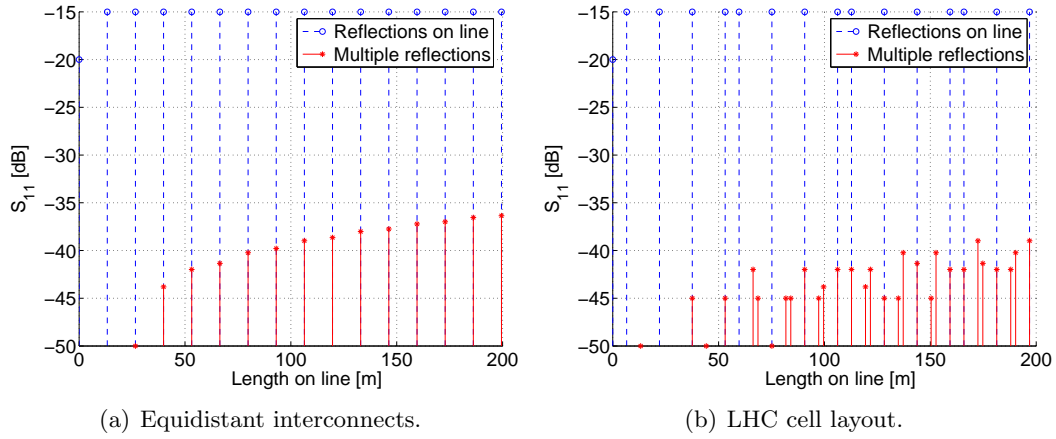


Figure 4.17:  $TM_{01}$  mode multiple reflections by the interconnects for different layouts. The reflection coefficient of the mode launcher and interconnects was estimated as  $-20$  and  $-15$  dB, respectively.

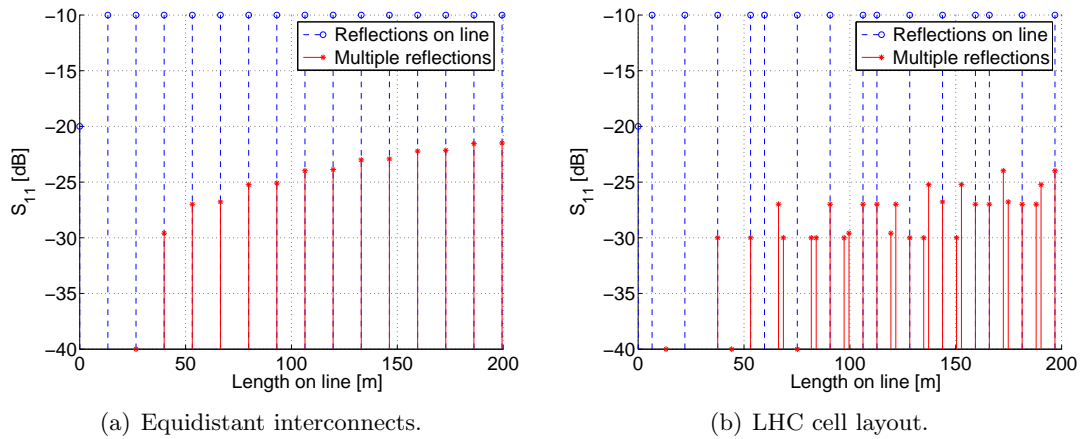


Figure 4.18:  $TE_{c11}$  mode multiple reflections by the interconnects for different layouts. The reflection coefficient of the mode launcher and interconnects was estimated as  $-20$  and  $-10$  dB, respectively.

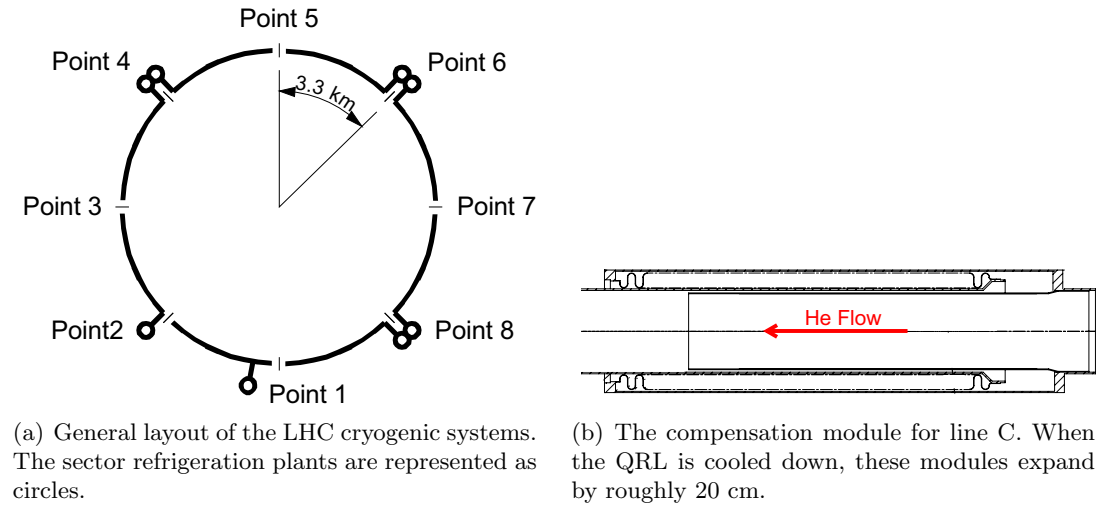


Figure 4.19:

the outer side of the tunnel, see Fig. 4.20. Helium in different states is transported in stainless steel tubes of different diameter. In the case of magnet quench, a large volume of helium has to be evacuated in very short time. Pressures of about 2 MPa are expected for the lines E and F [37]. After the installation of the lines, pressurization tests with higher pressures are performed to check the stability of the lines. Since these distribution lines are difficult to access once the magnets are installed, it is very important to make sure that the installation is impeccable. However, the inside of the pipes is even more difficult to access through the outer cryostat and the steel tubes. In addition to that the lines run over big lengths of up to 3.3 km.

In early 2005, the idea was born within the collaboration between the AT-VAC group and the University of Krakow to employ the waveguide mode reflectometry for quality insurance on the QRL. At the time of writing (June 2005), first tests have been performed, which are outlined below. Concerning the measurement set-up and signal processing, the existing configuration for the Reflectometer Assembly Version could be used with minor adaptations.

#### 4.5.1 RF properties of the QRL

The QRL is composed of stainless steel lines having diameters between 80 and 267 mm. The individual lines are connected to the machine cryostat once for each lattice cell, that is every 106.9 m via a jumper connection. The tappings have diameters of one third of the pipe diameter or smaller. Every about 12 m the pipe sections are connected by a weld. In general every fifth section, i.e. about every 60 m a compensation module is installed which can make up for the thermal contraction during cool-down. As an example, the D line compensation module is shown in Fig. 4.19(b). This discontinuity is rather smooth so as not to impede too much the helium flow. However, from the RF point of view, the concentric pipes form a TEM line, which can be expected to strongly influence the  $TM_{01}$  mode due to the similar mode pattern. In addition to the  $TM_{01}$  mode, use of the  $TE_{11}$  mode was tested.

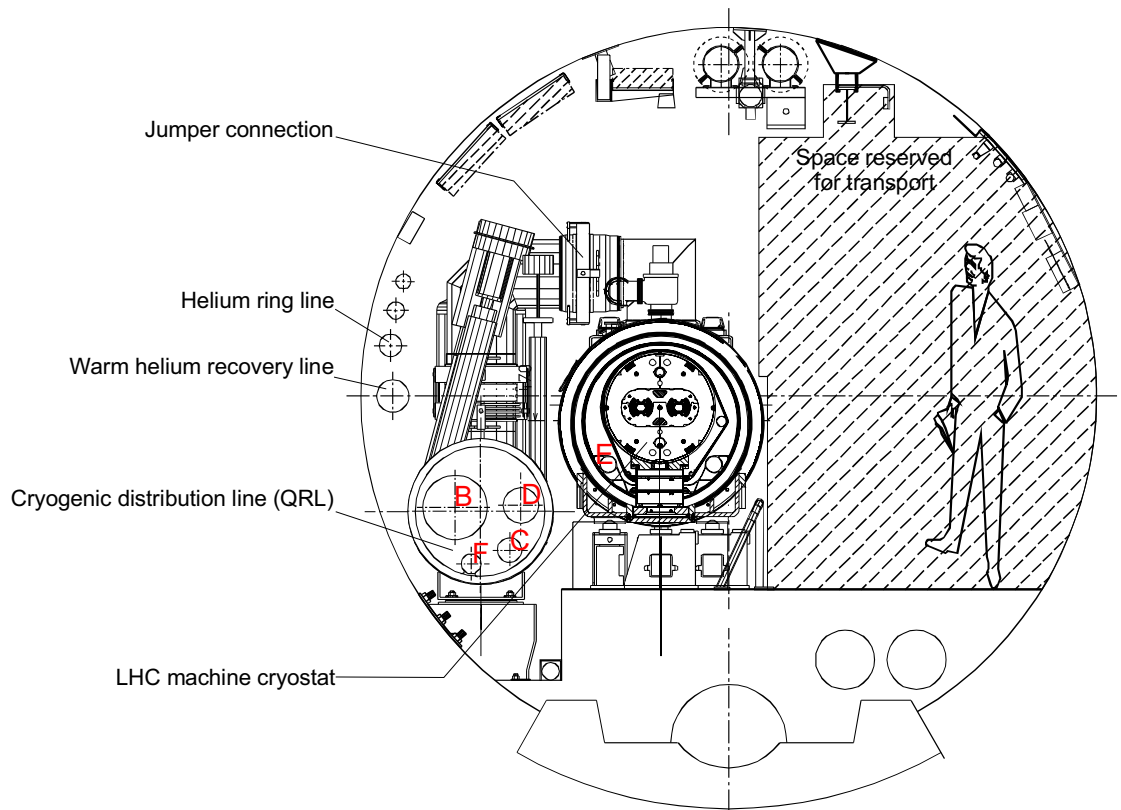


Figure 4.20: Cross-section of LHC tunnel with the QRL. The red capitals indicate the labels of the individual lines.

Line	$\varnothing$ [mm]	$f_c$ [GHz]		Peak width [cm]	
		TE <sub>11</sub>	TM <sub>01</sub>	TE <sub>11</sub>	TM <sub>01</sub>
B	267	0.658	0.860	190	61
C	100	1.757	2.295	71	27
D	150	1.171	1.530	106	34
F	80	2.196	2.869	55	18

Table 4.4: Cut-off frequencies and 6 dB peak widths for reflectometry measurements on the QRL lines.

### Frequency range

Not much time and resources were available for the design and manufacturing of flanges and improvised antennas. In addition to that, there are many inhomogeneities in the QRL lines that can excite higher order modes. For these reasons the frequency range of operation had to be somewhat limited. For the fundamental TE<sub>11</sub> mode pure mono-mode operation was chosen since the antennas also excite the TM<sub>01</sub> mode. The TM<sub>01</sub> mode is ideally limited by the cut-off of the second TM mode with rotational symmetry, the TM<sub>02</sub>. This leaves a pretty wide operational frequency range. However, the impact of mode conversion gets bigger at higher frequencies when more and more modes can propagate. Keeping the above constraints in mind we started with a frequency range between  $1.1 \cdot f_c$  and  $0.95 \cdot f_{cHOM}$ , with the mode's cut-off  $f_c$  and the higher order mode cut-off  $f_{cHOM}$ . This leads to a range between  $1.1f_c$  and  $1.241f_c$  for the TE<sub>11</sub> mode and  $1.1f_c$  and  $2.180f_c$  for the TM<sub>01</sub> mode. For reasons of mode conversion and antenna response the latter frequency range was later reduced to  $1.1f_c$  to  $1.5f_c$ .

The resolution is inversely proportional to the bandwidth  $B$  used, as given in Equation 3.4. With Kaiser windows having  $\beta = 9$ , a high  $\beta$  value necessary due to the relatively long range, the  $k$  parameter becomes about 2.2. Table 4.4 lists cut-off frequencies and peak widths on the individual lines for the frequency ranges given above.

### Attenuation

The waveguide attenuation was calculated using the formulas given in [9]. For circular pipe with diameter  $D$ , cut-off frequency  $f_c$  and conductivity  $\sigma$  the TM<sub>01</sub> mode attenuation is given by

$$\alpha_{TM} = 9.04 \cdot 10^{-4} \frac{1}{\sigma [\text{S/cm}] D [\text{cm}]} \frac{f [\text{Hz}]}{\sqrt{1 - \left(\frac{f_c}{f}\right)^2}} \quad [\text{dB/m}] \quad (4.5)$$

and the TE<sub>c11</sub> mode attenuation by

$$\alpha_{TE} = 9.04 \cdot 10^{-4} \frac{1}{\sigma [\text{S/cm}] D [\text{cm}]} \frac{0.42 + \left(\frac{f_c}{f}\right)^2}{\sqrt{1 - \left(\frac{f_c}{f}\right)^2}} \quad [\text{dB/m}]. \quad (4.6)$$

For the conductivity of stainless steel  $\sigma = 1.43 \cdot 10^4$  S/m was assumed. The attenuation averaged over the operational frequency range is given in Table 4.5. These values are

Line	Attenuation [dB/m]	
	TE <sub>11</sub>	TM <sub>01</sub>
B	0.018	0.016
C	0.078	0.068
D	0.043	0.037
F	0.110	0.095

Table 4.5: Waveguide mode attenuation on the QRL lines. For the TE<sub>11</sub> the frequency range  $1.1f_c$  to  $1.241f_c$  was used, for the TM<sub>01</sub> mode  $1.1f_c$  to  $1.5f_c$ .

far above the minimum values for the respective mode, in particular for the TE<sub>11</sub> mode. This is due to the fact that the mono-mode region on the circular waveguide is particularly narrow, so that we cannot work in the attenuation minimum. However, the attenuation did not turn out to be a major limiting factor.

### Flanges, antennas and discontinuities in the QRL

Simple antennas were designed and optimized for both modes. For the TE<sub>11</sub> mode, a hook and for the TM<sub>01</sub> mode a central pin was used. Both were made from wire and soldered onto an N type connector positioned in the center of the flange. Changing modes was possible by replacing the N type connectors, while the flanges did not need to be removed from the pipes.

Several simulations were run on the known discontinuities in the pipes. The tapplings were found not to disturb too much the waveguide modes. Only the biggest tapplings, which leave line D and have 50 mm diameter (a third of the line's diameter) make significant reflections. However, since they branch only every about 100 m, this can be lived with.

Compensation modules are spaced by about 60 m. Due to the big dimension compared to the wavelength, an entire module including the coaxial pipes and the bellow is not very easy to model. In preliminary simulations a distinct resonant behaviour was found for the TM<sub>01</sub> mode. This can be easily understood by noting that the coaxial pipe section inside the compensation module (Fig. 4.19(b)) acts like a TEM transmission line. A TM<sub>01</sub> wave incident from the left side will excite this TEM wave as well as a TM<sub>01</sub> wave running in the inner pipe. The TEM wave will then run back and forth inside the module and slowly couple back to the TM<sub>01</sub> mode, producing a long ringing. The TE<sub>11</sub> mode should not be very sensitive to this type of discontinuity.

### 4.5.2 Measurements

The actual measurements were performed on a 400 m length of connected QRL that was scheduled for destruction due to vacuum leaks. It was about 2000 m away from IP8 in the direction of IP7. A schematic view of the first pipe sections is shown in Fig. 4.21. A typical result taken with the TE<sub>11</sub> mode is depicted in Fig. 4.22(a). In agreement with numerical simulations, both TE and TM antennas turned out to be reasonably well matched, having an S<sub>11</sub> of about  $-10$  dB averaged over the respective frequency range. In order to make the curves easier to interpret, the line attenuation was removed numerically by adding an exponentially increasing gain. A value 20 % higher than the calculated attenuation was found to fit well in most cases. This attenuation

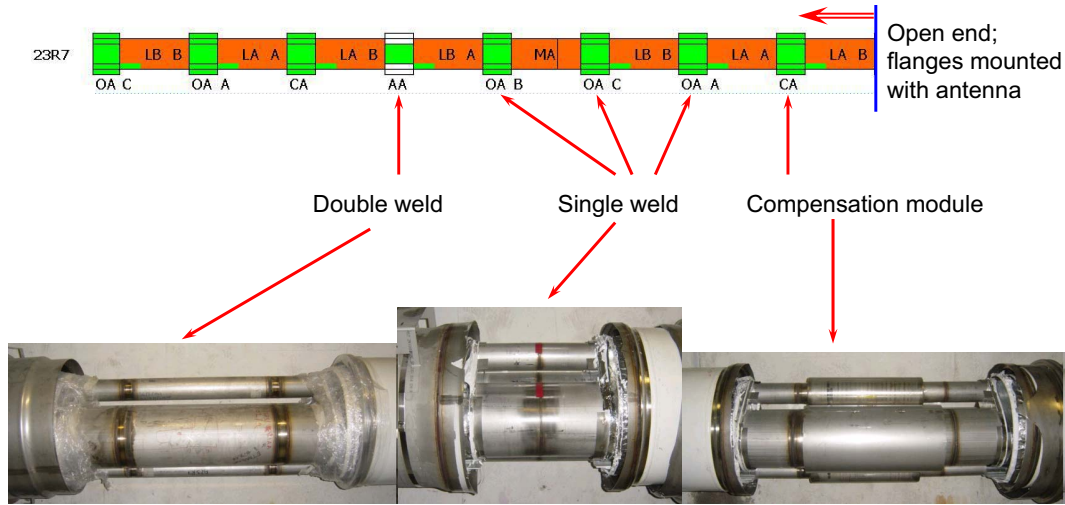


Figure 4.21: Schematic layout of the QRL section that was used for the first tests.

compensation was used for all the following plots.

The first peak at 12 m distance comes from a compensation module. The following smaller peaks are due to single welds, while the rather big peak at 54 m stems from a double weld. After initial doubts on the origin of these strong peaks it was found that 5 mm thick bucking rings were used for these double welds.

Fig. 4.22(b) shows a longer trace taken on the same line with TE and TM curves overlaid. The compensation module shows up with a long ringing in the  $TM_{01}$  mode data. The 5-section pattern compensation module – three single welds – double weld appears three times in this plot.

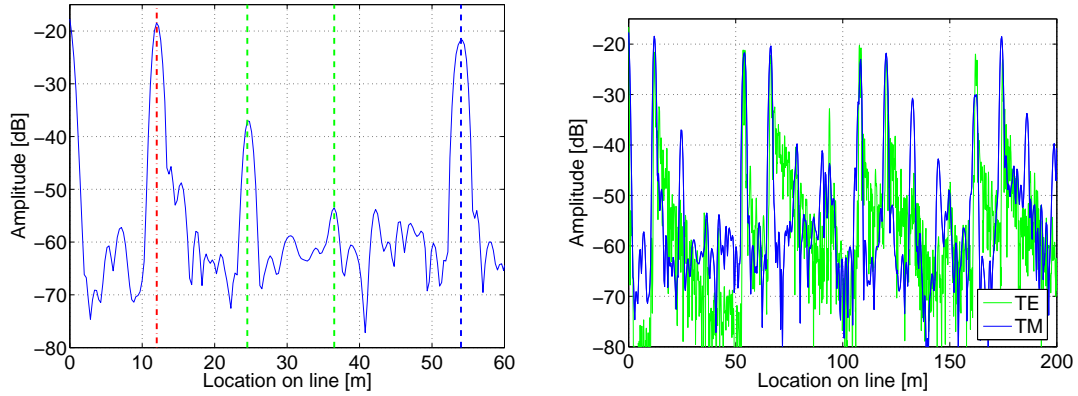
For the determination of the spatial range, the  $TE_{11}$  mode on line F is the crucial factor. From calculations using Equation 3.5 with a network analyser dynamic range of 115 dB, an antenna reflection of  $-10$  dB, a minimum obstacle of  $-40$  dB and a line attenuation 20 % above the calculated value to account for surface roughness etc the spatial range  $R$  is found as

$$R = \frac{115 \text{ dB} - (-10 \text{ dB}) + (-40 \text{ dB})}{2 \cdot 0.11 \cdot 1.2 \text{ dB/m}} = 320 \text{ m.} \quad (4.7)$$

This compares very well to the measurement depicted in Fig. 4.23(a). The estimated spatial range is marked with a dashed green line. However, the noise level, sketched as a dashed black line also increases with increasing range.

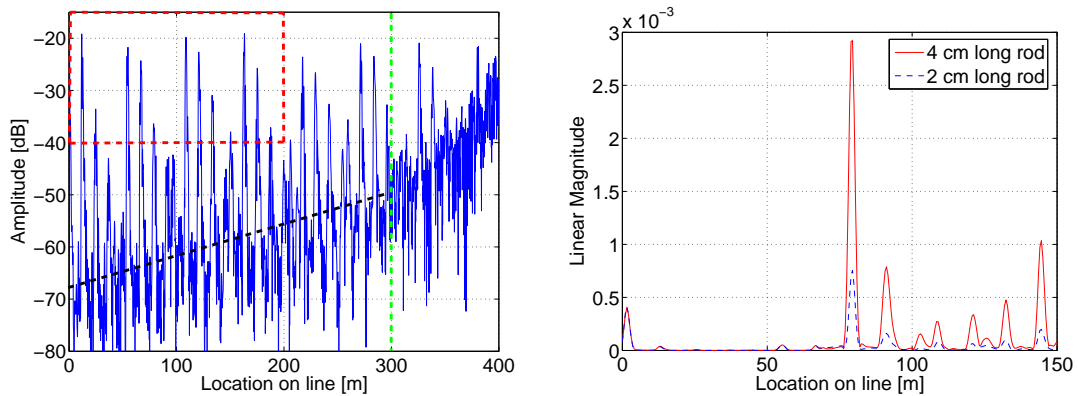
The initial measurements were *absolute measurements*, i.e. performed without special prior knowledge. However, the location of welds, compensation modules etc is known beforehand. In Fig. 4.22(a) these inhomogeneities were indicated in order to facilitate the interpretation of the results.

Once the response of the pipe has been measured, small changes can be detected with high sensitivity in *relative measurements*. An example for this method is shown in Fig. 4.23(b). At a distance of 75 m a 5 mm diameter threaded steel rod was inserted in pipe B ( $\varnothing$  267 mm). Significant signals were found for penetration depths of 40 mm and even 20 mm. Later peaks are due to reflections between the obstacle and close-by inhomogeneities.



(a) First measurement data with the TE mode. The positions of the compensation module, single welds and double welds are indicated by the red chain-dotted line, the green dashed lines and the blue dashed line, respectively. (b) Comparison of data with the TE and TM mode. Compensation modules have a characteristic signature in the TM trace due to their “ringing”.

Figure 4.22: Results from measurements on line D ( $\varnothing$  150 mm).



(a) Estimation of the spatial range of the TE mode on line F ( $\varnothing$  80 mm), which has the highest attenuation of all modes used. (b) Detection of a little obstacle on line B ( $\varnothing$  267 mm). A 5 mm threaded rod was inserted via a hole drilled in the steel tube about 75 m from the end of the pipe.

Figure 4.23:

Obstacle material	Line B $\varnothing$ 267 mm	Line C $\varnothing$ 100 mm	Line D $\varnothing$ 150 mm	Line F $\varnothing$ 80 mm
Metal	6 cm <sup>3</sup>	1 cm <sup>3</sup>	2 cm <sup>3</sup>	0.6 cm <sup>3</sup>
Dielectric ( $\epsilon_r \approx 2$ )	30 cm <sup>3</sup>	5 cm <sup>3</sup>	10 cm <sup>3</sup>	3 cm <sup>3</sup>

Table 4.6: Volume of a “typical” obstacle giving a  $-40$  dB reflection. For the obstacle geometry a cuboid with side ratio 1:1:3 lying in the pipe was assumed.

In order to get a feeling for the obstacle responses that can be expected, a number of obstacles were introduced into line D. These objects include metal cylinders and various dielectric items. Using a rough scaling, the size of a “typical” obstacle giving a  $-40$  dB reflection could be found, see Table 4.6. The size of the typical obstacle scales with the pipe diameter. Metallic objects give in general larger responses than dielectric ones. Comparing with the data found on the lines, a typical obstacle would show up inside the red rectangle in Fig. 4.23(a) among the peaks from welds, compensation modules and other known inhomogeneities.

### 4.5.3 Preliminary conclusion and possible application

The inspection of the QRL using microwave reflectometry in sections of 200 m appears feasible. When 400 m sections of QRL are subjected to pressure and helium leak tests, measurements could be done from both sides, thus covering the entire length. Carrying out measurements before and after pressurization would not only allow to check whether there are obstacles present but also to tell whether non-reversible deformations occurred. It can be imagined to perform measurements *during* the pressurization test to observe the on-set of potential mechanical instabilities, as well.

A typical measurement, including mounting the flanges and antennas, should not take more than a couple of minutes. The main effort will probably consist in the transport of the equipment. Measurements could be performed by the CERN quality assurance teams at the time of the pressurization and leak tests, causing not much additional work.

## 4.6 Summary

During the assembly of LHC, there is a non-vanishing probability of obstacle formation in the beam screen. The consequences of even a small object obstructing the beam aperture would be serious. For this reason it is desirable to have a tool at hand to detect such obstacles. To this end, microwave waveguide mode reflectometry using synthetic pulses was studied. In this chapter the Assembly Version of the LHC reflectometer was described. It is to be applied during the installation of LHC. Short sections of interconnected magnets are planned to be tested for obstacles and correct interconnect installation. Both the fundamental TE and TM mode will be used for the inspections. For the excitation of these waveguide modes, coupling structures that can be connected to the end of the beam screen at the position of the interconnects’ plug-in module are used. These coupling structures were successfully designed, simulated, manufactured and tested. The actual measurements are done on a state-of-the-art vector network analyser connected to the coupling structures. The subsequent signal processing, in

particular dispersion compensation and a graphical user interface were implemented in Matlab. The system was tested on a single fully equipped dipole and on a 50 m long run of beam screen, where obstacles as small as metallic M4 nuts could be detected. Ranges of the order of 400 m are expected, but the signal quality is expected to deteriorate for long distances due to multiple reflections. Very recently tests on the cryogenic ring line using improvised coupling structures showed pretty promising results.

## Chapter 5

# Reflectometer In Situ Version

The reflectometer Assembly Version presented in the previous chapter allows checking the beam screen for obstacles during the construction phase of LHC. Once the interconnects are installed, no direct access to the beam screen is possible any more. However, even though not very probable, it cannot be ruled out that obstacles of some kind emerge during the magnet and beam commissioning phase. Possible reasons could be

- Deformations of the beam screen during magnet quenches
- Pieces of the 75  $\mu\text{m}$  copper layer coming off
- Accidents with the machine.

Even though a bigger effort is necessary and obstacle detection is harder than in the Assembly Version, the potential benefits of having an inspection tool available *in situ* appear to outweigh the drawbacks.

### 5.1 Concept

The In Situ Version of the reflectometer consists in measuring across half an arc in reflection mode after completion of the LHC. Measurements can be performed both with and without air in the beam pipe. After cool-down, however, the copper resistivity should be small enough to finally allow checking an entire arc by looking from both sides using the  $\text{TM}_{01}$  mode. It is not planned to examine the warm sections, since they contain many cross-section changes and other discontinuities which disturb microwave propagation. Additionally there is less interest in checking those sections, since they are easily accessible compared to the cold arcs. To excite waveguide modes in the beam screen, special coupling structures have to be designed. Standard LHC button type pick-ups (Fig. 5.1(a), for example), cannot be used in the GHz range due to their excessive capacity to ground. Furthermore, ordinary pick-ups are explicitly designed not to radiate, so it can be expected that they will not excite waveguide modes, either. Coming to the signal processing, in principle the software used for the Assembly Version can be used with some adaptations. Since the in-situ reflectometer is not planned to be used extensively, there are no plans for developing a special graphic user interface or measurement procedure.

### 5.1.1 Desirable features

From the RF point of view there are many features that the couplers should possibly fulfill. The most important ones are

- Operation with both  $TM_{01}$  and  $TE_{c11}$  mode should be possible. Even though for obstacle detection mainly the  $TM_{01}$  mode is planned to be used, many of the potential side applications need a more flexible mode excitation that can also work with the  $TE_{c11}$  mode.
- Well matched for both modes. As pointed out above, a good match effectively increases the detection range and reduces the impact of multiple reflections on the signal.
- Large bandwidth. The coupler must work in a sufficiently wide frequency band in order to make measurements with high resolution possible.
- Spurious mode-free excitation. The excitation of higher order modes in the coupler has to be avoided, since they would in practice spoil the reflection signal and make the interpretation of the data very hard.
- Directivity. This property is listed for the sake of completeness. In the present design a closed sector valve that provides the directivity is needed.

### 5.1.2 Location

Several considerations led us to the final choice of the coupler location. It would have been advantageous to have many couplers installed in the cold section, however this is out of question for financial, space and accessibility reasons. With the cold sections out of the game, it has to be tried to get as close as possible to the extremity of the adjacent warm section. Waveguide attenuation after cool-down should be sufficiently low to make it possible to cover half an arc in reflection mode. However, the warm sections containing lots of beam diagnostics equipment, RF cavities and collimation systems, the beam pipe is not homogeneous in these regions. Many cross-section changes make microwave propagation in the beam pipe pretty hard. Therefore (1) the couplers need to be as close as possible to the cold sections and (2) it has to be avoided that part of the signal leaks out to the warm sections, where lots of strong reflections would spoil the picked-up reflection signal. Argument (2) suggests a long coupler with high directivity. However, the available space is restricted and in general long couplers have only a limited bandwidth. An idea to overcome these problems was to look for a place close to a sector valve (Fig. 5.1(b)). These valves can be closed to protect the arc vacuum. The hermetic vacuum seal also provides a solid short circuit for microwaves. By putting a short coupler between the vacuum valve and the cold section, high directivity can be obtained, as well. However, this relatively easy solution comes at a price.

- The coupler has to sit close to the vacuum valve as compared to the wavelength, otherwise the bandwidth will be small. A big fraction of the power will be directly reflected back to the measurement device.
- Additionally, reflectometer measurements need the sector valve to be closed. However, the latter fact is not really a limitation, since obstacle detection with beam

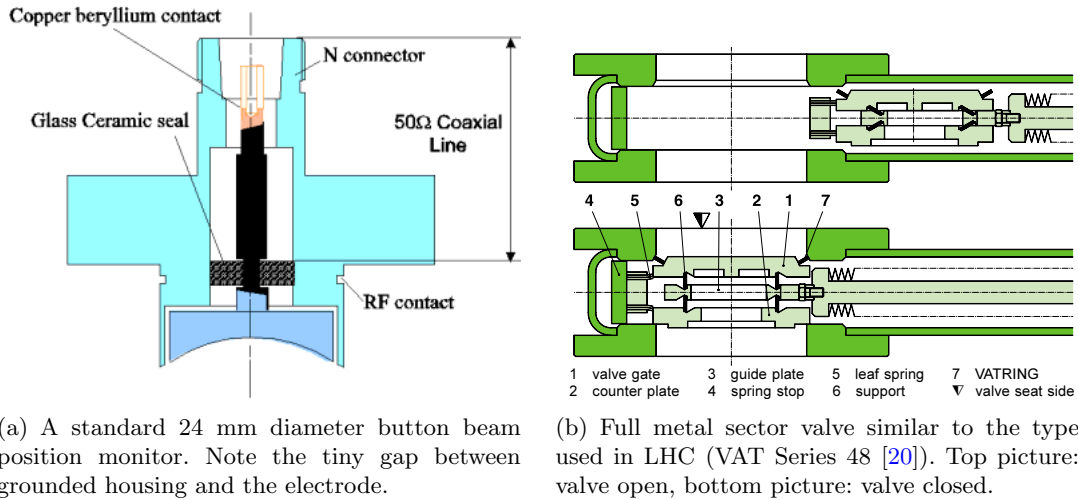


Figure 5.1:

does not make sense owing to beam-induced disturbing signals. When there is no beam for a longer time, vacuum valves are likely to be closed anyway as a safety measure.

- In general in LHC beam position monitors and other diagnostics equipment containing ceramics that might break are deliberately *separated* from the cold sections by vacuum valves. This is due to the fact that a failing ceramic might disrupt the vacuum system of an entire arc. By choosing such a special location, special precautions are needed to prevent extensive damage in the (highly unlikely) case of a ceramics break.

Right next to the sector valves on the side leading to the cold section, vacuum installations are housed in a so-called VM module. This location was found to be most suitable for the in situ reflectometer couplers, which had to be integrated in this VM module. However, a number of constraints had to be accepted and trade-offs made in order to reconcile vacuum and RF needs. The region around the end of the continuous cryostat with the VM module is shown in Fig. 5.2.

### 5.1.3 Modes of operation

The in-situ version is not planned to be operated continuously as a beam instrumentation tool. Rather, it is foreseen to be used in case of problems as a mobile device. The most probable scenario is a problem being discovered during the commissioning of the machine. Hopefully, of course, we will never come to that point but it cannot be excluded. In this case the activation of the machine should not be too critical, making longer interventions possible. The network analyser can then be connected to the couplers and measurements started.

Throughout the designing of the couplers it turned out that low-reflection coupling to the beam pipe is not easily feasible. Moreover the measurement bandwidth will be limited to few hundred MHz due to the reflection from the closed vacuum valve. For these

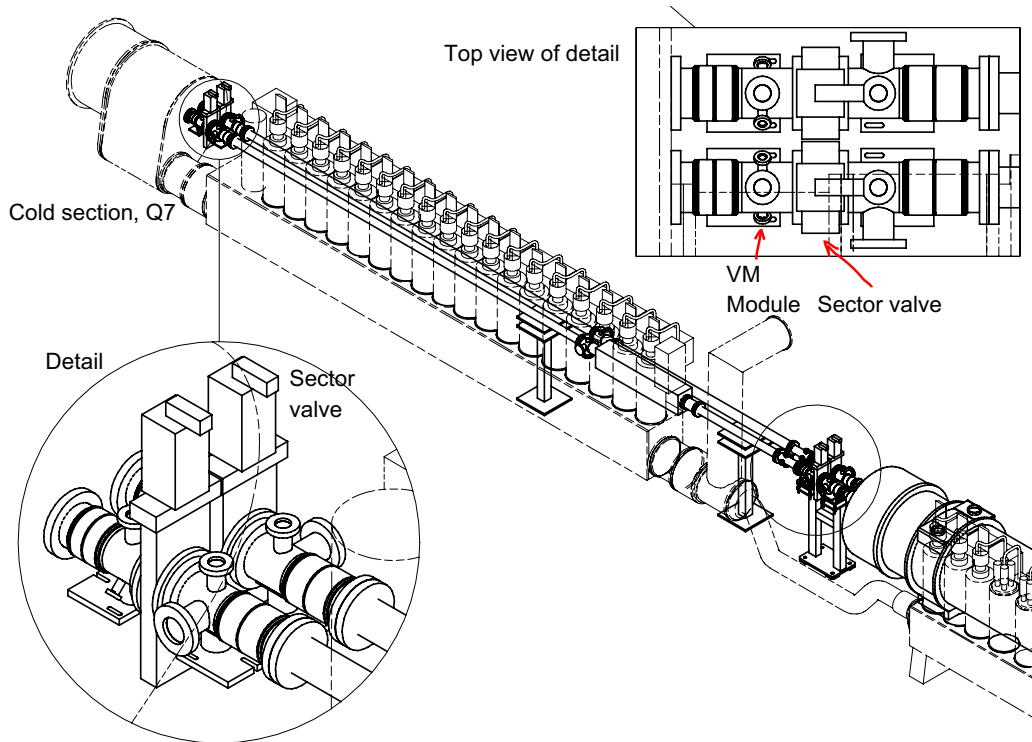


Figure 5.2: Layout of the LHC in the region of the cold-warm transition. The section left of the detail with the big cryostat is cold, the rest at ambient temperature.

reasons it will be difficult to make absolute measurements, i.e. tell without prior knowledge whether there is some problem or not. Improving the signal quality by numerical deconvolution is being considered. Currently, by default it is planned to do comparative measurements. After completion of each LHC arc, reflectometer measurements will be carried out and the results archived. Since Assembly Version inspections are planned for all these sections, it can be expected that they are clean and fault-free in the beginning. In case of a potential problem, new measurement results can be compared with previously taken data, which should considerably facilitate the search for obstacles etc. Surely over time there will be small changes in the response due to instrument drift, change of material properties and similar effects, but it should still be much easier to compare with a reference trace than to start from scratch. During cool-down the RF properties of the beam screen as well as the expanding interconnects will make the reflectometer response change. Therefore reference traces have to be taken both at room temperature and at low temperature.

## 5.2 Modified VM module

Right next to the sector valve space is scarce (Fig. 5.2). The cryogenic distribution line passes below the beam lines and not far aside the big cryostat of the cold section starts. The space constraints can be summarized as follows.

- Available length in direction parallel to the beam line: 170mm. This space has to

TE Modes	Cut-off [GHz]	TM Modes	Cut-off [GHz]
<u>TE<sub>11</sub></u>	2.786	<b>TM<sub>01</sub></b>	3.640
<u>TE<sub>21</sub></u>	4.615		
TE <sub>01</sub>	5.793	<u>TM<sub>11</sub></u>	5.793
TE <sub>31</sub>	6.345	<b>TM<sub>21</sub></b>	7.760
<b>TE<sub>41</sub></b>	8.020		
TE <sub>12</sub>	8.042	<b>TM<sub>02</sub></b>	8.328
<u>TE<sub>c11</sub></u> in beam screen	3.614	<b>TM<sub>01</sub></b> in beam screen	5.326

Table 5.1: Cut-off frequencies of the first 10 modes in a 63 mm diameter circular pipe. The beam pipe at the location of the VM module has approximately these dimensions. The modes with TE<sub>c11</sub> symmetry under 6 GHz are underlined, those with TM<sub>01</sub> symmetry are printed in bold face.

be shared with two ports of a vacuum installation.

- At this location the inner beam pipe diameter is 63 mm. This aperture can be decreased to 55 mm and possibly to 50 mm when special alignment is provided. However, this would require the installation of alignment targets and frequent realignment in order to satisfy the tighter tolerances.
- The distance between the centers of the beam lines is 194 mm. Thus, the maximum width in horizontal plane on the side next to the other beam pipe must not exceed 95mm. Already coming close to this limit makes installation complicated.

In addition to space constraints, the particular environment of LHC imposes several additional conditions.

- Impedance budget. The additional transverse impedance must be kept so low that it can be neglected.
- The formation of trapped modes must be ruled out.
- All materials must be suitable for employment in this high (ionizing) radiation area. Especially close to the collimators this region may get very hot.
- Materials on the vacuum side must comply with high vacuum requirements, no excessive outgassing etc. is allowed.

### 5.2.1 Coupler design

Based on the above requirements possible coupler designs were looked for. Two different types of couplers have been studied thoroughly. In both cases the limited length did not pose major problems. It was the aperture that turned out to be the crucial parameter. This is simply because in a larger cross-section more unwanted modes can propagate, thus rendering a spurious mode-free excitation more and more difficult. The cut-off frequencies of the first modes propagating in the 63 mm diameter round waveguide constituted by the beam pipe are given in Table 5.1. The corresponding mode patterns are displayed in Fig. 5.3.

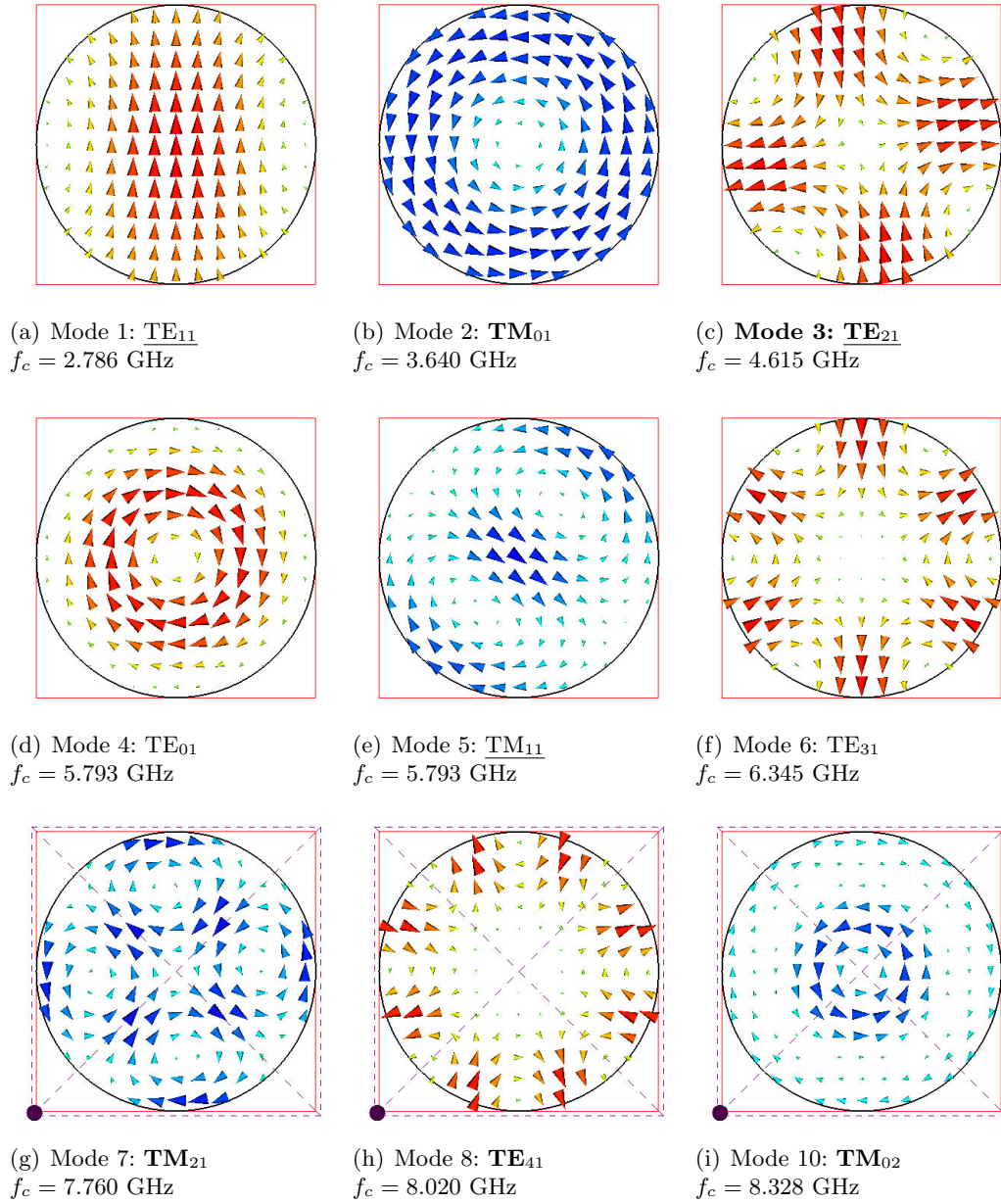


Figure 5.3: Waveguide modes in the 63 mm diameter circular pipe at the location of the In Situ Version couplers. For TE modes the E field (reddish) and for TM modes the H field (blueish) is plotted. The quoted cut-off frequencies are simulated values. The modes with  $TE_{c11}$  symmetry under 6 GHz are underlined, those with  $TM_{01}$  symmetry are printed in bold face.

A perfectly rotationally symmetric geometry would be best for exciting the  $TM_{01}$  mode, as was the case for the Assembly Version mode launcher. However, space constraints do not allow such an elegant solution. Falling back to non-rotationally symmetric geometries, the field pattern of the first modes gives some hints on how to proceed. In a circular waveguide, any excitation element for the  $TM_{01}$  mode with a two-fold symmetry will couple strongly to the  $TE_{21}$  mode, which has an even lower cut-off than the  $TM_{01}$  in the beam pipe. Three-fold symmetry will excite the  $TE_{31}$ , and, more generally,  $n$ -fold symmetry the  $TE_{n1}$  mode. However, in the round pipe the  $TM_{02}$  mode has cut-off at 8.328 GHz. Since this mode has the same symmetry properties as the desired  $TM_{01}$  mode, for the given cross-section it cannot be avoided without substantially limiting the beam aperture. Tapering the beam pipe down to an acceptable diameter of 55 mm would move this mode's cut-off up to 9.5 GHz. However, the  $TE_{31}$  cut-off would only move to 7.3 GHz, posing a major bandwidth limitation. Therefore, any coupler must at least have a four-fold symmetry to keep the excitation of the  $TE_{31}$  mode low. Furthermore, using a four-fold symmetry can be obtained easily in practice and in the simulation. In practice all you need are three identical hybrids and a couple of cables of equal length. In most simulation tools, a two-fold symmetry can be easily modelled by introducing say a horizontal symmetry plane. For the  $TM_{01}$  mode the condition is that the magnetic field is normal to this plane. A four-fold symmetry is realized in a similar way by introducing two normal magnetic symmetry planes. Apart from speeding up the simulation runs, the symmetries also remove undesired modes. Physically, a magnetic symmetry plane corresponds to exciting two ports in phase. This can be understood by looking at the electrostatic equivalent: the electric field in the symmetry plane between two equal point charges will be parallel to this plane. In practice, excitation with equal phase is realized by feeding the sum port of a 3 dB hybrid and using the signal of the two hybrid input ports. The difference port has to be terminated with a matched load. The  $TE_{11}$  mode on the other hand can be excited by using the hybrid's delta port and feeding two coupler ports in phase opposition. This condition requires an electric symmetry plane in the simulation. When four ports are used, two have to be fed in phase and the other two in opposite phase. This allows one electric and one magnetic symmetry plane to be used. For two-port excitation, the  $TE_{21}$  is the first higher order mode that gets excited, for 4 ports it is the  $TM_{11}$  mode. Since no reasonable mode excitation is possible with those higher order modes present, the only possibility consists in working at lower frequencies. This of course limits the operational frequency range and with it the potential spatial resolution.

#### Four rectangular waveguide feed lines

For the Compact Linear Collider (CLIC) project several types of mode launchers were developed. In [21] a high-performance  $TM_{01}$  mode launcher for circular waveguides is described. The function of this coupler can be understood by having a look onto Fig. 5.4.

The  $TE_{10}$  mode is excited in a rectangular waveguide. The power is then split and guided towards the circular beam pipe by two arms of equal length. The two rectangular feed waveguides join the beam pipe on opposite sides, combining their power and coupling it to the  $TM_{01}$  mode. This is possible because the  $TE_{10}$  in a rectangular cross-section and the  $TM_{01}$  mode in a circular guide have similar field patterns.

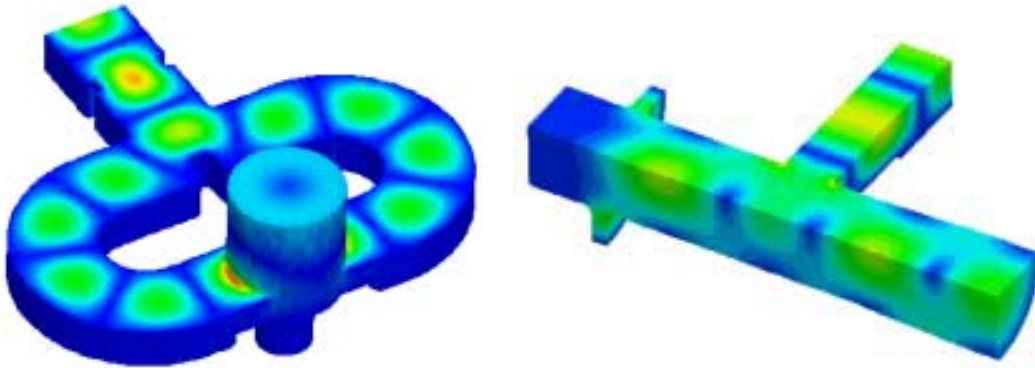


Figure 5.4: A coupler exciting the  $TM_{01}$  mode in a circular beam pipe. Left: The power in injected in the  $TE_{10}$  mode in a rectangular waveguide in the upper left corner. Right: Cut along the beam axis, with the feed line coming in on the upper right side. This structure was developed for the CLIC project [citeSyr1](#).

The right picture in Fig. 5.4 illustrates how directivity is obtained. A choke cavity placed at a suitable distance from the excitation reflects the wave back, most of the power is coupled to the accelerating cavities situated further right.

Two remarks have to be made concerning this design.

- The couplers have been designed for a high power application. It is for this reason that the power splitting is done by waveguides. For low-power applications, in principle this could also be done in a simpler way using coaxial power splitters or hybrids.
- The couplers are optimized to work well over a relatively small bandwidth. In particular the choke cavity cannot be easily made to work over a larger bandwidth.

The following design is largely inspired by the above couplers. Some modifications were necessary to adapt it to our purposes. In order to get a sufficient usable bandwidth, at least a four-fold symmetry has to be used. The choke cavities are not needed, since we can use the closed sector valves as reflector. That leads to the design depicted in Fig. 5.5(b). To push the higher order mode cut-off to higher frequencies, the beam pipe was tapered down to a minimum acceptable value of 55 mm diameter. The yellow stubs reaching out of the feed waveguides represent the coaxial feed lines.

The simulated S parameters of the structure are plotted in Fig. 5.5(a). In order to reduce CPU load, two symmetry planes were introduced: the vertical and the horizontal plane parallel to the beam axis were set as magnetic symmetry planes. This means that the magnetic field has to be normal onto these planes, which is the case for the  $TM_{01}$  mode. Modes that do not fulfill this symmetry condition are not considered, a fact that speeds up the calculation, as well. In Table 5.1 and Fig. 5.3 the modes which fulfill the  $TM_{01}$  symmetry condition are printed in bold face. The first two modes having the required symmetry, the  $TE_{21}$  and the  $TM_{21}$  mode are not excited in theory since their electric fields at the location of the feed waveguide do not have the right orientation. Thus, the first mode being strongly excited is the  $TE_{41}$  mode with cut-off at 9.2 GHz in a 55 mm diameter pipe. The corresponding peaks and drops in the transmitted power can be clearly seen in the simulated S parameters in Fig. 5.5(a).

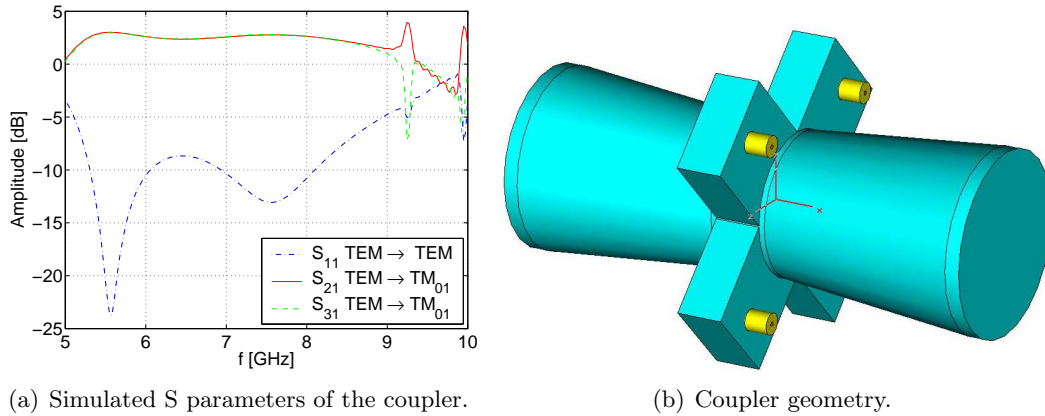


Figure 5.5: Four rectangular feed waveguides for  $TM_{01}$  mode excitation in a 55 mm diameter beam pipe.

Coming back to the simulation, a one-port excitation of the coaxial feed lines was used for the incident wave. Two additional waveguide ports were defined at the extremities of the beam pipe. A closer look onto the simulated S parameters shows values clearly above 0 dB. This is due to the symmetry planes, which in practice multiply the input power by two for each plane. Therefore the results need to be compared to the total incident power of +6 dB. Conversely, the reflected power has to be multiplied by 4, since only the power coming out of *one* input port is obtained in the simulation.

Another important point was not considered in the above structure, either. The close-by vacuum valve will reflect all the power incident on it, giving rise to a standing wave. For some frequencies the power transmitted to the beam pipe will thus double, for others the waves will cancel. With a distance of roughly 10 cm to the vacuum valve, several transmission bands will appear, each a few hundred MHz wide. In principle, the full reflection can be studied analytically based on the simulated S parameter set. The difference between transmitted and reflected power in the frequency bands with constructive interference can be evaluated. A maximum value of  $S_{21} = 3 \text{ dB} + 3 \text{ dB} = 6 \text{ dB}$  in bands of constructive interference is found for the transmission. With the simulated  $S_{11} \approx -10 \text{ dB} + 6 \text{ dB} = -4 \text{ dB}$  due to symmetry planes,  $S_{21}$  is found to be 10 dB higher than  $S_{11}$ , corresponding to an insertion loss of 0.5 dB.

The field pattern of the excited  $TM_{01}$  mode is plotted in Fig. 5.6. Unfortunately it is not possible at all to use this structure for TE modes. Changing the feed waveguides can be thought of, but such a major modification once the installation is finished would be prohibitively complicated.

#### Four buttons

Staying with the four-fold symmetry, we came up with another structure. Apart from electrostatic pick-up electrodes, buttons can be used for waveguide mode excitation, as well. However, the coupling decreases fast when the buttons are retracted from the beam pipe aperture. A useful coupler needs buttons that penetrate at least a few millimeters into the beam pipe. The principle design is shown in Fig. 5.7. Four buttons are mounted on the inner conductors of 50  $\Omega$  coax transmission lines. It was found in

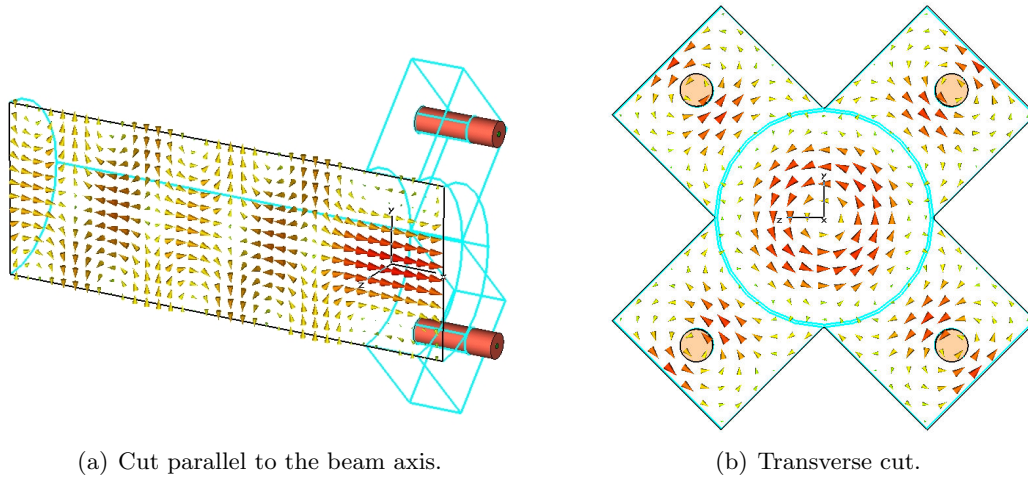


Figure 5.6: Field pattern of the  $TM_{01}$  mode in a coupler geometry without tapering. The brownish shaded circles in the four waveguide stubs represent the center conductor and dielectric of the coaxial excitation.

numerous simulation runs that good coupling can be obtained for coaxial lines with about 15 mm diameter. Owing to its rotational symmetry, for the  $TM_{01}$  mode the azimuthal orientation of the set of buttons is not critical. However, space constraints and a better  $TE_{c11}$  performance suggested rotating the buttons by  $45^\circ$  with respect to the vertical plane.

For reducing higher order mode excitation it would be advantageous to reduce the diameter of the beam pipe. However, this would prevent letting the buttons reach into the beam pipe without further constricting the beam aperture. Conversely, increasing the beam pipe diameter would be possible in order to let the buttons penetrate deeper, but at the price of reduced bandwidth due to higher order modes, higher mechanical complexity and possible problems with trapped modes. Therefore it was decided to stick to the 63 mm beam pipe diameter.

Figure 5.8 shows the  $TM_{01}$  mode on the four button coupler. The bends in the coaxial feed lines are necessary for setting up the simulation, since Microwave Studio accepts only waveguide ports parallel to the coordinate axis<sup>1</sup>. The bending radius was made large enough that no significant change in the properties resulted. From the mode pattern the excitation of the  $TM_{01}$  mode can be seen, as well as a strong similarity to the  $TE_{41}$  mode. Indeed, the S parameters in Fig. 5.8(a) show a very strong  $TE_{41}$  excitation above 8 GHz. Again the raw results have to be interpreted with care. For the following plots, including Fig. 5.8(a), the S parameters have been corrected for the symmetry plane effect.  $S_{11}$  is the power being reflected back to *one* coaxial line. The value for  $S_{11}$  is correct, since the incident as well as the reflected wave represent a quarter of the total incident or reflected power.  $S_{21}$  and  $S_{31}$ , however, have to be corrected, thus reduced by a factor 4 or 6 dB. As a cross-check, the summed power of all the modes is

<sup>1</sup>In more recent versions of Microwave Studio that later became available at CERN, it was also possible to simulate the given structure without bent feed lines by suitably combining the results for each port. This considerably reduced CPU time, but the results did not differ significantly from those obtained before.

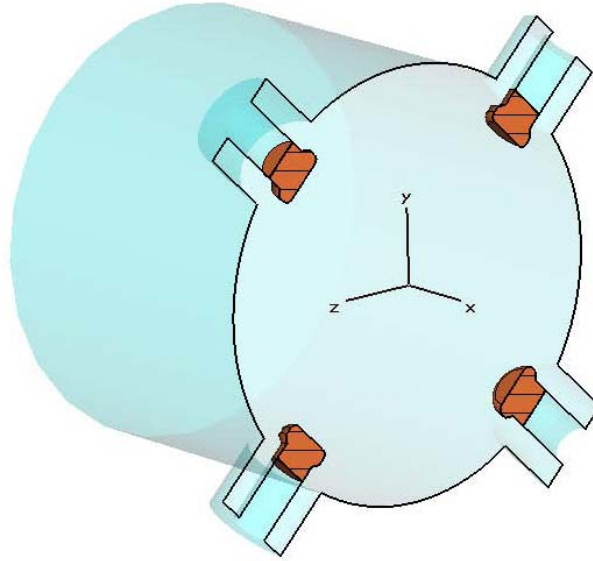


Figure 5.7: Geometry of the four button type pick-up for waveguide mode excitation in the beam pipe.

plotted, as well (dashed cyan trace). Apart from the regions close to some higher order modes' cut-off, the data is consistent.

In the structure used, Port 1 was the coaxial line and waveguide ports were set at the left and the right extremity of the beam pipe. The first mode fulfilling the symmetry conditions in the beam pipe, the wanted  $TM_{01}$  mode, can thus propagate both ways. Its power is split between  $S_{21}$  and  $S_{31}$ . This situation corresponds to an open vacuum valve. However, to speed up the simulations, multi-mode propagation (four modes) was allowed only at Port 2. Therefore, in the model, the higher order modes are reflected on one beam pipe end, they can only leave the beam pipe at Port 2 or actually couple back to the coaxial line.

The traces representing the transmitted power in the desired  $TM_{01}$  mode (solid red and dashed green) are about 5 dB below the reflected power (solid blue). When the vacuum valve is closed, the resulting standing wave pattern should have maxima about 3 dB higher than the actual  $S_{21}$  trace, resulting in a minimum insertion loss (magnitude of  $S_{21}$ ) of about 5 dB. Special simulation runs with the reflection of the vacuum valve included will be discussed later. Furthermore, the penetration depth of 7 mm in the present structure cannot be allowed without special alignment of the VM module.

The same simulations were run with  $TE_{11}$  mode excitation (Fig. 5.9). In the simulation, this requires again two symmetry planes, an electric and a magnetic one. Contrary to first assumptions, the present structure with the buttons at a  $45^\circ$  angle performed better than two single buttons excited with opposite phase. The vacuum valve reflection taken into account, a minimum insertion loss of about 8 dB can be reckoned with.

Departing from the classic button geometry as discussed above, various coupling structures have been examined. Other geometrical shapes, such as hooks or loops did not yield any significant improvements. For the buttons structure, the most important parameters were found to be the penetration depth  $p$  and the radius of the end plate  $r$ . The outer radius of the coaxial line  $r_a$  plays a certain role, too. Several simulations

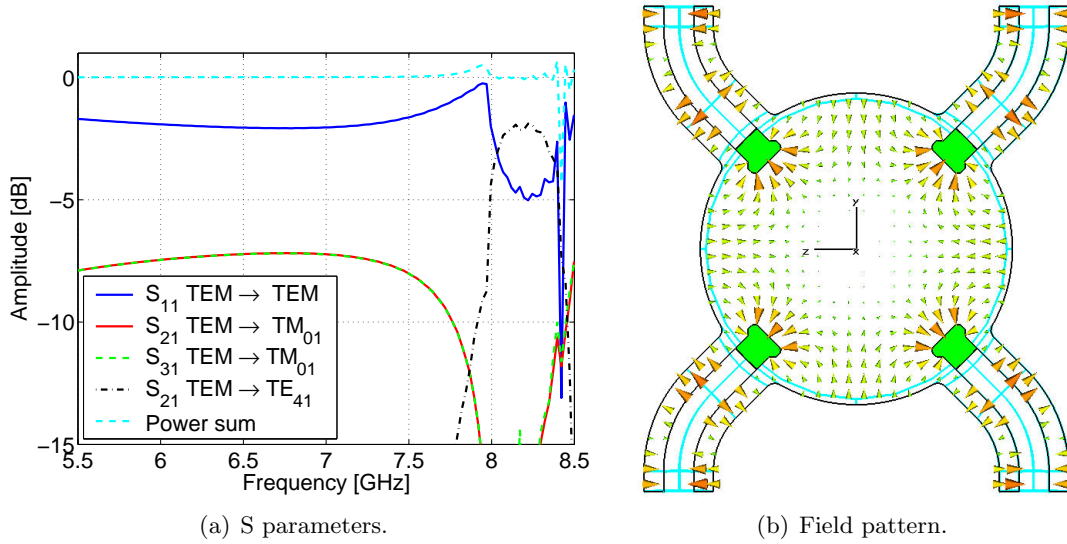


Figure 5.8: Simulation of the  $TM_{01}$  mode in the 4 button coupler. The penetration depth is 7 mm, leaving 49 mm of free aperture.

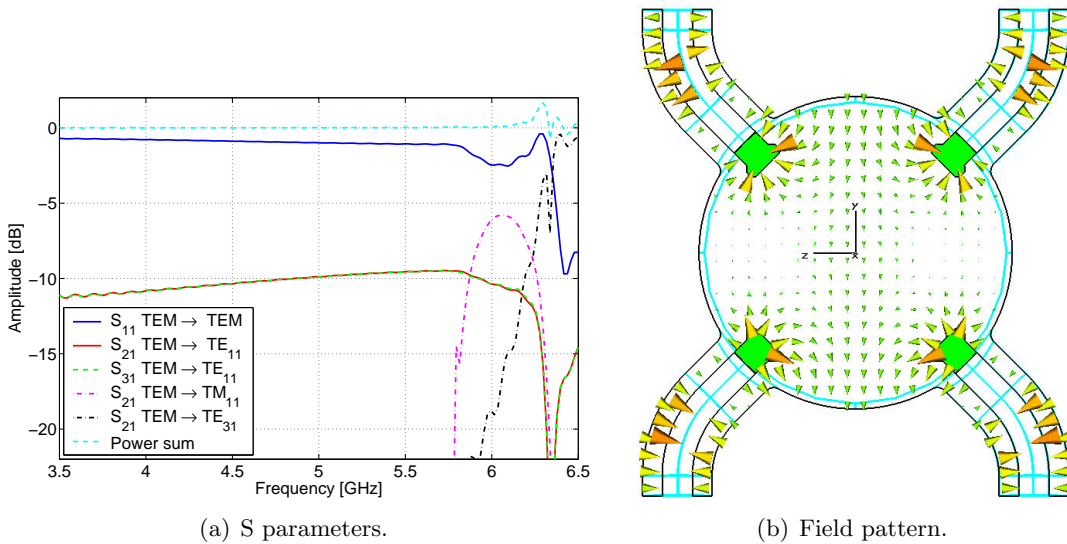


Figure 5.9: Simulation of the  $TE_{11}$  mode in the 4 button coupler. The penetration depth is 7 mm, leaving 49 mm of free aperture.

showed a shallow optimum in the range of  $6 \leq r_a \leq 9$  mm, with the minimum around  $r_a = 7$  mm. For  $r_a \approx 9$  mm waveguide modes start to propagate in the coaxial feed line. This should be not a serious problem in practice, provided that the buttons are well centered and symmetric, but it makes the simulation unstable. Too big feed lines are not practical from the installation point of view, either, so we stuck to  $r_a = 7$  mm for the first detailed analysis. Another important parameter is the end cap thickness, while its exact shape does not play a too big role. Rounded end caps with thickness  $d = 3$  mm and blending radius 1 mm were used. Varying  $p$  and  $r$ , the following observations were made:

- TM<sub>01</sub> mode
  - Very strong dependance on  $p$ . Coupling gets better for increasing  $p$ .
  - Weak dependance on  $r$  in the range  $4 \leq r \leq 6$  mm for  $p = 7$  mm and probably also for other values of  $p$ .
- TE<sub>11</sub> mode
  - Very strong dependance on  $r$ , with best performance found at  $r = 4$  mm for  $p = 7$  mm.
  - Strong dependance on  $p$ , getting better for higher  $p$ .
- For both modes it was found that increasing the end cap thickness decreases the coupling strength. This is valid at least in the range  $0.5 \leq d \leq 3$  mm. However, for small  $d$  around 1 mm, the coupling strength appears to reach a maximum. This is probably only due to the limited accuracy of the simulation. This effect was not investigated in more detail since buttons with caps thinner than 1 mm are unacceptable for various practical reasons. Rounding off the edges of the end cap does not have a big effect, apparently it simply makes the cap seem a bit smaller in diameter and thickness.

The previous design was done during preparatory studies. In order to fully adapt it to the installation requirements, several changes had to be implemented. The new design is depicted in Fig. 5.9. There are several important differences compared to Fig. 5.7.

- Owing to aperture restrictions a design with buttons reaching only 4 mm into the beam pipe had to be chosen. This was necessary since it was deemed too complicated to guarantee perfect alignment by installing special alignment targets and including the VM module in the list of elements needing high-precision alignment.
- Since thick end caps turned out to be disadvantageous, a cap thickness  $d = 1$  mm was used as a trade-off between easy manufacturing and good performance. Edge blending is still possible to some degree, so that the buttons are less susceptible to sparking when high voltages are applied. This might be interesting for a potential fringe application.
- In cooperation with the AT-VAC group the design for the entire VM module was finalized. The center of the pick-up buttons is now located  $\approx 113$  mm from the sector valve flange. When the shutter is closed, on the vacuum side its surface

will be about 19 mm from the flange. Therefore the closed valve was modelled as a perfect short circuit 132 mm to the side of the buttons. A standing wave will build up between the buttons, leading to frequency bands of high and low transmission.

- The vacuum feed-through used will sit on a CF16 flange (16 mm inner diameter). This is the standard size used in vacuum technology coming closest to the optimum outer button diameter of about 14 mm obtained in simulations. Aside the CF25 flanges that are not among the standard components used in LHC, the next size would have been CF40, which – obviously – is way too big. The slight diameter increase to 16 mm does not significantly change the RF performance.

Incorporating the design changes and the things learned from previous simulation runs, the following model was used (Fig. 5.10). Changes and special simulation settings include

- Higher order modes. Previous simulation runs showed that for the  $TM_{01}$  and the  $TE_{11}$  mode higher order modes get strongly excited at around 8 and 6 GHz, respectively. The operational frequency range is sharply limited by this fact. If these modes are included in the simulation, they will just increase the time to converge, giving not much additional information. Therefore, as a first step, the upper frequency limit for the simulation was decreased as much as possible (5.8 to 8 GHz for  $TM_{01}$  and 3.8 to 6 GHz for  $TE_{11}$  mode). This limits the number of modes that can propagate. When a higher order mode is excited at the buttons but cannot leave the structure through the waveguide port on the left because the latter was set not allow this specific mode, then this mode is reflected back and forth. The transient solver used can be understood as a time domain excitation of the coupler. With relatively much power circulating in the structure the algorithm does not converge fast. Therefore, exceptionally, specifying a higher number of modes on the port 2 can improve convergence and speed up the simulations. For  $TM_{01}$  simulations, the first three modes were included in the calculations in certain cases, while only the first mode turned out to be sufficient for the  $TE_{11}$  runs. Increasing the length of the distance of Port 2 from the buttons to give the evanescent mode space to decay did not turn out to help much.
- Adaptive meshing. Already with the mesh automatically generated by Microwave Studio Version 5 pretty good results were found. A cross-check forcing four mesh refinements showed only minor variations in the frequency response on from the first mesh refinement. Only the higher order mode responses at the limit of the frequency range changed significantly but they are not of primary interest for us. In order to rule out a potentially deteriorating higher order mode influence on the mesh refinement process, a smaller frequency range was used for adapting the meshes (6 to 7.8 GHz for  $TM_{01}$  and 4 to 5.5 GHz for  $TE_{11}$  mode). Therefore, in order to minimize calculation time, the mesh obtained after the first refinement was used for most of the subsequent parameter sweeps. The number of mesh cells was roughly  $1 \cdot 10^5$  for the  $TM_{01}$  and  $5 \cdot 10^4$  for the  $TE_{11}$  mode. The difference comes from the higher  $TM_{01}$  frequency range, requiring finer meshing. For a non-high precision simulation (“accuracy”  $-30$  dB) with one mesh refinement, the solver times were of the order of 1 minute for the  $TE_{11}$  and 10 minutes for

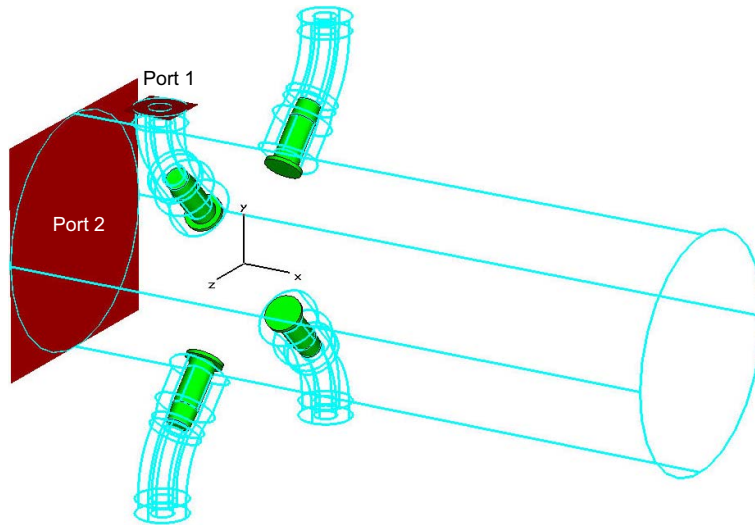


Figure 5.10: Model for the simulation and optimization of the 4 buttons coupler. The structure is excited with a TEM wave coming at the top port (Port 1), the modes coupled to the beam pipe are calculated at the port to the left (Port 2).

the  $TM_{01}$  mode on a Pentium 3 with 2.4 GHz clock rate and 256 MB RAM. The “accuracy” here is the maximum S parameter change that has to be under-run for the simulation to abort. Due to the fact that both  $S_{11}$  and  $S_{21}$  are way above  $-30$  dB over most of the frequency range, this appears reasonable. This assumption was later confirmed by re-running a simulation with the accuracy set to  $-60$  dB.

- Feed line bends. The slight increase in the outer button diameter compared to the previous simulations (from 14 to 16 mm) required a change in the geometry, e.g. an increase in the bending radius of the coaxial feed lines. In order to reduce the size of the structure, a coaxial line with outer diameter 14 mm was used, opening up to a diameter of 16 mm about 10 mm before reaching the beam pipe. Separate simulation of the cone transition showed reflection coefficients of the order of  $-40$  dB for this small discontinuity.
- Blending of the button edges was not considered in the simulation for the time being. For cap thicknesses of the order of 1 mm, this would have entailed only small changes, since the mesh size in the region of the buttons is in the same order of magnitude. In addition to that, Microwave Studio can model edges pretty well using an analytical singularity model. Introducing such a fine structure would probably have not much effect apart from increasing simulation time.

The two main free parameters, the end cap radius  $r$  and its thickness  $d$  were varied for both  $TM_{01}$  and  $TE_{11}$  mode. The former was swept in the range  $3.5 \leq r \leq 8$ , that is, from the case of no end cap at all to a button the same size as the outer feed line diameter. For the end cap thickness, values between 0.5 mm and 3 mm were considered. The fixed parameters are the depth of button penetration  $p = 4$  mm, the outer feed line radius  $r_a = 8$  mm and the distance of the vacuum valve  $d_{short} = 132$  mm. In the following, the results of the parameter sweeps are summarized. The main criterium was the magnitude of  $S_{11}$  at the frequencies of the transmission maxima.

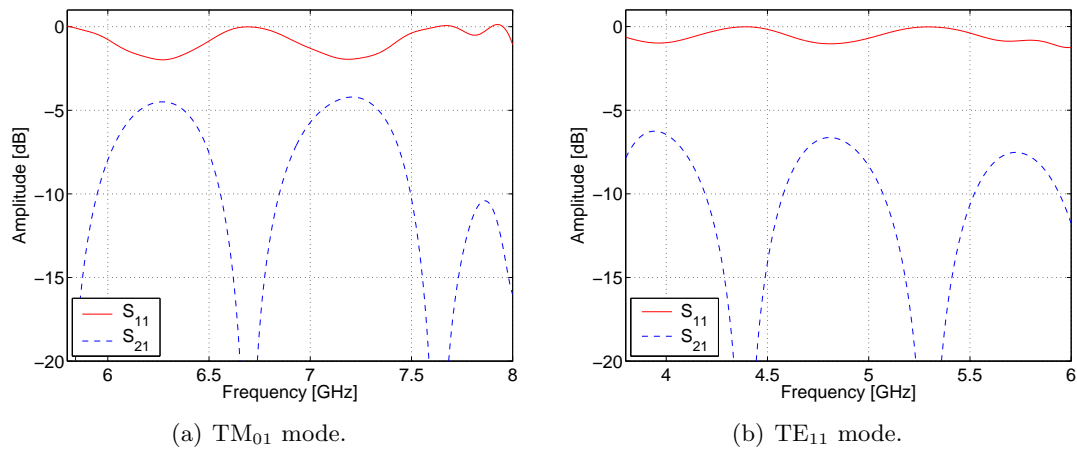


Figure 5.11: Simulated S parameters of the final button structure for the in-situ coupler.

- $TM_{01}$  mode
  - Dependence on  $r$ . Optimum between  $r = 5$  and  $r = 5.5$  mm, significantly higher  $S_{11}$  for lower  $r$  (0.5 dB higher  $S_{11}$  for  $r = 3.5$  mm). Above  $r = 7$  mm resonances appear at the end of the button between the end cap and the close-by outer conductor, which excludes  $TM_{01}$  mode operation in this range of  $r$ .
  - Dependence on  $d$ . In general, thinner end caps show better coupling. The effect is significant with an improvement of 0.3 dB in  $S_{11}$  going from  $d = 2$  mm to  $d = 1$  mm. For smaller values doubts exist about the validity of the results. Not too much work was spent on this topic, since most probably other considerations, such as mechanic stability, ease of manufacturing and sparking will be decisive.
- $TE_{11}$  mode. Response gets significantly better for increasing  $r$ , with an optimum in the range between  $r = 6$  and  $r = 7$  mm.

Considering the above results and the fact that the  $TM_{01}$  mode is the main field of operation for the reflectometer, a button diameter of  $r = 5.5$  mm was chosen as the final design. This value is slightly higher than the  $TM_{01}$  mode optimum, but the differences are small and edge blending will make the cap look smaller. For the end cap width,  $d = 1$  mm was chosen for practical considerations. The S parameters of this structure are plotted in Fig. 5.11.  $S_{21}$  was corrected by 6 dB to compensate for the known symmetry plane effect. The minimum insertion losses in the transmission bands are about 4.5 dB for the  $TM_{01}$  mode and 6.5 dB for the  $TE_{11}$  mode, respectively.

## 5.2.2 Realisation of adopted design

The most recent version of the modified VM module is shown in Fig. 5.12. In the drawing on the left side the continuous cryostat of the dispersion suppressor and cold arc starts a few centimeters left. On the right flange the sector valve is connected. In Fig.

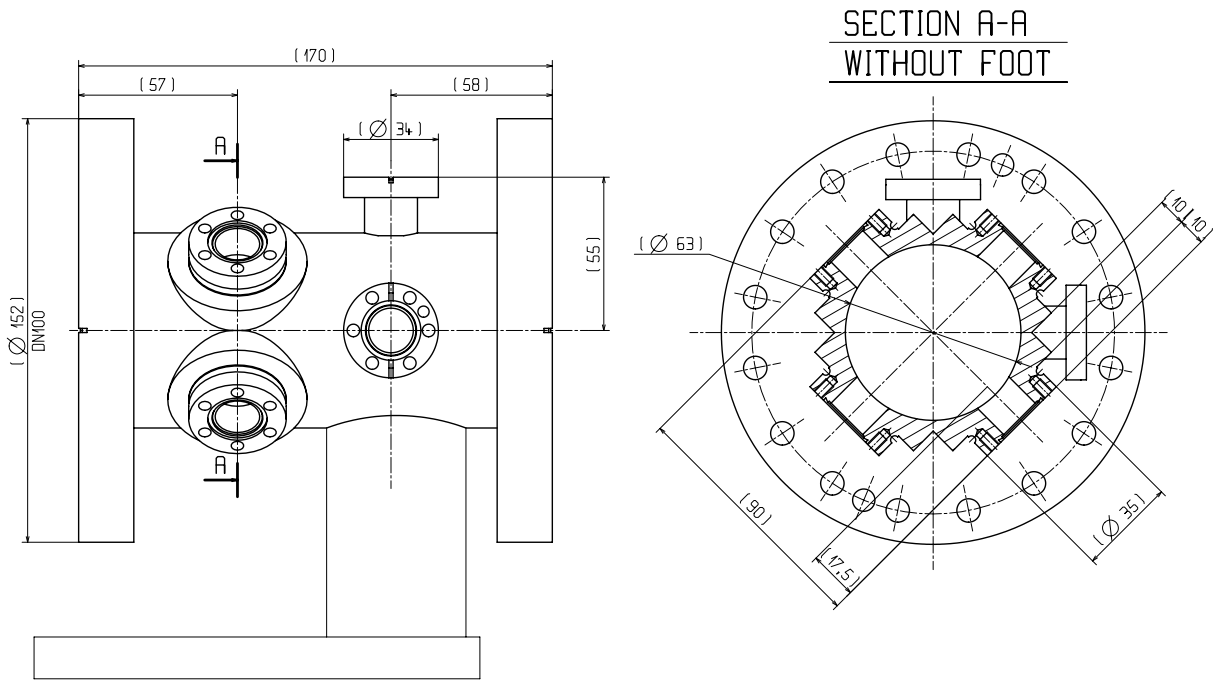


Figure 5.12: Modified VM module.

5.13 the principal button installation is illustrated. The buttons are protected from mechanical forces by hermetically sealed metal caps. In the extremely improbable case of vacuum leak of the feed-through, the cap can be pumped easily via the pre-installed vacuum flange.

Coming to the RF components, starting from the inside of the beam pipe, the mushroom-shaped button is sticking 4 mm into the aperture. A short  $50 \Omega$  line goes radially outwards to the vacuum-tight feed-through, provided with an SMA connector on the outside. An about 120 mm long RG 316 type or similar coaxial cable then goes to another vacuum-tight SMA feed-through. After installation the short cable will be wound up in the interior of the cap.

Per default each button will be terminated by a matched load. In case of measurements being done, the desired mode can be excited by feeding the buttons with the right phase. By using three 3 dB hybrids either the  $TE_{c11}$  or the  $TM_{01}$  mode can be launched in one beam pipe.

### 5.3 Performance

For the performance parameters of the In Situ Version we have to rely on simulations and extrapolations, since the VM module has not gone into production. Nevertheless, key parameters such as range and sensitivity shall be addressed here.

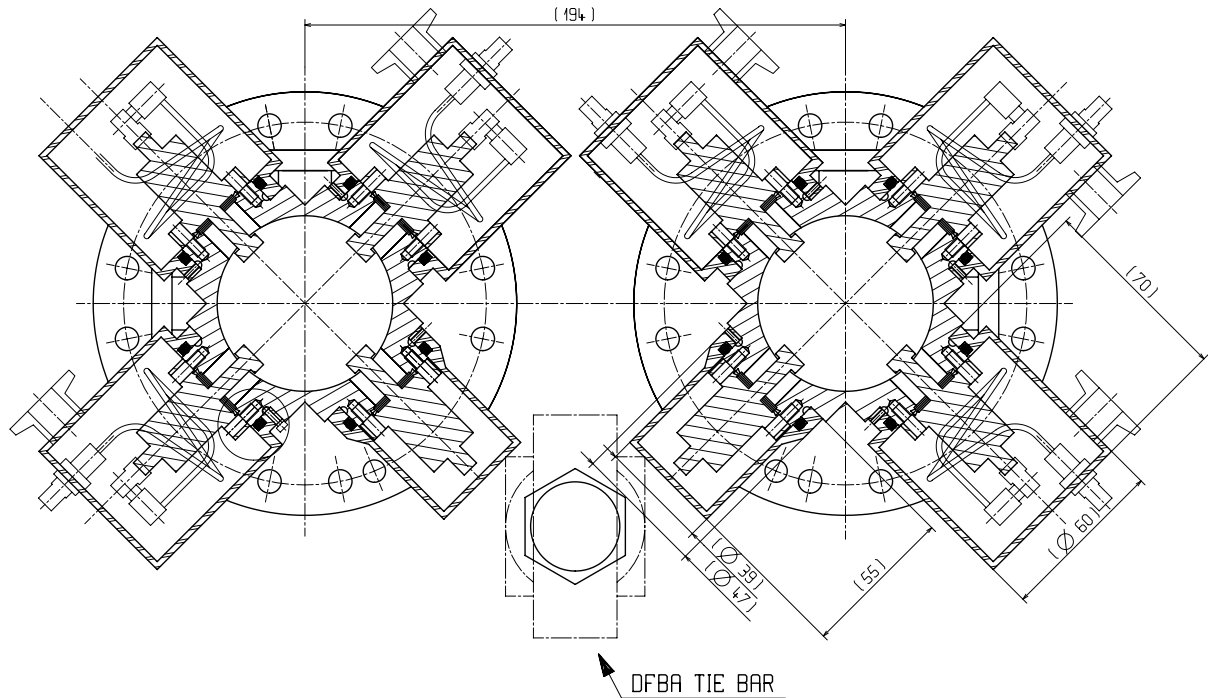


Figure 5.13: Cross-section of a preliminary version of the buttons installation on the VM module.

### 5.3.1 Range

Measurements have to cover one entire arc including the dispersion suppressors. Looking from one side in reflection mode, a range of 1400 m is necessary. Basing the estimation on the  $TM_{01}$  mode, which has better coupling and lower attenuation than the  $TE_{c11}$  mode, we find from Fig. 5.11(a) an insertion loss of about 5 dB. An estimation of the waveguide attenuation is given in Table 2.2. At low temperature without magnetic field 0.028 dB/m were found. Assuming a network analyser dynamic range of 125 dB (E8358A with 10 Hz IF bandwidth) and a typical obstacle size of  $-20$  dB, we get from Equation 3.5

$$R = \frac{125 \text{ dB} - 10 \text{ dB} + (-20) \text{ dB}}{2 \cdot 0.028 \text{ dB/m}} = 1700 \text{ m}. \quad (5.1)$$

The insertion losses were accounted for by subtracting  $2 \cdot 5$  dB from the network analyser's dynamic range. If current estimations hold, an arc can thus be covered at low temperature. At ambient temperature the  $TM_{01}$  mode line attenuation is higher (0.06 dB/m) and the range decreases to about 800 m, representing about 60 % of an arc's length.

### 5.3.2 Sensitivity

As can be seen in Fig. 5.11(a), acceptably good coupling can be only expected in two about 300 MHz wide bands. Due to the long range, very small windows must be applied in the Fourier Transform, implying e.g. Kaiser windows with  $\beta = 11$ . Scaling from Table 3.1, a 6 dB peak width of about 90 cm is found for  $TM_{01}$  mode operation. However, relatively high insertion losses of the coupling structure and the full reflection of the

closed vacuum valve, additional pulse broadening can be expected. In the case of the vacuum valve, the impact on the pulse length should not be too big, since the short circuit is only at 13 cm distance from the buttons. However, the convolution of the pipe's response with the button and vacuum valve reflection may pose problems. It should still be possible to identify "bigger" obstacles, especially in relative measurements comparing with a stored reference trace.

## 5.4 Potential fringe applications

Aside from the reflectometer there are several potential fringe applications for the coupler structures. They were taken in consideration for the coupler design, as well. Here is a list of the most interesting potential fringe applications.

- Use as clearing electrodes with a DC voltage. Dust particles could be prevented from entering the cold arcs by applying a static voltage on the buttons.
- Use as pick-up at 8 GHz and above
- Measurement of the change of the beam screen resistivity after cool-down and during the ramping of the magnetic field. The  $TM_{01}$  attenuation at 7 GHz at room and cryogenic temperature was estimated to 0.06 and 0.028 dB/m, respectively (Tab. 2.2). For a transmission measurement over an entire arc (2800 m) including 10 dB insertion loss, an attenuation of 180 and 90 dB is found. The estimated 180 dB room temperature attenuation is excessive but not prohibitively high. Assuming a simple CW measurement with a spectrum analyser with 10 Hz resolution bandwidth on the far side, with the thermal noise level at  $-174$  dBm/Hz, a source power above  $-174$  dBm + 180 dB + 10 dB = 16 dBm is necessary. Allowing a few dB for amplifier noise figure etc, we get a  $> 20$  dBm source power, which is easily feasible at 7 GHz.

For transmission measurements at low temperature, the 90 dB attenuation is acceptable.

- Measurement of the interaction between waveguide modes and the electron cloud. A waveguide transmission experiment like the one carried out in the SPS (see next part) can also be imagined for the LHC. However, since the measurements have to be carried out with beam, restrictions are imposed on the measurement set-up. About 30 m long feed cables between racks in alcoves and the pick-ups in the tunnel will be necessary, giving an extra  $\approx 12$  dB attenuation. Assuming a CW signal with 20 dBm source power and a 10 Hz detection bandwidth, the available dynamic range is 20 dBm source power  $-((-174$  dBm + 10 dB) noise level + 12 dB coaxial line attenuation + 90 dB waveguide attenuation and insertion losses) = 82 dB. Potential electron cloud-related attenuations of 0.03 dB/m can therefore be measured directly.

Since these measurements are performed with beam in the machine, no human operators can be in the tunnel. Long cables for signal transmission to the surface or remote-controlled measurement equipment would be necessary. Recent induced radiation simulations suggest that the dose rate should not exceed 1 Gy/year in the cavities next the reflectometer coupling modules [23]. It should thus be

possible to install conventional RF measurement equipment in these places for an uncritical task such as an RF transmission measurement.

For the reflectometer, the  $TM_{01}$  mode is particularly interesting but some of the potential applications outlined above  $TE_{c11}$  mode operation would be preferable.

## 5.5 Summary

In addition to the Assembly Version of the LHC reflectometer for inspection of the beam screen during installation, the In Situ Version will make reflectometry measurements possible after completion of the LHC. To this end, customary couplers will be installed at the end of each continuous arc cryostat in the warm section. The couplers have been designed and simulated; operation with both the fundamental TE and TM mode in the beam screen is possible. For reflectometry measurements, the neighbouring sector valve has to be closed in order to avoid signals coming back from the generally not very homogeneous beam pipe in the warm section. Due to the numerous restrictions in the coupler design, the coupling strength is expected not to be as good as for the Assembly Version couplers. However it is still expected to perform satisfactorily. Absolute measurements without prior knowledge are expected to be difficult due to rather big insertion losses and the full reflection from the closed vacuum valve. Therefore, reference measurements after the completion of each arc are foreseen in order to facilitate the identification of any obstacles that might crop up later. Besides reflectometer operation a number of potential fringe applications for the coupling structures are discussed.

## Part III

# Microwave transmission diagnostics

# Chapter 6

## Electron cloud effect

The electron cloud (EC) effect is an important phenomenon in high-intensity particle accelerators. Good examples are the CERN SPS, the Los Alamos National Laboratory Proton Storage Ring and BNL's Relativistic Heavy Ion Collider. In future machines that are currently in construction, in particular CERN's LHC and the Spallation Neutron Source in Oak Ridge, Tennessee, the EC is a major issue which may limit performance. Intensive work is going on in major accelerator labs where this effect has been found, centered on the development of simulation codes, measurement techniques and studies of EC mitigation.

### 6.1 Introduction

The EC effect is the result of beam-induced multipacting. Primary electrons are accelerated towards the center of the beam-pipe by the potential of a passing particle bunch. For "short" bunches, like the 5 ns LHC bunches, the electrons just get a kick. On the other hand, in long bunches they are captured at the bunch head and kept by the beam potential in the center of the beam pipe until the falling edge of the bunch, when they are released. In either case the accelerated electrons eventually hit the wall of the beam pipe, releasing secondary electrons. These electrons can again be accelerated by the following bunch, leading to a resonant electron build-up. This process is illustrated for an LHC beam with 25 ns bunch spacing in Fig. 6.1.

Primary electrons are always available in an accelerator beam pipe. They can be generated by several mechanisms.

- Photoelectrons are emitted when synchrotron radiation hits the beam pipe.
- Residual gas is ionized by the beam.
- Lost beam particles impacting on the beam pipe lead to the generation of ions and electrons.

In the LHC at injection energy, the main sources of primary electrons are residual gas ionization and beam loss, while at top energy electron generation is enhanced by photoemission from synchrotron radiation [2].

Whether a significant electron build-up occurs depends on several factors related to (1) surface effects, (2) chamber geometry and (3) machine parameters [29]. Surface effects include

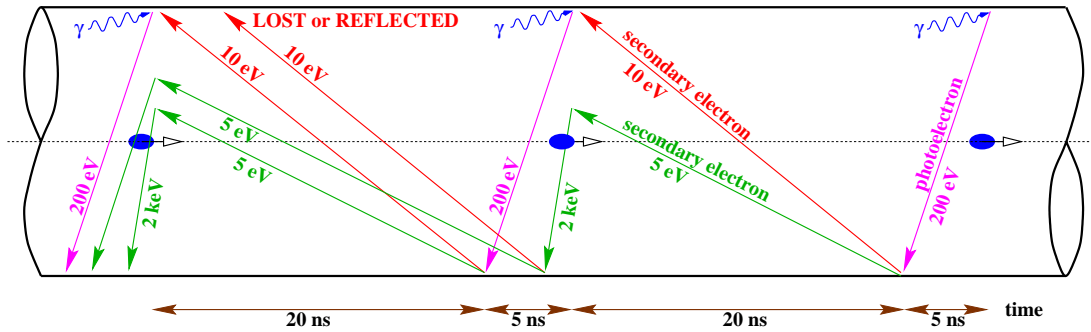


Figure 6.1: The EC build-up in the LHC beam pipe (courtesy F. Ruggiero). An electron created by synchrotron radiation is accelerated by the first (rightmost) bunch. Secondary electrons are freed when this electron hits the wall. These electrons are in turn accelerated by the second bunch. For certain beam, surface and chamber parameters a resonant build-up can occur: the electron cloud.

- Photoelectron yield. When the photoelectron yield of the beam pipe is high, more seed electrons will be available.
- Photon reflectivity. It should be avoided that the synchrotron light gets reflected along the beam pipe, because otherwise it can free secondary electrons more efficiently. For that reason a saw-tooth pattern is foreseen in the outer side of the LHC beam screen which is meant to intercept synchrotron light at angles close to  $90^\circ$ .
- Secondary electron yield (SEY). This parameter is one of the main factors for EC generation. It gives the average number of electrons freed for one impinging electron. The SEY has a strong dependence on electron energy, angle of incidence and of course the type of material used. Secondary emission can be minimized by coating the beam pipe surface with low SEY materials, such as TiZr and TiZrV non evaporable getter (NEG) thin film coatings [30]. All warm sections in LHC will be coated with the getter material TiZrV, which has to be activated by heat treatment under about  $250^\circ\text{C}$ . Afterwards it provides both low SEY and pumping of residual gas [35].

Recently it has been proposed to cover beam pipe surfaces with a longitudinal groove in order to prevent the secondaries from directly escaping the surface [31]. However, this approach may present problems related to the high frequency beam pipe impedance.

Another way to reduce secondary electron flux is by adapting the chamber geometry. The addition of an antechamber on the outer side of the beam pipe has proved useful e.g. in Berkeley's Advanced Light Source. The synchrotron light will liberate electrons mostly in the antechamber, where they do not see the beam field. Therefore they will not enter the multipacting process.

Finally, there is a variety of beam parameters that have an influence on the EC formation.

- Bunch current. A higher bunch current gives rise to higher beam fields, which in general are more efficient in accelerating electrons.

- Bunch spacing. When the bunch spacing increases, at some point the EC will have enough time to decay between two bunches, preventing a resonant build-up.
- Bunch length. Changing the bunch length impacts the beam potential and the wakefield, which in turn influence the EC build-up.
- Magnetic field. The strength of the magnetic field as well as the field configuration have an impact on the electron cloud dynamics. In inhomogeneous magnetic fields, e.g. quadrupoles, electron trapping can occur, potentially enhancing the EC effect.

It is here where performance limitations for colliders arise. The number of events  $N_{event}$  per second in an LHC collision point is given by [2]

$$N_{event} = L\sigma_{event} \quad (6.1)$$

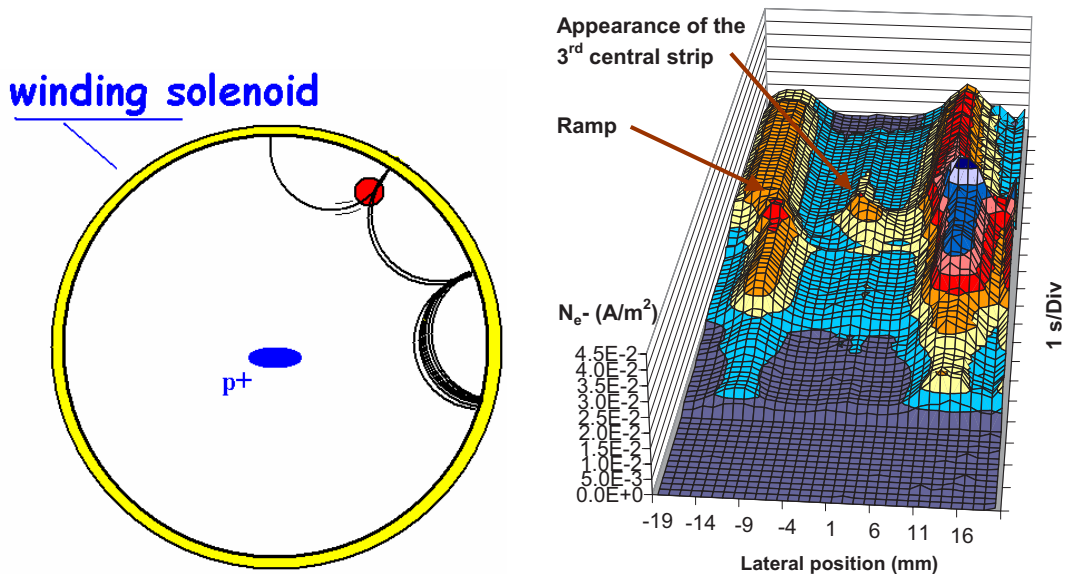
with the cross-section  $\sigma_{event}$  for the event of interest.  $L$  is the machine luminosity

$$L = \frac{N_b^2 n_b f_{rev} \gamma_r}{4\pi \epsilon_n \beta^*} F, \quad (6.2)$$

where  $N_b$  is the number of particles per bunch,  $n_b$  the number of bunches per beam,  $f_{rev}$  the revolution frequency,  $\gamma_r$  the relativistic gamma factor,  $\epsilon_n$  the normalized transverse beam emittance,  $\beta^*$  the beta function at the collision point and  $F$  the geometric luminosity factor due to the crossing angle at the interaction point. It is of interest to maximize  $L$  in order to study very rare events. As  $L \propto \frac{N_b^2 n_b}{\epsilon_n}$ , limitations in bunch population or bunch spacing as well as emittance growth directly affect the accelerator performance. In addition to that the EC can have other detrimental effects [29].

- Vacuum and beam lifetime degradation. The electrons impinging on the chamber wall cause a desorption of gas, which may affect beam life time by increasing the vacuum pressure.
- Heat load. The electrons get energy from the beam, which they eventually deposit on the chamber walls. At cryogenic temperatures, such as in the LHC cold arcs, this energy has to be evacuated at high cost. In addition to that the cooling capacity is limited.
- Collective instabilities such as transverse coupled-bunch instability and single-bunch instability lead to emittance blow-up, degrading the quality of the beam.
- Noise in beam diagnostics. On many occasions results from wire scanners, ion profile monitors, beam position monitors etc. have been found to be affected by the EC effect.

A possible remedy for EC not linked to the points mentioned above are solenoids, see Fig. 6.2(a). By winding a solenoid around the beam pipe, an azimuthal magnetic field can be created. This field keeps secondary electrons out of harm's way, that is, away from the beam. This solution is practicable e.g. in straight machine sections and has been applied in many synchrotron light sources, for example in Stanford's PEP2 (Positron Electron Project) or in ESRF (European Synchrotron Radiation Facility) in Grenoble. However, it appears out of question for arc sections with dipoles such as



(a) Solenoids: a possible cure for EC. The axial field keeps secondary electrons close to the chamber wall, avoiding detrimental effects on the beam (image courtesy M. Pivi).

(b) Measurements of the EC build-up in a mock-up of LHC beam screen at cryogenic temperature (courtesy M. Jimenez). Strips of high electron density were found to appear.

Figure 6.2:

the LHC cold arcs. It has to be added that dipoles cover the main percentage of the LHC ring; EC will form mainly there because of enhanced multipacting in the dipoles. In the next section the expected impact of the EC at LHC and possible remedies are discussed.

## 6.2 Electron cloud in the LHC

Rather early in the planning of LHC it was recognized that the EC effect might become an issue for this accelerator [35]. Since then numerous experimental and simulation studies on the EC were carried out. Simulations concentrated on the development of a code named ELOUD that models the generation of the primary electrons, the motion of the electrons in beam, EC and external magnetic fields and secondary electron generation [32]. The impact of the EC on collective effects and emittance was analyzed using the “HEADTAIL” code, another simulation tool developed at CERN [36]. The experimental work used the SPS as test bench for LHC beams. Simulation results were cross-checked and benchmarked against measurements. Furthermore, after validation of the simulation models in the SPS, predictions for the LHC are possible.

### Experimental studies

After first observations of the EC effect in the SPS by a pressure rise, many other experiments were performed in order to characterize the EC. Button type and strip-line pick-ups can be used to study the onset and the intensity of the EC. For heat load measurements, calorimeters were used. During several machine studies the influence

of the EC on the beam was investigated. In addition to that a cold strip detector was installed in the SPS to study EC effects under cryogenic conditions for LHC beams [34]. In this experiment, the vacuum pressure, heat load, electron current and the electrons' spatial and energy distribution could be measured under conditions similar to those expected in LHC. The results can be summarized as follows.

- In the dipoles, for increasing intensities vertical strips with high electron population form as shown in Fig. 6.2(b). These strips move in dependence of magnetic field and bunch intensity. Initially two strips appear symmetrically off-center; after the ramping, depending on the bunch intensity, a third one may appear in the center of the beam pipe.
- An analysis of the electron energy spectrum revealed distributions with maxima at about 80 eV in regions without magnetic field and 180 eV in dipoles.
- An EC build-up was found for bunch intensities above  $3 \cdot 10^{10}$  protons in dipoles with LHC beam with 25 ns bunch spacing.
- For bunch trains spaced by more 550 ns the build-up effect starts being decoupled, indicating that the residual electrons decay over this time scale.
- The beam pipe surface properties can be improved by so-called beam scrubbing. By this term accelerator operation with an artificially increased EC effect is understood. By the bombardment with electrons the beam pipe is “conditioned”, that is, its SEY is decreased. A couple of days of uninterrupted beam scrubbing should suffice to reduce the SEY to acceptable values in the SPS. In the LHC beam scrubbing is complicated by the fact that the maximum heat load in the cold arcs is very limited. Therefore, care has to be taken not to exceed the cooling capacity during beam scrubbing runs, when the EC effect is artificially enhanced.
- In the LHC a longer scrubbing time appears necessary, and the EC-induced heat load both during the beam conditioning and for operation at nominal intensity are still a major concern.

Changes in the bunch spacing have been discussed as possible remedies for the EC effect. It can be thought of doubling or tripling the bunch spacing and increasing the bunch population to keep luminosity constant. However, this introduces other limitations on the accelerator side. In addition to that it has to be kept in mind that the beams are collided to produce physics events. For nominal LHC beam (25 ns bunch spacing,  $1.1 \cdot 10^{11}$  protons per bunch) the high luminosity experiments ATLAS (A Toroidal LHC ApparatuS) and CMS (Compact Muon Solenoid) expect about 25 proton-proton interactions per bunch collision. This small number of interesting events is masked by a huge amount of elastic collisions and other events. The detectors are designed to cope with such an amount of data. However, when the bunch population is increased to compensate for larger bunch spacing, the so-called “event pile-up” gets problematic. This means that it gets increasingly difficult for the detectors to cope with the flood of data produced in each bunch collision. Another concept proposed to reduce the effect of EC are very long bunches (“superbunches”). Since EC build-up is driven by the attraction of electrons at the beginning of a bunch and by the ejection on the end, EC formation is mitigated by the use of long bunches; the electrons are trapped inside the

beam potential and the multipacting process does not start off. However, in this case the event pile-up appears to be even more critical.

### 6.3 Summary

The electron cloud is a beam-induced multipacting effect. Seed electrons already present in the beam pipe are accelerated by the beam potential. When they hit the wall, secondary electrons are freed. For a bunched beam, this may lead to the build-up of an electron cloud. In general, the presence of an electron cloud has detrimental effects on the beam quality. For this reason, a number of techniques are applied to measure the properties of the electron cloud in SPS, LHC and other accelerators and mitigate its impact. Following present estimations it appears that in LHC the electron cloud effect could limit the accelerator performance.

## Chapter 7

# SPS microwave transmission experiment

Various approaches have been pursued at CERN and elsewhere in order to measure the electron cloud effect in particle accelerators. Following suggestions by Noël Hilleret, microwave transmission measurements were carried out in the SPS during the 2003 and 2004 runs. A CW carrier above waveguide cut-off is transmitted through the beam pipe. An electron cloud present will interact with this electromagnetic wave, thereby revealing some of its properties. Compared to other methods, the potential advantages are threefold. First, the properties of the electron cloud are measured *in situ* in an existing accelerator beam pipe. Second, pretty large lengths can be covered and third, all this comes at relatively little cost. However, there is a price to pay. High beam-induced signals superimposed on the desired carrier have to be coped with. In addition to that, the overall situation is exceedingly complex due to the inhomogeneous magnetic fields and the time-invariant inhomogeneous electron plasma. Furthermore, the area in question is not easily accessible. When there was no beam for a longer period, e.g. at the end of the winter shut-down 2003/2004, the access to the tunnel was possible without major problems for several hours. However, small modifications to the set-up after the start of the 2004 run proved rather difficult due to the elevated radiation dose. All modifications were done during service times in the shadow of other higher priority interventions. For all the measurements no dedicated beam time was used. Rather, the complete program was run entirely parasitically, and a certain degree of flexibility was necessary working with beams tailored to fit the needs of other clients.

### 7.1 Concept

Microwaves transmitted in the beam pipe do not interact with the beam for several reasons. First, like in the case of plasmas, the protons are too heavy to move much at microwave frequencies. This effect is even stronger on account of the protons' relativistic speeds, which makes them stiffer. Furthermore, any interaction would have a very bad transit time factor due to the different velocities of beam and waveguide mode. The major part of any effect will thus average out over the lengths considered. With the beam dropping out, any measured effect has to be attributed to the electron cloud or other phenomena.

Conventional theories, simulations and measurements predict electron cloud densities of the order of  $\rho_e = 10^{12}$  per  $\text{m}^3$  for LHC beams [24]. These densities are similar to those found in the ionosphere [25], and the GPS frequencies are in the same range as the waveguide cut-off in the SPS. It is commonly known that the phase shift of electromagnetic waves in the ionosphere is one of the major limiting factors for the precision of GPS. The first SPS transmission experiments were inspired by this analogy. In the simple case of a thin unmagnetized plasma, the key parameter is the plasma frequency  $f_p = \frac{\omega_p}{2\pi}$ , given by

$$\omega_p = \sqrt{4\pi\rho_e r_e c^2} \quad (7.1)$$

with the classical electron radius  $r_e$  and the speed of light  $c$ . For  $\rho_e = 10^{12}$  per  $\text{m}^3$ , we get a plasma frequency of about 10 MHz. Since waveguide modes need to be used in order to cover the distances of interest, the operational frequencies have to be above 1 GHz. In this region, an unmagnetized plasma is transparent and causes a phase shift that is given for a length  $L$  by [38]

$$\Delta\phi = -\frac{1}{2} \frac{\omega_p^2}{\omega \cdot c} L. \quad (7.2)$$

Initially it was tried to maximize the expected phase shift by measuring over an SPS sector (about 1 km). However, already in measurements without beam an exceedingly high attenuation was found that can be attributed to the numerous cross-section changes that scatter the wave. Therefore, shorter sections of 30 and 7 m length were chosen.

### Modulation

The expected phase shifts for lengths of the order of 30 m are only about  $1^\circ$ , which cannot be easily measured. However, any beam-related amplitude or phase change is modulated with the SPS revolution frequency of 43.4 kHz, thus making highly sensitive sideband measurements possible. For  $L = 30$  m and  $f = 3$  GHz a phase change of  $0.6^\circ$  is found, corresponding to a modulation index  $\beta = 0.0105$  and a sideband amplitude  $\beta/2 = -46$  dB [26]. When the length is reduced to  $L = 7$  m, modulation sidebands  $-58$  dB below the carrier can be expected.

## 7.2 Measurement set-up

### 7.2.1 Machine lay-out

The measurements were carried out in SPS sector 251, at the downstream end of LSS2 (long straight section 2), which can be accessed from the surface building BA2. The machine layout of the SPS at the location of the experiment is depicted in Fig. 7.1. The set-up on the two measurement tracks is shown in Fig. 7.2. For all measurements, the signal was injected at the center pick-up and extracted at the two outer pick-ups. We refer to the combination of the down-going path, the propagation over *30 m of beam pipe* in the direction of the beam and up the surface as the *long track*, while the propagation over down-going path, *7 m of beam pipe* in the direction opposite to the beam and up is the *short track*. The long track is an arc section with four main bending magnets, a focusing quad, a sextupole and a correction dipole, while on the straight short track there are only one correction dipole and a skew quad.

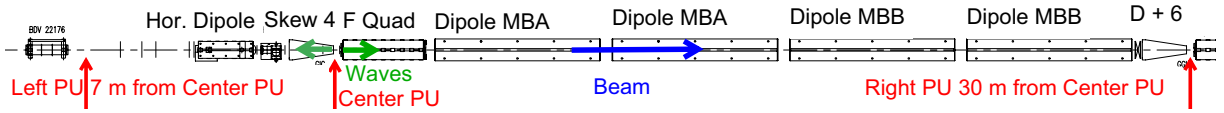


Figure 7.1: Layout of the SPS at the location of the experiment. “Hor. Dipole” designates a horizontal correction dipole, “Skew 4” a skew quadrupole, “F Quad” a focusing quadrupole and “D + 6” a horizontal dipole and a sextupole. The microwave signal was injected at the center pick-up (Center PU) and detected at the two outer pick-ups. The length of main bending dipoles and the focusing quad is 6.2 and 3.0 m, respectively.

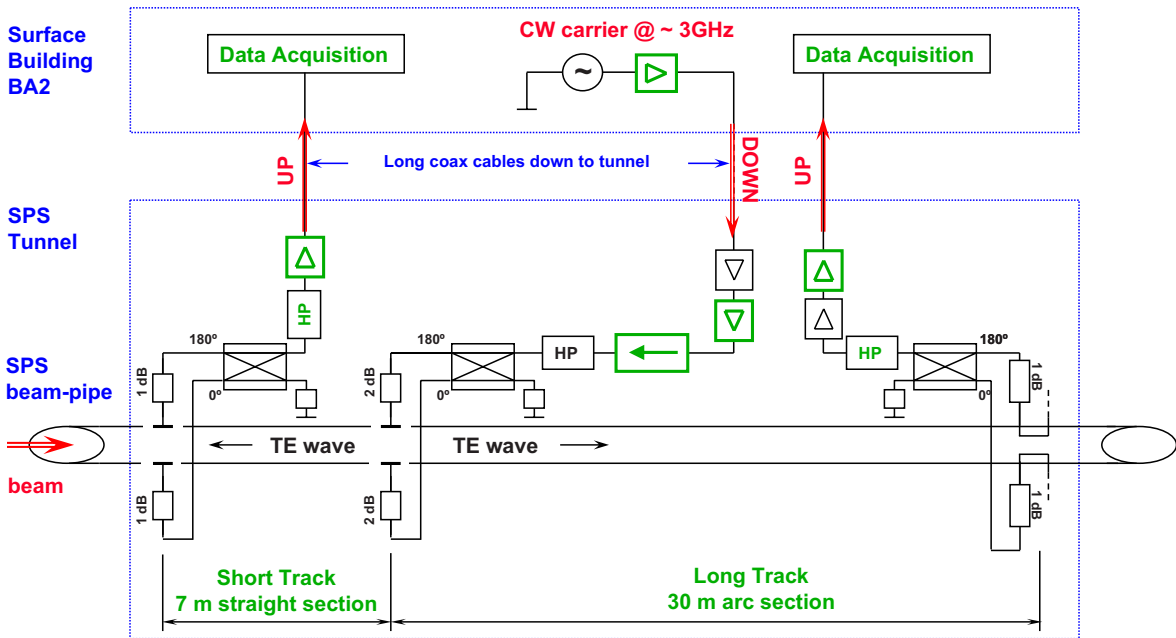


Figure 7.2: The set-up of the SPS microwave transmission measurement.

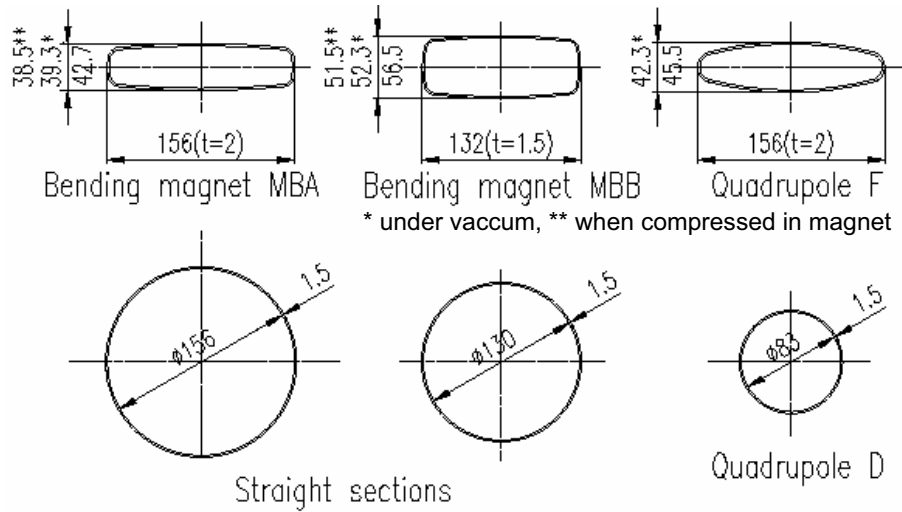


Figure 7.3: Vacuum chamber profiles in the SPS.

Pipe	TE <sub>10</sub>	TE <sub>30</sub>	TM <sub>11</sub>
Bending magnet MBA	1.0	3.0	4.5
Bending magnet MBB	1.2	3.5	3.3
Quadrupole F	1.2	3.5	3.3
∅ 156 mm Straight section	1.1	2.6	1.5

Table 7.1: Cut-off frequencies of the first modes on the SPS beam pipe in [GHz]. The bending magnet pipes were approximated by circumscribed rectangular waveguides, for the almost elliptic quad cross-section and the round pipe the cut-off frequencies of the corresponding modes on rectangular waveguides are listed.

The chamber cross-sections in the region of interest are shown in Fig. 7.3. On the long track, mainly flat type MBA and MBB bending magnet chambers are installed, while on the short track mainly the round 156 mm diameter straight section beam pipe is present. In the SPS, in general the beam pipes are made of stainless steel. The cut-off frequencies of the first waveguide modes on these pipes are listed in Tab. 7.1.

## 7.2.2 RF measurement equipment

### Down-going path

We will start the detailed description of the RF components used with the down-going path. On the surface, a CW signal in the range between 2 to 4 GHz, mostly 2.84 GHz, was produced using a signal generator. In some cases a power amplifier was used thereafter to boost the signal level up to 30 dBm. Then the signal runs down to the tunnel over a  $\approx 250$  m long 7/8 inch 50  $\Omega$  beam diagnostics cable that was not in use and could be borrowed. The one-way cable attenuation determined by time domain reflectometry was found to be 42 dB at 2.5 GHz, 45.6 dB at 2.84 GHz and 47.5 dB at 3 GHz. Once in the tunnel, the signal is amplified by about 65 dB in two-stage amplifier chain, composed of an Avantek AMG-4051M901 and a Mini-Circuits ZHL-24 amplifier. The frequency response as well as the power characteristics of these amplifiers

are plotted in Fig. 7.4.

As can be seen from Fig. 7.4(f), the 1 dB compression point of the entire amplifier chain is at about  $P_{in} = -37$  dBm. With a line attenuation of 46 dB at 2.84 GHz the CW power at the surface should be kept below 10 dB in order not to drive the amplifier chain in the down-going path into saturation.

After the amplifiers, an isolator (Melabs RS-9) and a high pass filter was inserted in order to protect the amplifiers against beam-induced signals. Fig. 7.5 depicts the characteristics of these components. The isolator suppresses the beam signals by 30 dB in the working frequency range, however, it has little or no effect at frequencies below 1 GHz. To avoid beam signal below 2 GHz, a waveguide filter was installed. It simply consists of two S-band coax-to-waveguide adapters connected. Unfortunately at the time of installation it was not deemed necessary to measure the filter's transfer function, and so it only turned out later that due to the short waveguide length the low-frequency suppression is no more than about 40 dB. This is not entirely satisfying since the beam spectrum is stronger at lower frequencies.

Finally, the signal goes to the delta port of a 2 to 4 GHz  $180^\circ$  hybrid where it is split in two signals of equal amplitude and opposite phase. These signals are then used to feed the two buttons of a custom wide-band pick-up.

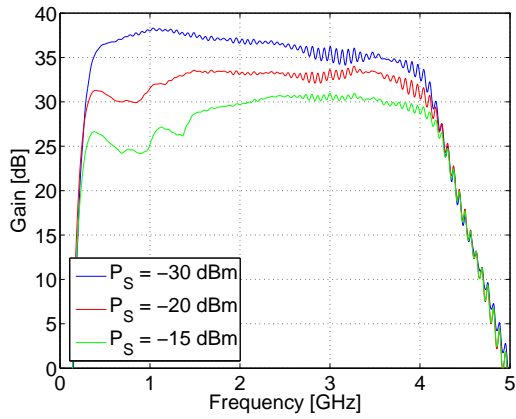
The fact that two buttons are excited in opposite phase ensures the excitation of modes with a transverse electric field. In the flat beam pipe of the center pick-up (PU), only the  $TE_{10}$  and the  $TE_{20}$  can propagate below 3 GHz. Therefore, since the buttons are installed in the center of the beam pipe, only the  $TE_{10}$  mode will be excited. Above 3 GHz the  $TE_{30}$  will be present, as well. Measurements and simulations showed that the coupling is not very high for this type of structure. In the flat beam pipe cross-section the center PU has a  $TE_{10}$  mode  $S_{21} \approx -13$  dB between 2 and 3 GHz. For the  $TE_{30}$  the coupling is a bit better, of the order of  $-7$  dB above 3.3 GHz.

It is known that in beam pipes electrically isolated objects tend to charge. The buttons used are not grounded DC-wise, since the hybrid does not work at low frequencies. In order to prevent a static charge-up of the buttons, small attenuators directly connected to the buttons were used as DC returns.

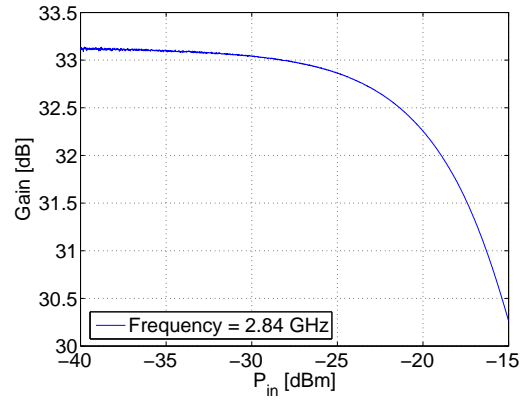
### Left up-going path

At 7 m distance upstream from the center PU another button type pick-up was installed before the 2004 run. In this straight section the beam pipe is circular with an inner diameter of 156 mm. Due to the bigger diameter, the coupling to the fundamental  $TE_{11}$  mode is still smaller than in the center PU, of the order of  $-20$  dB. A multitude of other modes, especially the  $TM_{11}$  mode (cut-off  $f_c = 2.34$  GHz), the  $TE_{31}$  ( $f_c = 2.57$  GHz), the  $TM_{31}$  ( $f_c = 3.90$  GHz) and the  $TE_{51}$  ( $f_c = 3.93$  GHz) are also excited at higher frequencies.

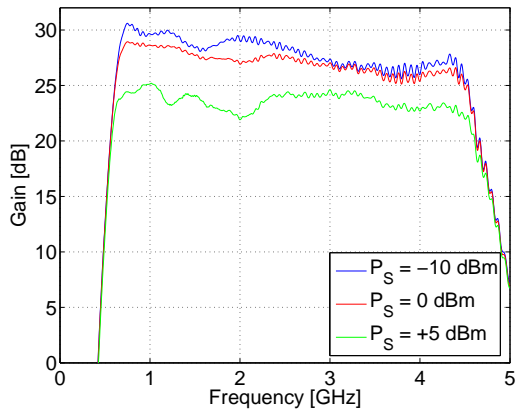
Coming from the PU, after going through 1 dB attenuators acting as DC returns, the signals are combined with  $180^\circ$  phase shift in a 3 dB hybrid. Thereafter, a relatively narrow band pass (Fig. 7.6(a), red curve) is used to limit the beam-induced background signal. A short coaxial cable (about 10 m) then runs back to the extremities of the long cables to the surface. Before going there the signal is boosted with a Mini-Circuits amplifier (Fig. 7.4(c)). The same type of cable as for the center PU with an attenuation of about 43.5, 47.3 and 49.2 dB at 2.5, 2.84 and 3.0 GHz was used.



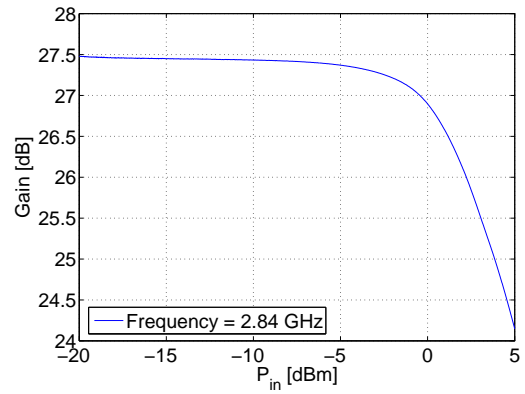
(a) Frequency response of the Avantek amplifier.



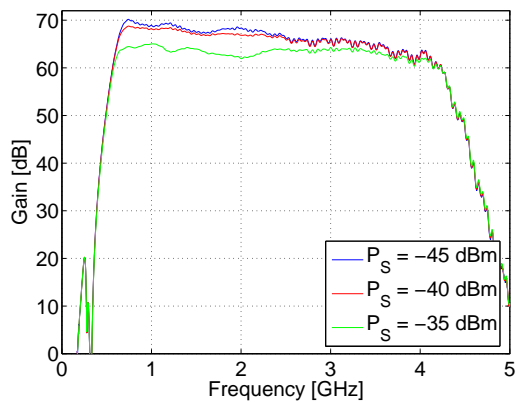
(b) Gain compression of the Avantek amplifier.



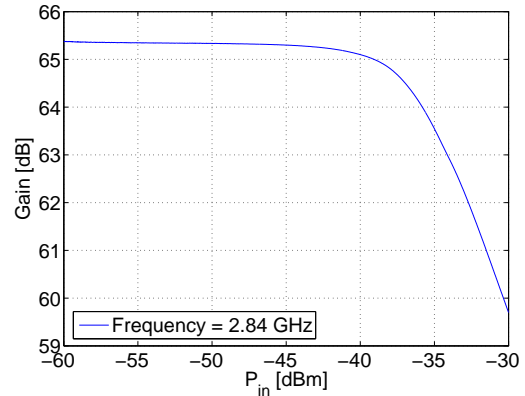
(c) Frequency response of the Minicircuits amplifier.



(d) Gain compression of the Minicircuits amplifier.



(e) Frequency response of the amplifier chain.



(f) Gain compression of the amplifier chain.

Figure 7.4: Characteristics of the Avantek AMG-4051M901 amplifier (a, b), sketched in thin black lines in Fig. 7.2, the Mini-Circuits ZHL-24 amplifier (c, d), sketched in thick green lines and the entire chain composed of the two in series (e, f).

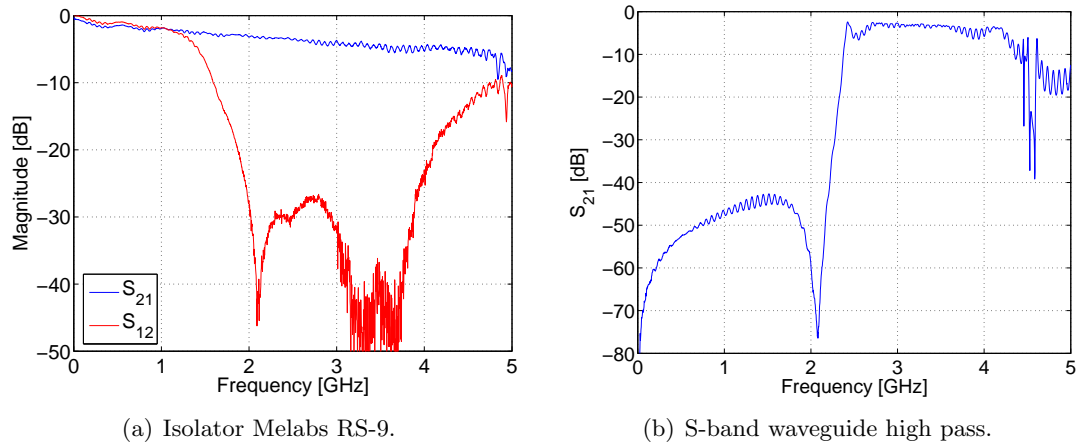


Figure 7.5: Characteristics of the isolator and waveguide filter employed to protect the amplifiers in the down-going path from beam-induced signals.

### Right up-going path

30 m downstream of the center PU, the upstream end of a stripline PU was borrowed for our experiment. This pick-up consists of two axis strips centered on the top and the bottom of the beam pipe. Unfortunately the characteristics of the PU in our frequency range are not known precisely. Again, small attenuators were used as DC returns and the difference between the signal from the top and bottom PU plate was generated in a hybrid. An S-band waveguide high pass filter with cut-off at 2 GHz was connected thereafter to limit the beam-induced signals. After recognizing that there might be an appreciable transmission through the filter by evanescent modes, the length of the waveguide was increased, leading to a satisfyingly large signal suppression below 2 GHz, see Fig. 7.6(a). The signal is then amplified by an Avantek amplifier (Fig. 7.4(c)) and transmitted back to the location of the center PU over a 50 m long coaxial cable. With a measured cable attenuation of 0.52 dB/m this makes a drop of 26 dB. Before going on the long cable to the surface the signal is again amplified with a Mini-Circuits amplifier (Fig. 7.4(c)). This cable is very similar to the one for the left up-going path with an attenuation of 44.0, 47.8 and 49.4 dB at 2.5, 2.84 and 3.0 GHz, respectively.

### Hardware transfer function

The transmission measurement over the entire signal path without beam nor magnetic field is called hardware transfer function (HTF). The determination of the HTF was among the first things done, since it shows at which frequencies transmission is possible. As can be seen in Fig. 7.6(b), the filters in the up- and down-going paths dominate the HTF. The ripple of the HTF in the filter pass-band is due to the frequency-dependent coupling of the buttons and the reflections from the cross-section changes of the beam pipe. For both the short and the long track regions of good transmission are found around 2.84 GHz. For practical reasons, since the excitation and the data acquisition are done with the same set-up for both tracks, this frequency was used in most of the measurements. A couple of measurements at 2.467, 3.00, 3.25 and 3.70 GHz were carried out as well, most of them on the long track during the 2003 run [33].

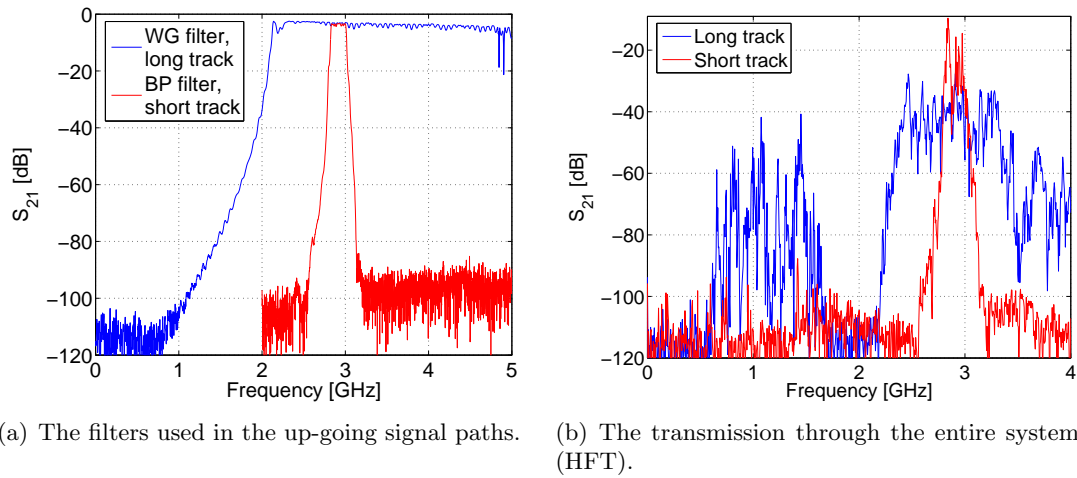


Figure 7.6: Filters used in the microwave transmission experiment and the hardware transfer function.

On the right track a considerable transmission was also found between 600 and 1700 MHz, which is probably due to the low signal rejection by the waveguide filter in the down-going path. However, the magnitude of the transmission in that region is not yet fully understood.

### Change of the HFT with magnetic field

Besides the hardware transfer function, the impact of the magnetic field alone on the microwave transmission was determined. To this end, the transmission at several frequencies was measured with the magnetic field varied. These measurements were not easy to carry out without dedicated machine time, since during normal machine operation there is beam and when the machine is halted for access, the magnets must not be operated for safety reasons. However, during the start-up of operation with beam, there is a small time window when only the magnets are ramped in preparation for injection. Fig. 7.7 shows the change of transmission when the magnetic field is ramped. In the bending magnets, the field goes from 0.117 T to 2.025 T during the ramp. The measured  $S_{21}$  was found to decrease for higher magnetic field. This small effect could be due to the small permeability of the austenitic stainless steel or thin ferromagnetic coatings on pumping ports. However, the changes in  $S_{21}$  are small and occur on a very long time scale compared to the SPS revolution period. Therefore, it can be easily separated from beam-related effects. On the long track, much higher variations of  $S_{21}$  were found e.g. at  $f_{carrier} = 2.5$  GHz, and for this reason this frequency was avoided in further transmission measurements.

### 7.2.3 Testing of the measurement set-up

In the present measurement we are trying to detect small signals in a very noisy environment. In particular the strong superimposed beam-induced signals pose quite a challenge. This is why cross-talk, electromagnetic interference, saturation and inter-modulation effects have to be checked carefully.

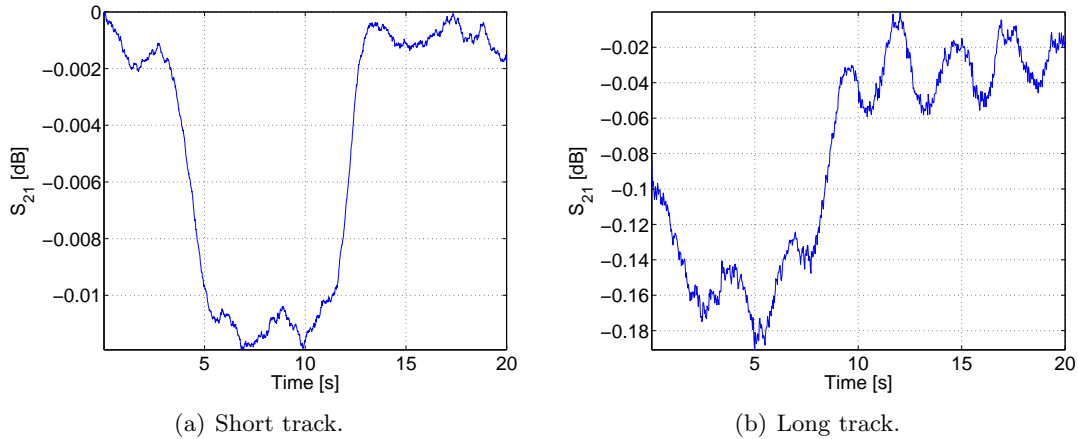


Figure 7.7: Change of transmission through the beam pipe for a varying magnetic field,  $f_{carrier} = 2.84$  GHz, Supercycle 950 for LHC beams. High transmission corresponds to low magnetic field. Traces smoothed over 5 % of the frequency span.

### Cross-talk

In the tunnel, at the extremity of the long cables coming down from the surface, there is the maximum signal level difference between the signal paths. The power amplifier provides up to 30 dBm output power, while the wanted PU signal is 40 to 60 dB lower. Type N or SMA screw-lock connectors were used without exception to eliminate cross-talk. As a check, the transmission between the long cables with terminations on the far ends was measured. The cross-talk was found to be negligible.

### Beam signals incident on the end stage of the power amplifier

In the down-going path, even though a high pass filter as well as an isolator were inserted, some fraction of the beam signals will still get through to the end stage of the Mini-Circuits power amplifier. The combined signal rejection of the the isolator and the high pass is not much higher than 40 dB. In particular at frequencies below 2 GHz, where the beam spectral density is still pretty high, it can be expected that significant beam power gets through. Therefore it was tested in the lab how the amplifier reacts on power incident on its final stage. For a rather strong parasitic signal of +10 dBm CW at 1 GHz, a slight decrease in gain was found ( $\approx 0.2$  dB).

### Saturation and intermodulation

Amplifier saturation due to the CW carrier used for the measurements can be avoided easily. To that end, the 1 dB compression point of the amplifier was determined and the source power set accordingly. However, on the up-going paths the situation is more difficult, since they cannot be protected from beam-induced signals by isolators. In-band beam signals will thus go through the amplifiers, eventually causing gain compression and intermodulation with the wanted CW carrier signal. In order to quantify these effects, a quick lab experiment was set up.

The Mini-Circuits ZHL-24 amplifier was driven with a 2.84 GHz CW signal at +10 dBm, its specified maximum input level. Another signal at 1 GHz with a level of 3

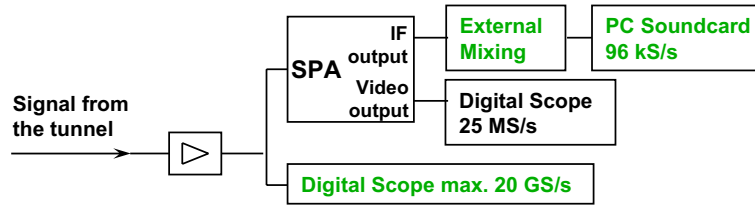


Figure 7.8: The data acquisition systems used. In addition to direct detection with a fast scope, downconversion using a spectrum analyser (SPA) was applied.

dBm, 100 % amplitude modulated at the SPS revolution frequency was superimposed. This latter signal represents the parasitic beam signal. In the presence of the parasitic signal a gain compression of 0.3 dB was found. For higher parasitic signal levels, higher gain compressions up to 3 dB were found. Still larger gain drops are probably possible but could not be obtained in this kind of non-destructive tests. Even when the parasitic signal is very low (-30 dB), a small gain compression can be observed due the small non-linearity of the amplifier.

### Recovery time after severe saturation

For short time intervals, amplifiers can stand high powers that would be destructive if applied continuously. The beam signal contains many sharp transients, e.g. from each bunch or from entire batches. For some beams, tails with decay times of the order of 1  $\mu$ s have been observed after the passage of the beam. It can be imagined that amplifier saturation is responsible for this effect. In order to check this the amplifier was driven with 1 ns long pulses simulating the beam. Recovery times of the order of 1 ns were observed.

## 7.3 Data acquisition

After the 2003 run, the data acquisition techniques were considerably improved [43]. At the end of the 2004 run four different systems were in use. The first two are the most basic techniques, given that the appropriate equipment is available but they suffer from a certain number of limitations. The two latter techniques are more powerful but of course also more complex and critical. The schematic of the four approaches is shown in Fig. 7.8. In some cases, especially the measurements with the spectrum analyser (SPA), a preamplifier was used as sketched in the figure.

- **Direct observation in time domain on a fast scope.** A fast scope was used for direct observation of the signal coming from the tunnel. This is certainly the most straight-forward way but it suffers from the inconvenience of a very limited observation time (max. 400  $\mu$ s) and produces huge amounts of data to transfer and process (about 50 MB for one 400  $\mu$ s trace). For these reasons it was only used casually, in particular to cross-check with other methods.
- **Direct observation in frequency domain on a spectrum analyser.** This second method is also very basic and easy to use. It has one fundamental draw-

back, which is the limited sweep time. When high dynamic range is required, a low intermediate frequency filter (IF) bandwidth is necessary in order to reduce noise. This slows down the sweep time, making measurements in dynamic situations, for example ordinary machine cycles difficult. However, good results were obtained during the injection flat top and for stored beams.

- **Downconversion with a spectrum analyser and observation of the SPA video output in time domain.** In order to observe the transmission of the CW carrier signal over longer periods of time ranging from several turns (100  $\mu$ s) to a machine cycle (roughly 10 s), the SPA was centered on the carrier and run in zero span mode with a big IF bandwidth, typically 3 to 5 MHz. In principle, the time domain signal is then displayed on the screen. However, since initially an analog device was used, the time domain signal had to be taken from the external video output and plotted on a digital scope to be able to record the data. Later this technique still proved valuable since the maximum trace length available on the scope was far larger than on the SPA, making longer records possible. Here, the rise time of the system is limited by the SPA IF bandwidth, giving about  $\Delta t \approx \frac{1}{3B} \approx 100$  ns for an IF bandwidth of  $B = 3$  MHz. The maximum trace length with sufficiently high sampling rate on the scope (25 MS/s) is of the order of 100 ms.

- **Downconversion with a spectrum analyser, external mixing and base band data acquisition on a PC sound card.** Instead of looking at the video output of the SPA, the IF output was used here. The IF signal, centered at 21.4 MHz for most spectrum analysers, was then mixed externally to base band, where the signal was sampled and acquired using a commercial PC sound card. Even though this approach was the most complicated of all, it could well be the method of choice. The PC sound card offers numerous advantages. It is pretty cheap (about 100 EUR), has a very high dynamic range (up to 120 dB), programming and data transfer to a PC are rather easy and very long traces (several minutes) can be recorded and processed. One major limitation, however, is the sampling frequency of  $f_s = 96$  kHz. In audio applications this may be amply sufficient even for the most brilliant ear but in our case it is not. With the SPS revolution frequency of  $f_{rev} = 43.4$  kHz, only to cover the first two sidebands of a modulation spectrum requires a bandwidth of at least 87 kHz. Due to aliasing, the maximum bandwidth of the sound card is limited to 48 kHz. However, this limitation could be worked around.

It is always possible to observe one single sideband by choosing the appropriate local oscillator (LO) frequency in the external mixing. Tracking a single sideband over time for itself is interesting, however much more information can be obtained from observing both sidebands *simultaneously*. This was accomplished by moving the LO close to the carrier (Fig. 7.9), to within a frequency  $f_0$ . Doing this, one sideband is transposed to  $f_{rev} + f_0$  while the other goes to  $f_{rev} - f_0$ . If  $f_0$  is sufficiently low ( $f_0 \lesssim 4$  kHz), both sidebands will fall below  $f_s/2$  and can thus be detected without problems. In practice, since we are already close to  $f_s$ , frequency offsets  $f_0$  of the order of 100 Hz were used. Attention has to be paid not to go too low in  $f_0$ , since the (strong) carrier is transposed to that frequency. Since the

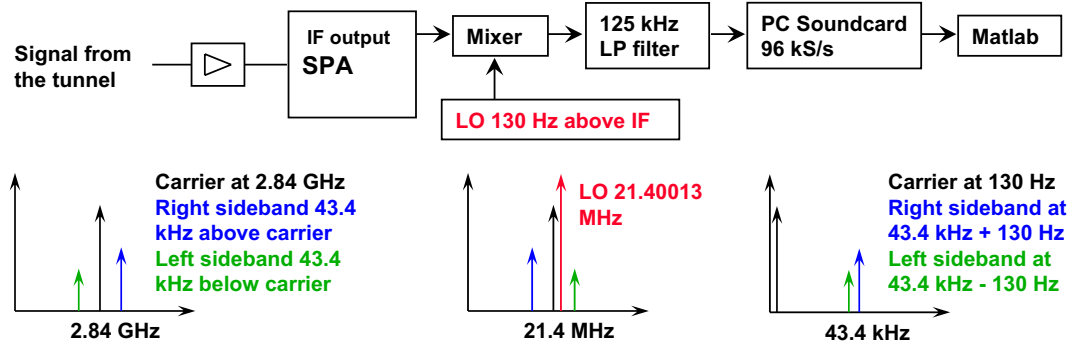


Figure 7.9: Set-up for the data acquisition with the sound card. By choosing the LO frequency close to the carrier, the spectrum is folded and both the upper and lower modulation sidebands fall in the detection range of the sound card.

sound card has a low frequency limitation of about 20 Hz, the strong carrier can be unduly distorted. In addition to that, a too small sideband spacing can make it difficult to measure the exact level of each sideband.

The data transfer and processing was implemented in a Matlab application. In the first mode of operation, the FFT spectrum is plotted in real time. Second, if necessary, a given set of data can be buffered and the spectrogram calculated. In principle, the system at hand works like a dynamic signal analyser, which is also commercially available. The question why such device was not used can be easily answered. In fact, an available base band dynamic signal analyser was tested (Stanford Research Systems SR785), but the results were not satisfying at all. Data transfer turned out to be very awkward and continuous time domain data (several traces in a row) could not be treated at all. However, recently fully featured RF dynamic signal analysers came on the market but such an instrument was not available. It remains a question whether the exceptionally high dynamic range of the sound card system (in excess of 100 dB) can be matched by an affordable commercial system.

## 7.4 Results

In the data taken during the 2003 and 2004 runs, phenomena were found that can be grouped in five categories. Most interesting is that a strong attenuation was found when the beam passes. The effect was observed both in time domain and in frequency domain, where the attenuation shows up as an AM spectrum.

### 7.4.1 Beams and Machine Parameters

Data was taken for a multitude of difference beams including

- SFT Pro beam (Physics beam in the SPS)
- LHC beam
- Single bunches

Beam parameters	nominal LHC	Pilot beam	SFT Pro 950
Proton momentum [GeV/c]	26 / 450	26 / 450	14 / 400
Number of bunches/PS batch	72	1	2100
Number of PS batches/SPS batch	2-4	1	1
Number of particles per bunch [ $10^{11}$ ]	1.3 / 1.15	0.055 / 0.05	0.06 – 0.1
Circulating beam current at inj. [A]	0.13 – 0.26	$3.9 \cdot 10^{-5}$	0.18 – 0.29
Bunch spacing [ns]	24.97 / 24.95		5
Bunch train spacing [ns]	224.7 / 224.6		1050
Longitudinal emittance [eV.s]	0.35 / <0.8	0.35 / <0.8	0.2 / 0.6
Rms. bunch length [cm]	30 / <15	30 / <15	135 / 51
Rms. energy spread [ $10^{-4}$ ]	10.7 / <2.8	10.7 / <2.8	20 / 60

Table 7.2: Beam parameters in the SPS. First values in each field are at injection, second values at extraction.

- Stored LHC and single bunch beams
- Ion beams
- Other customary machine development (MD) beams.

The beam parameters for the nominal LHC beam, the pilot beam and the SFT Pro beam are summarized in Table 7.2 [3].

The SFT (SPS Fixed Target) type beams are production beams, i.e. they go to fixed target physics experiments. In 2003 and 2004, most of the time the SPS ran on such beams. With two injections of debunched beam from the PS (Proton Synchrotron), the SPS is completely filled apart from the two kicker gaps. After the injection the beam is bunched and accelerated to 400 GeV. This machine cycle is depicted in Fig. 7.10. The acceleration increases the momentum of the particles, implying that the magnetic field needs to be ramped, as well, to keep the beam in orbit. Thereafter, the beam is sent to the users by slow extraction, as can be seen from the slowly decreasing intensity.

On the other hand, the LHC beam comes from the PS as a bunched beam, is captured in the SPS, accelerated to top energy and then ejected within one single turn to go to the LHC (7.10(b)).

Different types of single bunch beams are used mainly for machine development and evaluation purposes. Due to the reduced intensity single bunch beams are less critical to handle compared to other beams. In the commissioning phase of LHC, the so-called pilot beam will be extensively used. This is a single bunch with a low intensity of only  $5 \cdot 10^9$  protons.

#### 7.4.2 Attenuation with beam

For all beams and most carrier frequencies used, an attenuation of the CW signal was found during the passage of the beam. This attenuation was observed in several ways.

##### Attenuation in time domain

For the observation of the attenuation in time domain, the video output of the SPA was plotted on a scope as described in the previous chapter and illustrated in the center

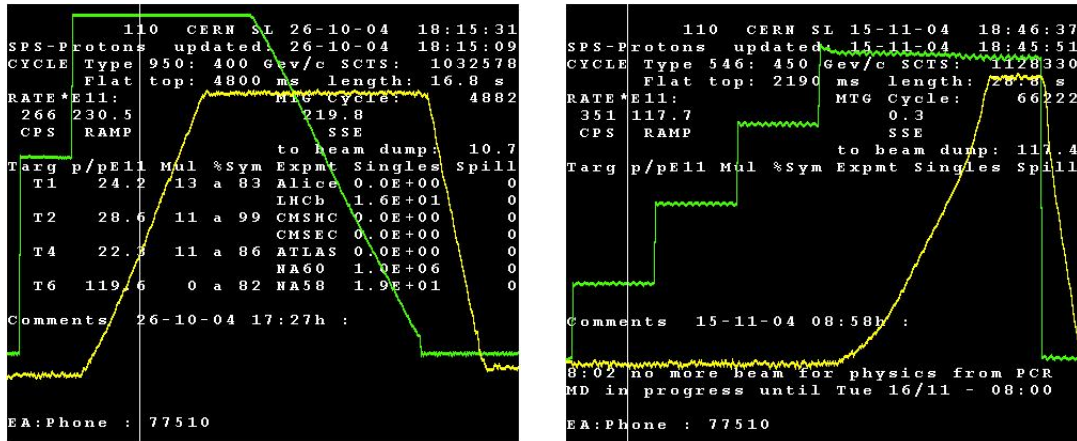
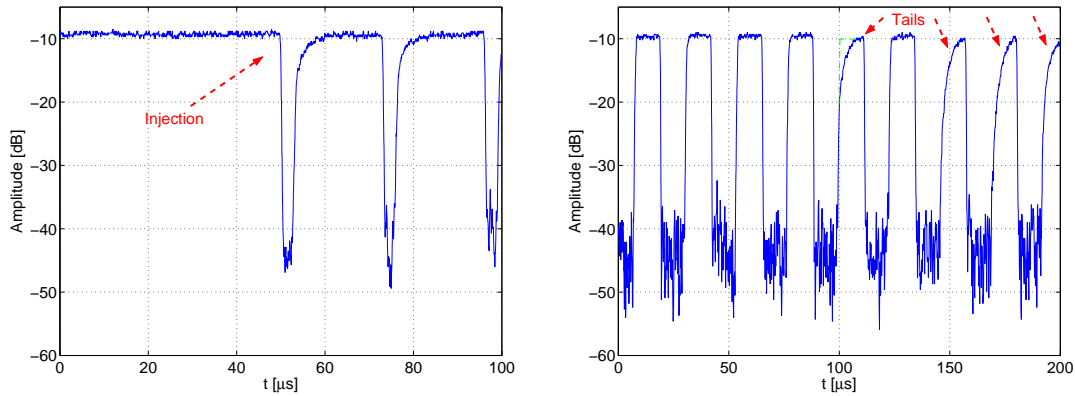


Figure 7.10: SPS machine cycle for two different beams. The beam intensity is plotted in green, the magnetic field strength in the bending magnets in yellow. These images are the typical way beam parameters are displayed at CERN. The data in the background is of no special interest here, so please ignore it.

branch in Fig. 7.8. A measurement for a 2.84 GHz carrier is shown in Fig. 7.11(a). The data acquisition was triggered upon injection of the beam in the SPS. Before injection the transmitted signal has a relative level given by the hardware transfer function at the particular frequency. The fact that the HTF is influenced to a small degree by the magnetic field will be neglected, since we are looking at much smaller time scales than the machine cycle length. At  $t = 50 \mu\text{s}$  the first batch is injected in the SPS. The transmission of the microwave decreases by at least 30 dB. After the passage of the beam, the signal returns to its initial level almost immediately. This process repeats with every turn of the batch, every  $1/f_{rev} \approx 23 \mu\text{s}$ .

The exact amount of attenuation with beam is hard to determine for “strong” beams, since the carrier goes below the noise floor, which is given mainly by the SPA noise figure. The present set-up was used with many measurement and beam parameters varied, in particular

- Beam type. For all the beams observed attenuation was found.
- Beam intensity. In general, higher beam intensities were related to higher attenuation. Nominal LHC beams caused attenuations of at least 30 dB on the long track, while single bunch beams were hardly visible at all in time domain or caused attenuations in the range of fractions of a dB, depending on bunch intensity.
- CW carrier frequencies. At all CW frequencies used, namely 2.467, 2.84, 3.0, 3.25, and 3.7 GHz, some beam-induced attenuation could be observed.
- Vacuum pressure variations in the range between  $3 \cdot 10^{-8}$  and  $1.3 \cdot 10^{-7}$  Torr did not change the known behaviour.



(a) Injection of an LHC type beam. Before injection the transmitted signal is high, after the subsequent beam passages it returns to its initial value.

(b) Tails on a fixed target beam. For some beams, the transmitted signal was found not to return immediately to its initial level.

Figure 7.11: Attenuation of a CW microwave signal transmitted through the beam pipe.

- Long or short track. On the long track, in general, the observed attenuation was much higher. However, it has to be kept in mind that the length is not the only difference between the short and the long track. On the long track there are main bending magnets, while the short track is straight. The observed effect could thus also be attributed to the longer sections with magnets on the long track.

### Tails

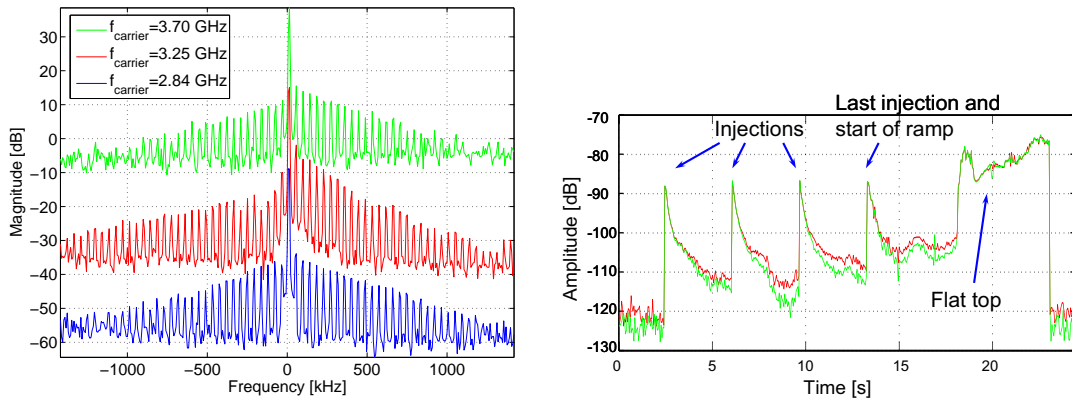
As can be seen in Fig. 7.11(b), the attenuation after the passage of the beam does not always go back to zero within the system rise time of about 100 ns. Sometimes it takes longer and so-called “tails” with rise-times of the order of 1  $\mu$ s appear. These tails mostly come in groups but their appearance does not seem to obey any periodicity. They are more pronounced for “strong” beams such as LHC beams.

### Asymmetric spectrum at cyclotron resonance

When the cyclotron resonance condition for electrons (charge  $e$ , mass  $m$ )

$$\omega = \frac{eB_0}{m} \quad (7.3)$$

is fulfilled in the main bending magnets at the SPS injection flat bottom ( $f_{carrier} \approx 3.25$  GHz for  $B_0 = 0.117$  T, when the beam is injected into the SPS), a visibly asymmetric modulation spectrum can be found (Fig. 7.12(a)). At lower frequencies, e.g. at 2.84 GHz, the spectrum is rather symmetric, meaning that we have either predominantly AM or PM. Now it cannot be told by from the spectrum itself whether it is AM or PM. However, from the time domain observation we know that there are drops in amplitude, so the spectrum at 2.84 GHz must be mainly AM. At the cyclotron frequency on the other hand, we have an additional PM that happens to be roughly as strong as the AM. At still higher frequencies the spectrum is slightly asymmetric.



(a) Modulation spectrum in the region of the electron cyclotron resonance at the injection flat bottom ( $f_{res} \approx 3.25$  GHz). Spectra stacked vertically for clarity.

(b) The two first modulation sidebands tracked over an LHC beam cycle in the SPS. Equal sidebands correspond to mainly AM, different sidebands to a superposition of AM and PM.

Figure 7.12:

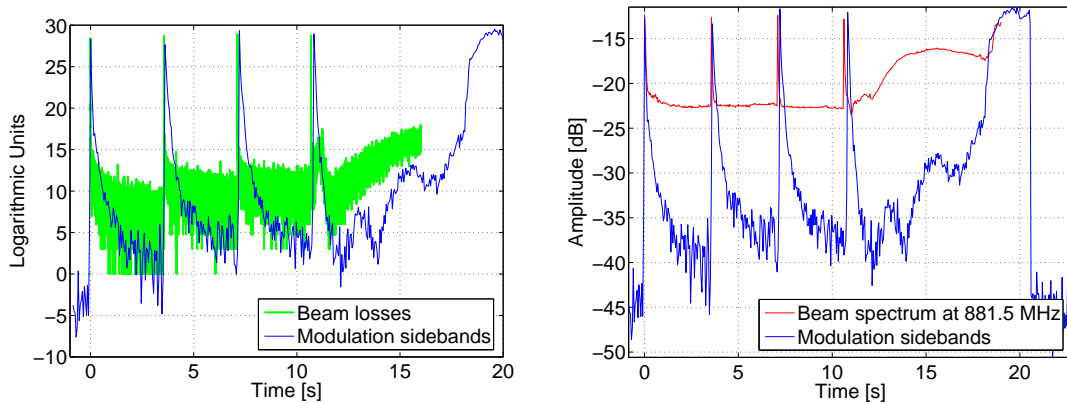
### Strong absorption peaks and periodicities after each injection

By means downconversion to base band and data acquisition with the soundcard, the first modulation sidebands were tracked over entire machine cycles. A large part of the modulation spectrum is lost this way but the most important information still remains. The symmetry of the spectrum can be observed and evaluated, as well as the height of the sideband relative to the carrier.

Measurements with many beams revealed sidebands between 30 to 90 dB below the carrier, in agreement with the spectra taken directly with the spectrum analyser. However, this kind of data acquisition is much more powerful, since the variations of the sidebands with time can be tracked accurately. A typical result of an LHC beam is shown in Fig. 7.12(b). The vertical axis has a logarithmic scale with an arbitrary reference level. Please compare this with the machine cycle in Fig. 7.10(b). When there is no beam in the SPS, no modulation sidebands are detected and we can see the noise floor at  $-120$  dB. The first injection then shows up as a strong peak going to more than  $-90$  dB. In the period before the second injection, the sidebands decrease by about 20 dB before peaking again at the second injection and so on. After the fourth injection, the beam is accelerated and kept for a few seconds in the machine on the flat top, where again we see strong sidebands. Finally, when the beam is dumped, the sidebands vanish. In the region where the sidebands are high, they appear to have almost equal height, while for smaller sidebands some asymmetry was found, implying that there is some superimposed PM. Similar patterns were found for all beams but with varying sideband height and asymmetry.

As a cross-check, the sideband signals have been correlated with a number of other accelerator parameters. They show some correlation with the beam losses over time (Fig. 7.13(a)). However, the beam losses decrease by 10 dB within about 10 ms after injection, whereas the beam sidebands take about 200 ms for an equal drop.

A stronger correlation was found between the modulation sidebands and the beam spectrum (Fig. 7.13(b)). Measurements of the beam spectrum at its harmonics below 1 GHz were available (courtesy T. Bohl). In the range of 400 to 1000 MHz, the beam



(a) Modulation sidebands versus beam losses for an LHC beam and the short track. The beam losses decrease much faster after each injection than the modulation sidebands.

(b) Modulation sidebands at 2.84 GHz versus beam harmonics at 881.5 MHz.

Figure 7.13: Correlation of the modulation sidebands with beam losses and the beam spectrum during a machine cycle with LHC beam. The latter effect happens in the same time scale as the modulation sidebands.

harmonics have in principle the same behaviour, even though the peaks at injection get higher for higher beam harmonics. The decay time of these injection peaks in the beam spectrum does not vary much for different frequencies. In the case depicted in the plot, beam spectrum decays about twice as fast as the modulation sidebands after each injection. About the same time step has been used for both traces ( $\approx 50$  ms) to avoid problems related to undersampling. The fact that the sidebands develop similarly as the beam spectrum density suggests that intermodulation with the beam-induced signal in the amplifiers has a significant impact on the measurement.

Another interesting phenomenon turned up in the detailed structure of the sideband peaks just after injection. Data from the SPA video output show repetitive structures with a period between 1 to 2 ms (Fig. 7.14(a)). This periodicity is strongest within the first 100 to 200 ms, when we also see the sideband peaks mentioned before. Zooming in more, a 3-turn periodicity ( $\approx 70$   $\mu$ s) could be resolved. This effect was correlated with many machine parameters trying to understand where it comes from. The most likely candidate now appears to be the vertical fractional tune, which is close to 0.16. Since the pick-ups are installed in the vertical plane, the beam will be close to one pick-up plate every  $1/0.16 \approx 6$  turns. Therefore the beam-induced signals as well as other beam-related effects will get stronger every 3 turns. This means that the amplifiers will get driven closer towards saturation every third turn, which can explain the observed pattern.

Coming to the longer 2 ms periodicity, this is simply due to the beating of the tune and the revolution frequency.

### Stored beams

For many reasons, stored beams are an interesting case to study in accelerator physics. In the SPS, beams are stored for minutes to hours during machine development sessions.

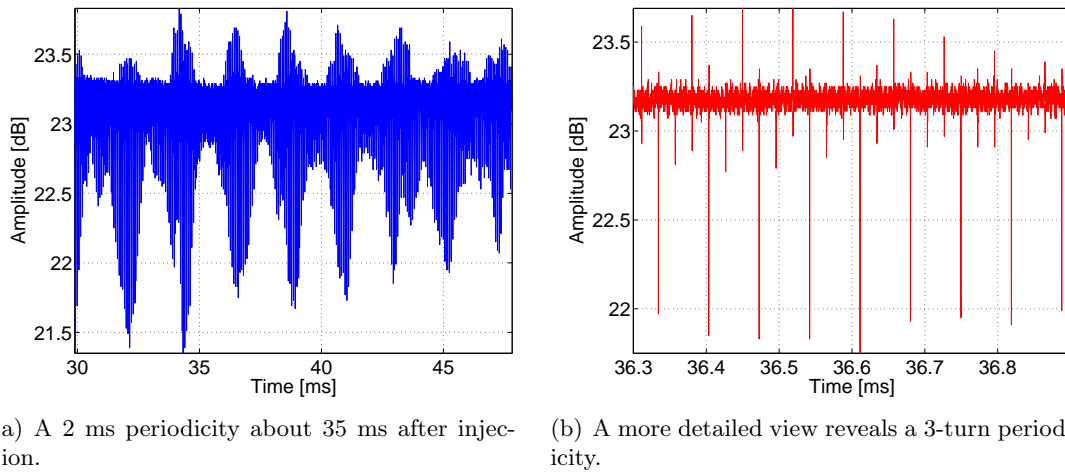


Figure 7.14: Repetitive structures found in the absorption signal shortly after injection of a single bunch beam with  $0.4 \cdot 10^{-11}$  protons per bunch, short track.

Such rather long times allow to play with many parameters and get easily comparable results, since the intensity decreases relatively slowly, e.g. by 50 % over 10 minutes as in the case that will be discussed next. Fig. 7.15 depicts the modulation sidebands' evolution on the short track over the first 200 s of a stored LHC beam.

In the top plot, within the first 10 s two strong peaks can be seen which stem from the injections. Then the sidebands decrease unsteadily until about 120 s after the start, when they level out. The noise level is still about 10 dB lower than the side bands after 120 s, as can be seen from the spectrogram in the lower plot in Fig. 7.15. The sidebands' amplitudes for the top plot were extracted by finding the maximum values of the spectrogram in the regions limited by the dashed red and green lines for the lower and upper sidebands.

The reader will notice another two horizontal lines about 10 Hz above the respective sidebands. These lines come from a small amplitude modulation on the carrier that was deliberately sent through the entire measurement and data acquisition chain. This turned out to be very helpful, since it allows a kind of on-line monitoring of a large range of possible measurement errors. When this “artificial” modulation is small, that is, comparable to the beam modulation in the present case, it will have no detrimental effect on the measurement. However, these modulation lines should be spaced sufficiently wide from the beam-induced modulation, otherwise the two may overlap for small FFT time windows, when the frequency domain peaks get wide.

One point that needed to be checked thoroughly is the correlation between the beam spectrum and the observed modulation sidebands. There were also doubts about whether the beam can or cannot directly interact with the waveguide modes. The spectrum of the same stored beams as discussed before is shown in Fig. 7.16 [27]. The left plot shows a typical spectrum taken about 100 s after the first injection. A 40 MHz comb structure can be seen, which is due to the 25 ns bunch spacing in the LHC beam. The longitudinal bunch profile is usually approximated by cosine squared distributions with lengths of about 1 ns (3 dB width). This leads to the 40 MHz comb being multiplied

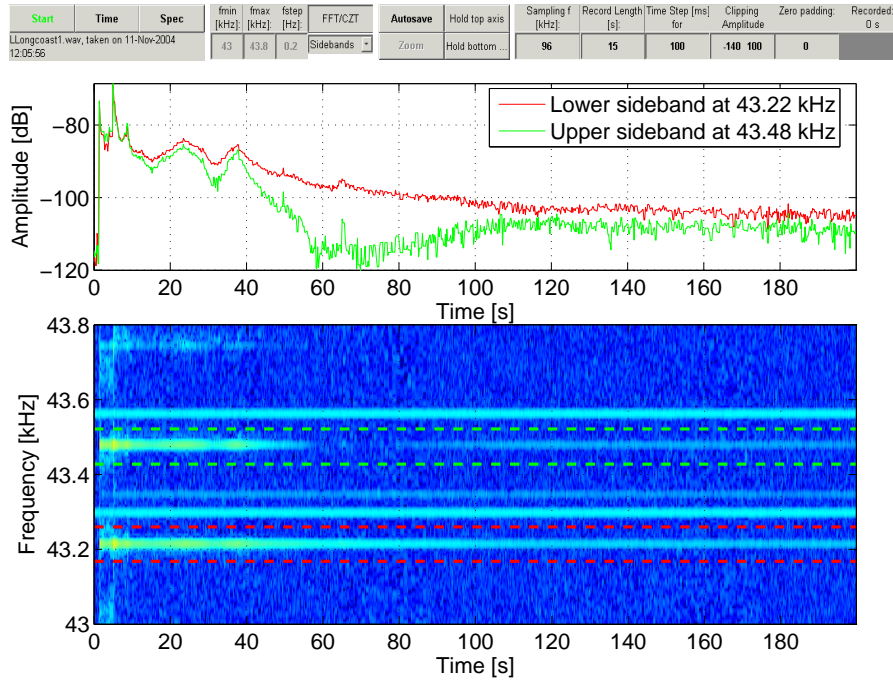


Figure 7.15: A screen-shot from the Matlab application for soundcard data acquisition and treatment. The modulation sidebands of a stationary LHC type beam on the short track were recorded over 200 s starting from injection. The beam energy was 26 GeV, the intensity at injection  $1800 \cdot 10^{10}$  protons. The bottom plot shows the spectrogram with the two sidebands at 43.22 and 43.48 kHz, respectively. In the upper plot, the sideband amplitude variation with time is depicted. The carrier has a relative level of  $-28.4$  dB.

by a  $\sin(f)/f$  distribution. The first zero of this distribution is at about 560 MHz. Calculating the height of the first sidelobe, a value of  $-32$  dB is found, which comes close to observed data. The second main lobe can then be expected at an amplitude of  $-41$  dB and at the working frequency of 2.84 GHz, the maximum side lobe amplitude is about  $-65$  dB.

In contrast to this approximation, the observed spectra may differ considerably at higher frequencies, for example due to microstructures in the bunch profile that correspond to high frequency components. At injection, in general the beam is excited and the spectrum is wide. When the beam is stored, the beam profile gradually converges towards a stable distribution. However, impedances in the machine may still excite instabilities, which translates to high frequency spectral components.

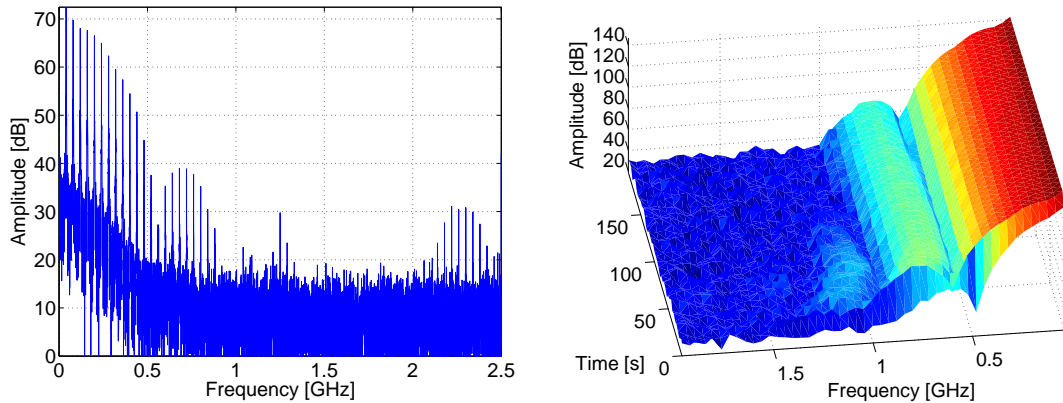
In the available data, due to the 5 GHz sampling rate the spectrum is limited to 2.5 GHz, and the peaks between 2 and 2.5 GHz appear to be due to intermodulation in the scope between the beam spectrum and half the sampling frequency. A smaller spurious line can be seen at 1.25 GHz, corresponding to a quarter of the sampling frequency.

For the first 200 s after injection, the power of the 40 MHz harmonics is plotted in Fig. 7.16(b). It is most interesting to note the general evolution of the spectrum. Shortly after injection the spectral power density is high, going well above 1 GHz. Towards the end of the trace, the lower components ( $f < 500$  MHz) stay almost constant, while the higher harmonics (above 1 GHz) fade out within about 100 s. It is not easily possible to extrapolate from the spectrum below 1.5 GHz the components at above 2 GHz, since the machine impedance which may excite resonances is frequency-dependant. Measurements carried out in 2001 and 2002 showed that the machine impedance decreases significantly in the range between 1.2 and 3 GHz, even though there seem to be some peaks around 3 GHz which could be attributed to pick-up resonances [3]. Therefore, it appears very likely that the harmonics up to 3 GHz will decrease in the same way after injection as those at around 1.25 GHz, or still faster. Physically, this corresponds to a “calming-down” of beam excitations after injection. The decrease of the beam spectrum due to beam losses is small on this time scale.

Comparing the modulation sidebands in Fig. 7.15 and the beam spectrum in Fig. 7.16, the following points can be retained:

- The modulation sidebands level off on the same time scale (100 s) as the high frequency beam harmonics ( $> 1$  GHz). This points to some link between the two effects. Amplifier saturation by beam-induced signals could play a major role here.
- After these first 100 s, the modulation gets very small, with sidebands about 80 dB below the carrier. However, compared to injection, the beam intensity did not change much, with a decrease of roughly 30 %. This means that a direct interaction between the beam and the microwaves can be ruled out.
- Already shortly after injection, the modulation sidebands have slightly different levels, in particular at the end of the trace. This implies a superposition of AM and PM even when beam-induced signals leading to possible saturation effects have decayed.

Another set of data from a stored beam with one to four single bunches is shown in Fig. 7.17. The modulation sidebands were very faint being  $-85$  dB below the carrier,



(a) The beam spectrum taken at about 100 s after injection.

(b) Evolution of the 40 MHz harmonics with time.

Figure 7.16: The beam spectrum of the stored LHC beam from Fig. 7.15.

but still about 10 dB above the noise level. About 20 minutes after injection of the beam, the carrier power was varied. If the observed modulation was due to saturation effects, than it should depend on the power of the carrier. This is because the gain compression curve of the amplifiers is very nonlinear, see Fig. 7.4. When the working point of an amplifier is shifted, the differential gain compression will change as well. In our case, since the carrier power was decreased, it can be expected that if the observed modulation is due to saturation, the modulation sidebands should decrease. There is only two cases when a variation of the carrier does not entail a change in the modulation amplitude.

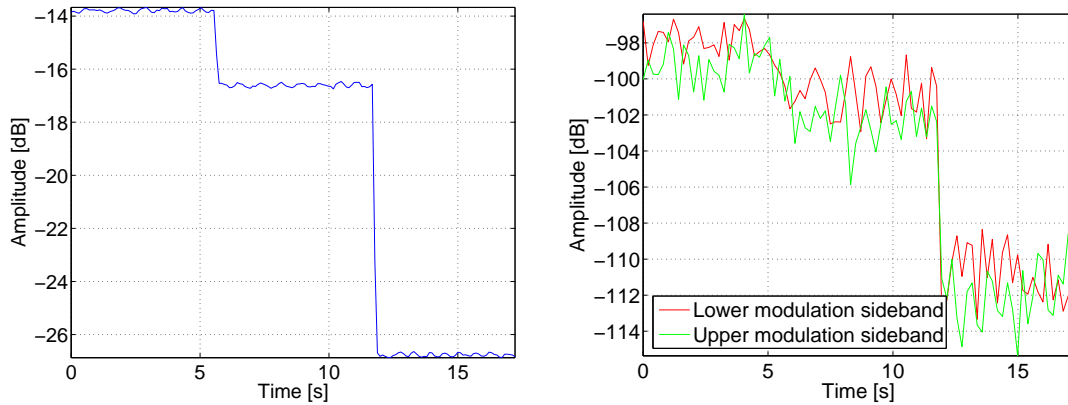
1. The carrier power is negligible compared to the signal that is saturating the amplifier. This would require unreasonable high beam-induced signals.
2. The beam-induced signals are very small compared to the carrier and the modulation is due to other factors.

The latter appears to be the case, which is a strong indication of some electron plasma-microwave interaction. Of course no significant electron cloud is expected for single bunch beams, however, the observed modulation is also *very* small, corresponding to a relative drop in the average carrier power by roughly  $10^{-8}$ .

## 7.5 Bench cross-check

In order to demonstrate the fact that there is a significant interaction between a magnetized electron cloud and waveguide modes, bench measurements were carried out. The goal was not so much to get quantitative results but rather to show that an electron cloud may have some effects on the transmitted microwave and that it is possible to measure it. Another reason for the experiment was to help us to get a feeling for this kind of phenomena.

It has to be added that there is a fundamental difference between the electron cloud in an accelerator and simple bench measurements. In an accelerator, the electrons are



(a) The carrier was decreased by first from 0 to  $-2.8$  dB at  $t \approx 6$  s, then to  $-10$  dB at  $t \approx 12$  s. (b) The two modulation sidebands follow the carrier within measurement uncertainty.

Figure 7.17: Variation of the relative carrier power in a single bunch stored beam several minutes after injection. The reference level was chosen arbitrarily.

created with a certain kinetic energy in the beam pipe itself in an extended region of high magnetic field. Ionization of residual gas, secondary emission or some other effect may be responsible for that. Then the electrons move under the influence of the external electric and magnetic forces. The result is a rather thin (about  $10^{12}$  per  $\text{m}^3$ ) electron plasma in a strong magnetic field.

In the proposed bench experiment, the electrons are created by emission of a heated filament. Leaving the filament at low energy, they can be accelerated to a given energy by a voltage between the filament and a close-by anode. This mechanism is implemented in the available electron gun, and the electrons can then be directed to some region of interest. When there is an external magnetic field present in this region, however, things get complicated. The electrons will be deflected by the inevitable fringe fields and not enter the region of interest. Creating electrons in an external magnetic field is not easy, either, since the electrons emitted by the filament have very low energies. Under the influence of a magnetic field, they will just spiral around with very small Larmor radii without gaining much energy from the acceleration voltage. With or without magnetic field, there will always be a very high electron density close to the cathode, which may even come into the range of the plasma frequency of the microwaves. For this state, the electron cloud-microwave interaction may be significantly different from what is expected in an accelerator beam pipe. In the experiment described below, it was tried to adjust the parameters such that a comparison with the beam pipe makes sense.

### 7.5.1 Electrons injected into a pipe carrying waveguide modes

The first object studied was an about 63 mm diameter 60 cm long stainless steel tube. In this circular cross-section waveguide, the fundamental  $\text{TE}_{11}$  cut-off is at 2.789 GHz and the  $\text{TM}_{01}$  cut-off at 3.643 GHz. On both ends, improvised hook antennas were mounted for the excitation of the vertically polarized  $\text{TE}_{11}$  and the  $\text{TM}_{01}$  mode. In the middle of the pipe, electrons of variable intensity and energy were injected by an electron gun as illustrated in Fig. 7.18(a). At a distance of 15 cm to one side, the vacuum pump was connected via a flexible hose, 15 cm to the other side the vacuum pressure meter

was installed. In the first run, these two ports were not shielded RF-wise. Electron gun, pressure meter and pumping hose were connected on 34 mm diameter flanges with a  $TE_{11}$  cut-off at 5.167 GHz. The electron gun coil current could be varied in the range between 0 to 3 mA, however the emitted electron current is lower by roughly a factor 3 to 10 [39]. Exact or interpolated values from the electron gun's specifications were used in all quantitative evaluations. The maximum electron energy was 500 eV. When electrons leave the gun, they have to pass through an about 1 mm wide diaphragm in the anode, situated about 2 mm outside the waveguide.

While getting acquainted with the set-up, a few interesting points were noticed.

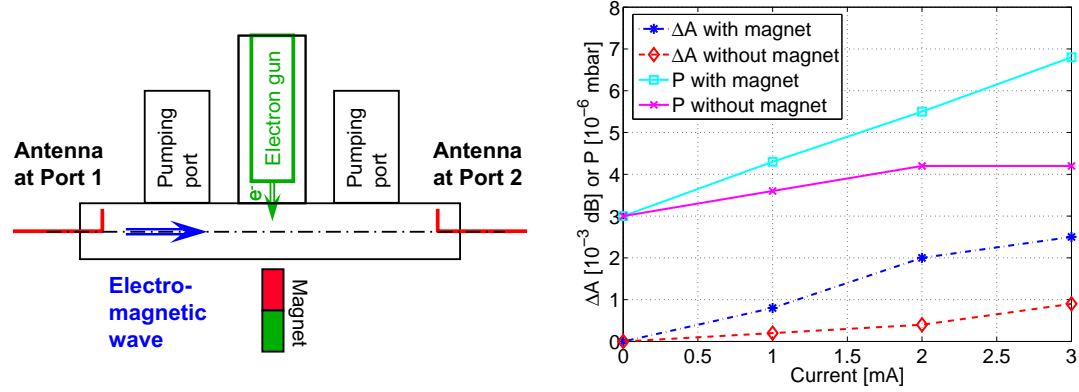
- When the electron gun is switched on and the electron beam goes to the waveguide, there is a vacuum pressure rise by up to a factor 2.
- This pressure rise is higher for higher electron currents and higher electron energies.
- When the electron acceleration voltage is switched off, very few electrons are emitted and no noticeable pressure rise is found.
- For low electron energies, between thermic energies (0.025 eV at 300 K) and 10 eV, the vacuum pressure increase is low.
- When a “strong” horseshoe permanent magnet is approached to the pipe or the operating electron gun, the vacuum pressure readings plummet to levels found when the electron gun or the electron acceleration voltage is switched off.

These first observations show that the vacuum pressure is a valuable indicator of electrons leaving the electron gun. After flying across the waveguide, they impinge on the opposite wall, liberating secondary electrons and ions, which leads to an increase in vacuum pressure. Approaching the horseshoe magnet actually puts the electron gun out of service, because the strong magnetic field prevents the electrons from leaving the electron gun. For this reason, a small permanent magnet was used later on. It was placed close to the location where the electrons should hit the pipe wall, on the side opposite of the electron gun.

A series of data was taken with and without magnet. It was found that the transmission through the waveguide changes slightly when the magnet is placed next it. This parasitic effect was overcome by switching the electron beam on and off with the magnet staying in place and comparing the measured  $S_{21}$ . For practical reasons, in particular the lifetime of the filament, the filament current was kept constant and only the acceleration voltage was turned on and off.

Fig. 7.18(b) shows the results obtained at one specific frequency for different filament currents. The amplitude differences plotted correspond to the drop in  $S_{21}$  when electrons are injected into the waveguide. It has to be noted that the changes in transmission are very small but repeatable. The instrument drift over the measurement time scale (a few seconds) is below  $10^{-4}$  dB, which makes such a sensitive measurement possible. For higher electron currents, the difference in attenuation increases. This effect is much more pronounced when a small magnetic field is applied. In addition to that, the vacuum pressure rises considerably more than without magnetic field.

Using the characteristic dimensions of the electron gun, the density of the electron



(a) Bench measurement set-up. Electrons are injected into a waveguide along which microwaves are propagated.

(b) Results at 4.0363 GHz for the electron gun current varied.  $\Delta A$  is the change in attenuation when the electron acceleration voltage was increase from 0 to 500 V, P is the vacuum pressure. The pumping ports were not shielded.

Figure 7.18: The bench measurement on waveguide mode transmission through an electron plasma.

E [eV]	I [mA]	$\rho_{max}$	$f_{p,max}$ [MHz]
10	0.34	$8.7 \cdot 10^{13}$	84
100	0.64	$5.2 \cdot 10^{13}$	65
500	1.2	$4.2 \cdot 10^{13}$	58

Table 7.3: Calculated electron densities at the iris of the electron gun, as well as the corresponding plasma frequency.

beam could be estimated. The electrons left the gun through a flat elliptic iris 9 mm times 1.8 mm wide. The 50 % opening angles of the electron beam are  $30^\circ$  and  $5^\circ$ , respectively. The longer side and thus the wider opening angle was oriented horizontally. With the electron energy and the pipe dimensions given, the electron density can be easily calculated. The maximum electron density  $\rho_{max}$  close to the iris is given by

$$\rho_{max} = \frac{I/e}{A\sqrt{2E[eV]}e/m} \quad (7.4)$$

for electrons with charge  $e$ , mass  $m$  and energy  $E$  emitted at a current  $I$  through the iris surface  $A = 13 \text{ mm}^2$ . Table 7.3 lists the calculated electron densities. The emitted electron current  $I$  as a function of the filament current was obtained from the data sheet. Since the electrons impact on an untreated stainless steel surface, secondary emission will occur. Depending on the electron energy, the secondary emission yield can be expected to be above 1. The angular distribution of these electrons is often approximated by a  $\cos \Theta$  dependence, with  $\Theta$  being the angle from the surface normal. As the opening cone of the electron gun spans only about 1 % of the  $2\pi$  solid angle, only a very small fraction of the secondaries will be re-emitted in the region of the primary electrons. The increase in maximum electron density will thus be very minor. Instead, a cloud of low energy electrons may form. The SEY at low energies is very small, but the electron reflectivity may be close to unity, entailing a considerable electron build-up.

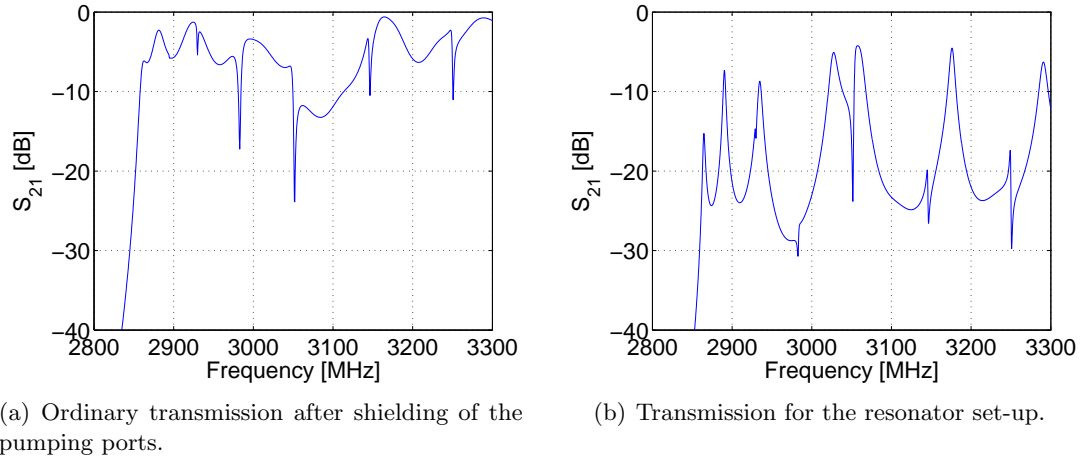


Figure 7.19: Transmission through the waveguide for the bench measurement without electrons and no external magnetic field applied.

Under similar conditions in the SPS a reflectivity of about 0.5 was found [40]. Assuming a value in this range, the electron cloud density will not increase significantly due to low energy electrons.

For a second experimental run using a refined set-up, the electron gun's iris was oriented vertically. The pumping ports on either side of the electron gun were shielded with a metallic grating. The electron cloud-related changes in transmission at 4.0363 GHz could not be repeated. Only a very small electron cloud dependent variation was found at 3.15 GHz. As can be seen in the Fig. 7.19(a), there is a notch in the transmission at this frequency, pointing to a destructive interference between two or more waves. In the following it was discovered that electron cloud-related amplitude changes can be observed only in the vicinity of such notches.

### 7.5.2 Resonator measurements

In order to verify the results described above, another measurement technique was used: the resonator. In general, resonator measurements allow to quantify attenuation to a very high precision by determining the quality factor at the location of the resonance peaks. Reactive impedances show up as shifts in the resonance frequencies, but they do not impact the Q factor. The set-up was transformed into a waveguide resonator by the use of capacitive coupling at both Port 1 and Port 2. Fig. 7.19(b) shows the transmission through the entire set-up. No external magnetic field was applied.

Here the results for the resonance peak at 2935 MHz are presented; the other peaks showed similar behaviour. This peak had a loaded quality factor  $Q_L = 510$ . Interestingly enough, with or without electrons and with or without a small magnetic field no change in the attenuation could be observed. With a calculated waveguide attenuation of 0.1 dB and the precision of the Q measurement of the order of  $10^{-3}$ , the additional attenuation should thus be below  $10^{-4}$  dB. However, the phase of the transmitted wave was found to vary in dependence of the electron cloud. Fig. 7.20 shows the transmission through the waveguide when the electron energy was varied. Over the first 5 s the electron gun's acceleration voltage was increased from 0 eV (no electrons) to 200 V. After another 5

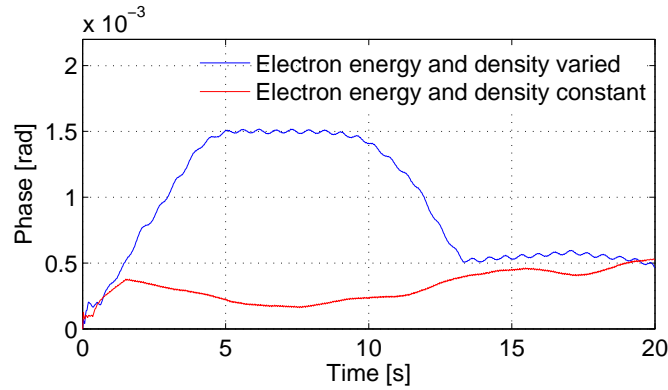


Figure 7.20: Change in the phase of  $S_{21}$  at the resonator peak at 2.935 GHz when the electron energy is varied. Due to the characteristics of the electron gun, this also causes a change in the density. For the blue trace, between  $t = 1$  and  $t = 5$  s the electron energy was increased from 0 eV (no electrons reaching the waveguide) to 200 eV, between  $t = 9.5$  and  $t = 13$  s the electron energy was reduced back to 0 eV. The electron current at 200 eV was about 0.6 mA.

s the acceleration voltage was ramped back down to 0 V (blue trace). For evaluation of the trace stability data was taken with the acceleration voltage constant at 0 V (red trace). A phase shift of about 1 mrad could be observed, while no significant amplitude change was found.

### 7.5.3 Discussion

First we will concentrate on the phase shift observed in the resonator measurement. As the resonator enhances the phase shift by its loaded Q factor, the measured phase shift must be divided by  $Q_L = 510$  to find the one-way phase shift  $\Delta\phi' = 2 \cdot 10^{-6}$  rad. Equations 7.1 and 7.2 were evaluated to compare this value with the expected phase shift  $\Delta\phi$ . Since at 2.935 GHz only the  $TE_{11}$  mode can propagate and only the vertical polarization of this mode is excited by the antennas, the maximum of the mode's electric field is the vertical center plane of the pipe. Therefore it can be expected that the major part of the electron cloud-microwave interaction will occur in the center of the pipe. For this reason the electron density in the center of the pipe was used for the calculation of the phase shift. In this region  $\rho_e = 2.6 \cdot 10^{12} \text{ m}^{-3}$  was found at an energy of 200 eV. Using the 50 % width of the electron beam for the interaction length  $L$  and dividing by 3, since the electron beam covers only about one third of the central part of the pipe,  $\Delta\phi = 1.4 \cdot 10^{-6}$  rad is found. This compares well with the value obtained in the resonator measurement  $\Delta\phi' = 2 \cdot 10^{-6}$  rad. The discrepancy is probably due to a number of estimations involved in the calculation of  $\Delta\phi$ , in particular the interpolation of the electron current from the data sheet, the shape of the electron beam, the simplified electron cloud-microwave interaction region and secondary emission. The results of the resonator measurements can thus be explained by the ordinary phase shift of an unmagnetized plasma. This phase shift occurs at all frequencies above the plasma frequency, but only at resonance peaks it is sufficiently enhanced so that it can be

detected.

No electron cloud-related amplitude change was observed in the resonator experiment at the resonance peaks, contrary to previous transmission measurements where this effect was found. It was noticed that these amplitude changes appear only close to notches in the pipe's transmission response. This gives a hint to the origin of these amplitude variations. Even after shielding the pumping ports the pipe used is not a perfectly smooth waveguide. In addition to that the improvised antennas have an  $S_{11}$  of  $-10$  dB or higher. For these reasons the transmitted wave is scattered, and for certain frequencies the resulting waves interfere destructively, in some cases almost cancelling each other. For such frequencies we see the sharp drops in  $S_{21}$ . Now if the electron cloud induces a small phase shift in one of the waves, the notch will move in frequency and for one fixed frequency a small change in amplitude can be observed. On one side of the notch the change will be positive, on the other side negative. This effect was observed. In the following we estimate the amplitude change in dependence of the phase shift.

Let's assume a "typical" notch with a drop of 30 dB. This amplitude difference corresponds to the second wave having an amplitude  $A_2 = A_1(1 - 10^{-30/20}) = 0.968A_1$ . Let's further assume that the electron cloud causes a small phase shift  $\Delta\phi$  on the first wave. The amplitude change will be maximum when the first wave has maximum slope, that is, when it is close to its zero crossing. The change in amplitude is then  $\Delta\phi A_1$  or lower. Using the measured value  $\Delta\phi = 2 \cdot 10^{-6}$  rad one gets as a pessimistic estimation for the new total amplitude  $A_1(1 - p) - A_2$ , about  $5.5 \cdot 10^{-4}$  dB lower than before. This value is of the order of magnitude of the data displayed in Fig. 7.18(b). It is a strong indication that the observed amplitude changes originate from phase shifts in regions of drops due to interference. The fact that such amplitude changes were much smaller after the shielding of the pumping ports also points in this direction.

When a small magnetic field is applied in the interaction region, the amplitude change is strongly enhanced. There is no quantitative explanation yet for this fact.

Concluding, the bench experiment has shown that

- We can measure the electron cloud-induced phase shift in a short waveguide
- In regions where the transmission response has sharp drops due to interference of scattered waves in the pipe, this phase shift can convert into an amplitude change
- This effect is enhanced in the presence of a magnetic field
- A similar mechanism should be at work in the SPS, where the beam pipe is very inhomogeneous.

## 7.6 Possible explanations

Among the effects observed in the SPS, amplifier saturation in the up-going signal path most probably plays a role in the attenuation peaks at each injection. The strong correlation between the beam spectrum and the modulation sidebands is a clear indication for this. However, there may still be some electron cloud-microwave interaction superimposed, but the signals are hard to disentangle. We will therefore concentrate on the two cases, where evidence of an electron cloud-microwave interaction has been found.

- The asymmetric spectrum at cyclotron resonance (Fig. 7.12(a)) and

- the small modulation in stored beams that remains after several minutes (Figs. 7.16 and 7.17).

### 7.6.1 Electron cyclotron absorption

The asymmetric modulation spectrum found close to cyclotron resonance in the main bending magnets points to an effect linked to the electron cyclotron resonance. In plasma physics, electron cyclotron absorption is widely used for heating and probing of plasmas. In fusion plasmas, in general the wavelength is much smaller than the typical length of the interaction region, which means that guided-wave effects are less important. The results for this case can be summarized as follows [28].

- Only the fundamental of the cyclotron resonance frequency  $f_c$  has absorption. Since  $f_c$  is proportional to the magnetic field and most of the measurements were performed *below* cyclotron resonance in the dipoles at injection, there exist always locations in the dipole fringe fields and in the quadrupoles where the cyclotron resonance condition is fulfilled. Thus we can expect that cyclotron resonance will always happen, and in the special case of cyclotron resonance in the homogeneous dipole field, the effect will be particularly strong.
- The interaction at succeeding harmonics of  $f_c$  decreases roughly by the small factor  $T_e/mc^2$  with the electron temperature  $T_e$  and the electron energy at rest  $mc^2$ . For typical electron cloud energies in the range of 100 eV, the interaction at harmonics of the plasma frequency should be very low.

Magnetized plasmas can interact in yet another way with microwaves. Electromagnetic waves in magnetized plasmas can propagate as various different modes. In general, mode conversion will occur in a waveguide, leading to power loss via reflection and absorption by coupling to lossy evanescent modes.

Two interesting cases are (1) a strong static B field normal to the E field of wave and (2) a static B field parallel to the E field of the wave. In the first case, the electrons are locked by the magnetic field to a plane normal to the wave's E field, so they cannot follow the excitation of the wave. Such waves propagate like if there was no electron plasma. This case corresponds to a mode with vertically polarized E field in an orbit correction dipole with a horizontal B field. In case (2) the electrons are free to move with the electric field of the wave. They feel the same interaction as in an unmagnetized plasma. This is the case of the fundamental TE mode in the main bending magnets. However, since the dipole vacuum chambers are not rectangular, there is a small transverse component in the wave's E field that may interact with the electrons.

If the static magnetic field is neither parallel nor normal to the wave's electric field, mode conversion can be expected. This case is found in the quadrupoles. The same effect could be also responsible for the enhanced attenuation with magnetic field in the electron gun bench measurement. Cyclotron absorption is out of question in the bench measurement due to the small magnetic field. Another indication for this is that no attenuation due to dissipative losses was found in the resonator measurements.

### 7.6.2 Tails

Up to the present day, the tails have defied all attempts of finding an explanation.

## 7.7 Summary

Microwave transmission measurements were performed in the SPS beam pipe during the 2003 and 2004 runs. The idea was to determine the line-averaged density of the electron cloud by measuring its interaction with waveguide modes. For theoretical reasons the microwaves should not interact directly with the beam. A strong beam-induced attenuation has been observed for various machine, beam and RF parameters. These results might be affected to some degree by amplifier saturation. For this reason, a repetition of the principal measurements with special care taken to avoid this parasitic effect would be desirable. However, for measurements at the cyclotron resonance frequency in the main bending magnets, as well as for stored beams, strong indications for electron plasma-microwave interaction have been found. Bench measurements completed this image by showing small effects in agreement with basic theoretical predictions. For the SPS beam pipe a quantitative evaluation remains very difficult due to the complexity of the situation.

### Lessons learned

During the 2003 and 2004 run, lots of experience was gained with respect to instrumentation and data acquisition. The following points have to be retained for future experiments.

- Suppress the beam-induced signals as much as possible in both the down- and the up-going signal path, e.g. using a waveguide cavity filter with a few MHz bandwidth.
- Choose straight sections of beam pipe without magnets or an arc section with dipoles only. Except for fringe fields the wave E field is then parallel to the static B field, making an interpretation of the results easier.
- Work with a carrier frequency a factor three or so above the highest electron cyclotron frequency. This should considerably reduce cyclotron absorption [28], making it easier to measure the expected phase shifts. In the LHC at injection energy, the cyclotron resonance is below 1 GHz, so this condition can be met using the fundamental TE or TM waveguide mode.
- As was seen in the bench experiment, in a frequency range with strong destructive interference between different waves, phase shifts can translate to changes in amplitude and vice versa. A frequency range where the transmission response is sufficiently flat over at least a few MHz should be chosen.

# Conclusion

In this thesis two remote sensing applications using waveguide modes in accelerator beam pipes are presented. A major part of the work is dedicated to the LHC reflectometer, which is an implementation of time domain reflectometry for obstacle detection on the LHC beam screen. The first TE and TM modes in the beam screen were used. The actual measurements were performed using a modern vector network analyser. Signal processing as well as data display and archiving were implemented in an application with an easy to use graphic interface. Two scenarios for deployment of the LHC reflectometer were proposed, namely the Assembly Version for inspections during the construction of the LHC and the In Situ Version for measurements with the machine under vacuum. For the Assembly Version, couplers for the excitation of the first TE and TM mode were successfully designed, manufactured and tested. On a 50 m long run of beam screen, obstacles as small as M4 nuts could be detected. In another experiment, on the cryogenic ring lines, recent trials of the complete system on up to 400 m long sections showed very promising results.

For the In Situ Version, couplers for permanent installation in LHC were designed. It is expected that after cool-down, entire LHC arcs with 2.8 km length can be covered by reflectometry measurements. However, due to the excessive distance and the difficult coupler design, reference measurements after completion of each arc will be needed to maximize the system's performance.

The second part of this work reports on the microwave transmission experiments that were carried out in the SPS beam pipe. An electron cloud present in the beam pipe should interact with the waveguide modes, thereby revealing some of its characteristics. A complex measurement and data acquisition system was set up, tested and optimized during the 2003 and 2004 machine runs. However, due to the high beam-induced signals and the generally very complicated problem the results are difficult to interpret. A small bench measurement was set up in order to gain additional insight in the electron cloud-microwave interaction. The tiny electron cloud-induced phase shift predicted by theory for a thin unmagnetized plasma could be measured. Further practical and theoretical work is needed for a reliable measurement and interpretation of this kind of transmission experiment. This work closes with a number of do's and don'ts that were found for the practical part.

# Bibliography

- [1] *Basic Course on General Accelerator Physics*,  
CERN Accelerator School 2000, CERN-2005-004, Geneva (2005)
- [2] *The LHC Main Ring*,  
LHC Design Report, Vol. 1, CERN-2004-003, Geneva (2004)
- [3] *The LHC Injector Chain*,  
LHC Design Report, Vol. 3, CERN-2004-003 (2004)
- [4] Lapostolle, P. M., *Introduction to RF linear accelerators*,  
CERN Accelerator School, CERN-96-02 (1996)
- [5] Stambach, T., *Introduction to Cyclotrons*,  
CERN Accelerator School, CERN-96-02 (1996)
- [6] Steerenberg, R., *Introduction to Particle Accelerators*,  
<http://humanresources.web.cern.ch/humanresources/external/training/tech/special/AXEL2003.asp> (2003)
- [7] Kroyer, T., *A Waveguide High Order Mode Reflectometer for the Large Hadron Collider Beam-pipe*, Diplomarbeit, Wien (2003)
- [8] Caspers, F. et al., *Wireless impedance measurements and fault location on ESRF vacuum chamber assemblies*, CERN-PS-92-30-AR, Geneva (1992)
- [9] Meinke, H. and Gundlach, F. W., *Taschenbuch der Hochfrequenztechnik*, Dritte Auflage, Springer-Verlag, Berlin (1968)
- [10] Zinke, H. and Brunswig, H., *Lehrbuch der Hochfrequenztechnik*, Springer-Verlag, Berlin (1973)
- [11] *Mechanical Design Aspects of the LHC Beam Screen*, IEEE (1998)
- [12] *Beam Screens for the LHC Cold Arcs*, LHC-VSS-ES-0001, CERN, Geneva (2002)
- [13] Veness, R. et al., *Design Aspects of the RF Contacts for the LHC Beam Vacuum Interconnects*, Proceedings of the 2001 PAC, Chicago (2001)
- [14] Veness, R. et al., *Beam Vacuum Interconnects for the LHC Cold Arcs*, Proceedings of the 1999 PAC, New York (1999)

- [15] Tan, J. et al., *Surface Resistance Measurements and Estimate of the Beam-Induced Resistive Wall Heating of the LHC Dipole Beam (Screen,)* LHC Project Report 307, CERN, Geneva (1999)
- [16] Kohler, M., *Annalen der Physik* 32, 211 (1938)
- [17] Kroyer, T., Caspers, F., *Coupler Structures for the LHC Beam Pipe Waveguide Mode Reflectometer*, Proceedings of the 9th European Particle Accelerator Conference (EPAC), Lucerne, Switzerland, CERN-LHC-Project-Report-764 (2004)
- [18] <http://hyperphysics.phy-astr.gsu.edu/hbase/electric/ohmmic.html>
- [19] [http://www.alloywire.com/german/alloy\\_stainless\\_steel\\_302.html](http://www.alloywire.com/german/alloy_stainless_steel_302.html)
- [20] *VAT Katalog 2004*, [http://www.vatvalve.com/cps/rde/xbcr/SID-3D19B28C-1D566DE2/public\\_eng/Katalog2004\\_E.pdf](http://www.vatvalve.com/cps/rde/xbcr/SID-3D19B28C-1D566DE2/public_eng/Katalog2004_E.pdf)
- [21] Syratcev, I., *Mode Launcher as an Alternative Approach to the Cavity-Based RF Coupler of Periodic Structures*, CERN-PS-RF-NOTE-2002-013, Geneva (2002)
- [22] Rathjen, C., *Mechanical behaviour of vacuum chambers and beam screens under quench conditions in dipole and quadrupole fields*, CERN-LHC-Project-Report-582, Geneva (2002)
- [23] Magistris, M. et al., *Study for Magnets and Electronics Protection in the LHC Betatron-Cleaning Insertion*, to be published in Nuclear Instruments and Methods in Physics Research (2005)
- [24] Zimmermann, F., *Electron-cloud Simulations: An Update*, Chamonix (2001)
- [25] Herring, T., *Modern Navigation*, <http://bowie.mit.edu/~tah/12.215>
- [26] Fontolliet, P.-G., *Systèmes de Télécommunications*, Traité d'Electricité, Vol. 17, Lausanne (1999)
- [27] Private Communication with T. Bohl (2005)
- [28] Prater, R., *Heating and current drive by electron cyclotron wave*, Physics of Plasmas, Volume 11, Number 5, San Diego (2004)
- [29] Harkay, K., *Electron Cloud Observations: A Retrospective*, Proceedings of the 31st ICFA Advanced Beam Dynamics Workshop (E-CLOUD '04), CERN-2005-001 (2005)
- [30] Rossi, A., *SEY and electron cloud build-up with NEG materials*, Proceedings of the 31st ICFA Advanced Beam Dynamics Workshop (E-CLOUD '04), CERN-2005-001 (2005)
- [31] Stupakov, G. and Pivi, M., *Suppression of the effective SEY for a grooved metal surface*, Proceedings of the 31st ICFA Advanced Beam Dynamics Workshop (E-CLOUD '04), CERN-2005-001 (2005)

- [32] Arduini, G. et al., *Electron-Cloud Build-Up Simulations and Experiments at Cern*, CERN-AB-2004-082, Geneva (2004)
- [33] Kroyer, T. et al., *Unexpected Results On Microwave Waveguide Mode Transmission Measurements in the SPS Beam Pipe*, Proceedings of the 31st ICFA Advanced Beam Dynamics Workshop (ELOUD '04), CERN-2005-001, 2005
- [34] Jimenez, M., *Electron Clouds and Vacuum Effects in The Sps*, Proceedings of the 31st ICFA Advanced Beam Dynamics Workshop (ELOUD '04), CERN-2005-001, 2005
- [35] Zimmermann, F., *Electron Cloud Effects in the LHC*, Proceedings of the Mini-Workshop on Electron-Cloud Simulations for Proton and Positron Beams, (ELOUD '02), CERN-2002-001 (2002)
- [36] Benedetto, E. et al., *Simulation of Transverse Single Bunch Instabilities and Emittance Growth Caused by Electron Cloud in LHC and SPS*, Proceedings of the 31st ICFA Advanced Beam Dynamics Workshop (ELOUD '04), CERN-2005-001, 2005
- [37] Riddone, G., *Dimensions, Pressures, Temperatures and Sizing of Valves and Piping in the LHC Machine Cryostat and Cryogenic Distribution Line*, LHC-Q-ES-0001 rev. 1.1, EDMS 90032, CERN (2000)
- [38] Heald, M. A. and Wharton, C. B., *Plasma Diagnostics with Microwaves*, Wiley, New York, 1965
- [39] Specs GmbH, *Specifications of the Flood Gun FG15/40S*, Berlin, 1999
- [40] Private Communication with D. Schulte (2005)
- [41] Mostacci, A., *Beam-Wall Interaction in the LHC liner*, CERN thesis-2001-014 (2001)
- [42] Kos, N., *Pumping Slot Shields for LHC Beam Screens*, AT-VAC-EN2/NK, CERN (2003)
- [43] Kroyer, T., Caspers, C., Mahner, E., *The CERN-SPS Experiment on Microwave Transmission through the Beam Pipe*, Particle Accelerator Conference PAC 2005, CERN-AB-2005-027 (2005)
- [44] Caspers, F., Morvillo, M., Ruggiero, F., *Surface Resistance Measurements of LHC Beam Screen Samples*, Proceedings of EPAC 2000, Vienna (2000)
- [45] *Technical Specification for the Manufacture of the Beam Screen Tubes for LHC Cold Arc Magnets*, LHC-VSS-CI-0001 (2000)
- [46] Ronde, F. C. *Ideal W.G. to Coax Transitions using a F.B.M. Monopole*, IEEE MTT-S International, p. 591-594 vol.2 (1988)
- [47] Private Communication with Ch. Rathjen (2003)

# List of Abbreviations

ADC: Analog to digital converter  
ALICE: A Large Ion Collider Experiment at CERN LHC  
ATLAS: A Toroidal LHC ApparatuS, an LHC experiment  
BNL: Brookhaven National Laboratory, a particle physics lab in the U.S.  
CERN: Conseil Européen pour la Recherche Nucléaire, the European Organization for Nuclear Research  
CLIC: Compact Linear Collider, an accelerator under study at CERN  
CMS: Compact Muon Solenoid, an LHC experiment  
CST: Computer Simulation Technology, a company name  
CW: Continuous wave, a sine wave with constant frequency  
DFT: Discrete Fourier Transform  
DS: Dispersion suppressor, a part of the LHC machine  
DSL: Dispersion suppressor left, a part of the LHC machine  
DSR: Dispersion suppressor right, a part of the LHC machine  
EC: Electron cloud  
ESRF: European Synchrotron Radiation Facility, a synchrotron light source near Grenoble, France  
eV: electron-Volt, a unit for energy, especially for particles  
FFT: Fast Fourier Transform  
FMCW: Frequency Modulated Continuous Wave, a radar technique  
GeV: Gigaelectron-Volt, a unit for energy, especially for particles  
GPS: Global Positioning System  
HTF: Hardware transfer function, the radio frequency transmission through a system with the beam off  
IF: Intermediate frequency  
IR: Interaction region, center of an octant of the LHC machine  
ISOLDE: On-Line Isotope Mass Separator, an experimental area at CERN  
keV: kiloelectron-Volt, a unit for energy, especially for particles  
LAN: Local Area Network  
LEIR: Low Energy Ion Ring, an ion storage ring at CERN  
LEP: Large Electron Positron collider, an ancient accelerator at CERN  
LHC: Large Hadron Collider, the particle accelerator currently being built at CERN  
LHCb: An LHC experiment on the violation of the charge/parity symmetry  
Linac: Linear accelerator  
LO: Local Oscillator  
LSS: Long Straight Section, a part of the LHC machine, about 500 m long  
MBA: Main Bending magnet A, a dipole magnet

MBB: Main Bending magnet B, a dipole magnet  
MD: Machine Development, a dedicated period of accelerator operation  
MQ: Main Quadrupole, a quadrupole magnet  
N: A screw-lock radio frequency connector  
NEG: Non Evaporable Getter, coating used for pumping and reduction of the secondary emission yield  
PEP2: Positron Electron Project 2, an accelerator at Stanford, U.S.  
PNA: A family of network analysers  
PS: Proton Synchrotron, an accelerator at CERN  
PSB: Proton Synchrotron Booster, an accelerator at CERN  
QRL: Cryogenic Ring Line, a line that transports Helium in LHC  
RF: Radio Frequency  
RRR: Residual Resistivity Ratio, ratio of a sample's resistivity measured at room temperature to the resistivity measured at temperature of liquid helium  
SEY: Secondary Emission Yield, average value of secondary electrons emitted by a surface by one impinging electron  
SFT: SPS Fixed Target, a type of beam in the CERN SPS  
SMA: Surface-Mount A, a screw-lock RF connector  
SPA: SPectrum Analyser  
SPS: Super Proton Synchrotron, an accelerator at CERN  
SSS: Short Straight Section, a part of an LHC cell, about 7 m long  
TE: Transverse Electric, a waveguide mode with transverse electric field only  
TEM: Transverse Electromagnetic, a wave with only transverse electric and magnetic field components  
TeV: Teraelectron-Volt, a unit for energy, especially for particles  
TI2: Transfer line for particles between CERN's SPS and LHC  
TI8: Transfer line for particles between CERN's SPS and LHC  
TM: Transverse Magnetic, a waveguide mode with transverse magnetic field only  
VB: Visual Basic  
VM module: A part of LHC housing mainly vacuum installations and RF couplers  
VNA: Vector Network Analyser

# Acknowledgements

I would like to express my profound gratitude to my supervisor Fritz Caspers for his amiable supervision, many stimulating discussions and all the material he placed at my disposal.

During my work, I profited from the hospitality of CERN, in particular the Radio Frequency group of the AB department. My thanks go to all the people here at CERN who helped me in various ways, particularly Flemming Peterson and Trevor Linnecar who always supported my project.

I would also like to mention Noël Hilleret, Paul Cruikshank and Laurent Faisandel from the AT-VAC group, with whom we had many constructive discussions concerning the coupling structures for the In Situ Reflectometer. I am indebted to Jacques Genest and David Tristram for the mechanical design of the Assembly Version couplers. The mechanical parts fabricated by the RF workshop were also much appreciated.

I would like to thank Alain Poncet and Lloyd Williams from the AT-CRY group and Zenon Zulek and Leszek Hajduk from Krakow University for the fruitful cooperation implementing the Assembly Version Reflectometer and performing the QRL measurements.

Thanks as well to Thomas Bohl, Frank Zimmermann, Wolfgang Höfle, Stefano Alberti, Jean-Francois Malo, Joachim Tückmantel, Bernhard Dehning, Gianluigi Arduini and Miguel Jimenez for help and inspiring discussions about the SPS microwave transmission measurement.

My special thanks go to my Austrian supervisor Arpad L. Scholtz from the Institute of Communications and Radio-Frequency Engineering at the Vienna University of Technology.

I would like to express my deepest thanks to my family, who always supported me in all possible ways. I want to thank my friends with whom I passed such an interesting time and who helped me in many practical ways. Last but not least, I want to say thanks to the girl who followed my work with so much understanding and interest.

This thesis was done in the framework of the Austrian Doctoral Students Programme, supported by the Austrian Federal Ministry for Education, Science and Culture.